USGS
science for a changing world

Prepared in cooperation with the Lahontan Regional Water Quality Control Board

Sequestration and Reoxidation of Chromium in Experimental Microcosms

Chapter I of

Natural and Anthropogenic (Human-Made) Hexavalent Chromium, Cr(VI), in Groundwater near a Mapped Plume, Hinkley, California

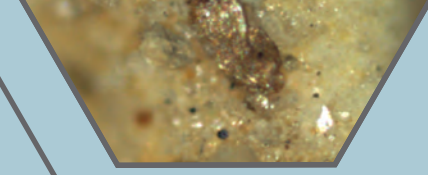

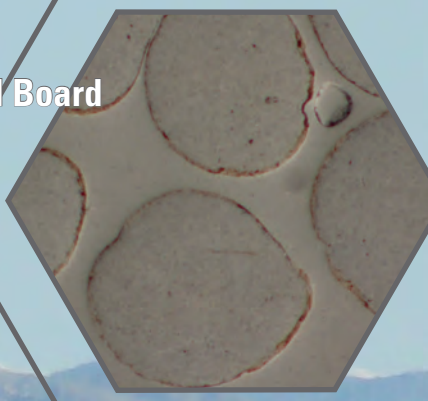

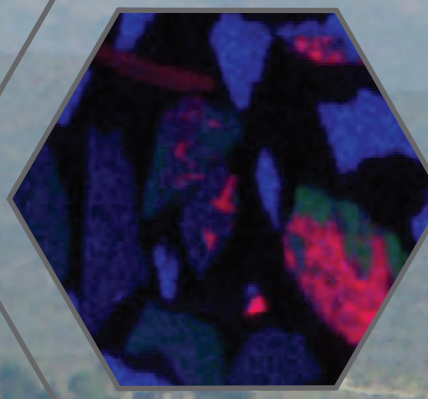

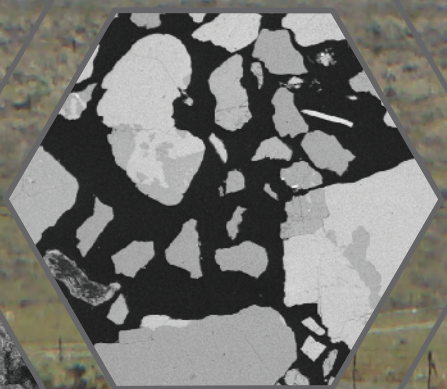

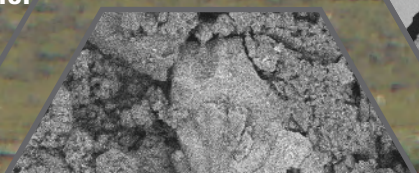

Professional Paper 1885-I

U.S. Department of the Interior
U.S. Geological Survey

Front cover

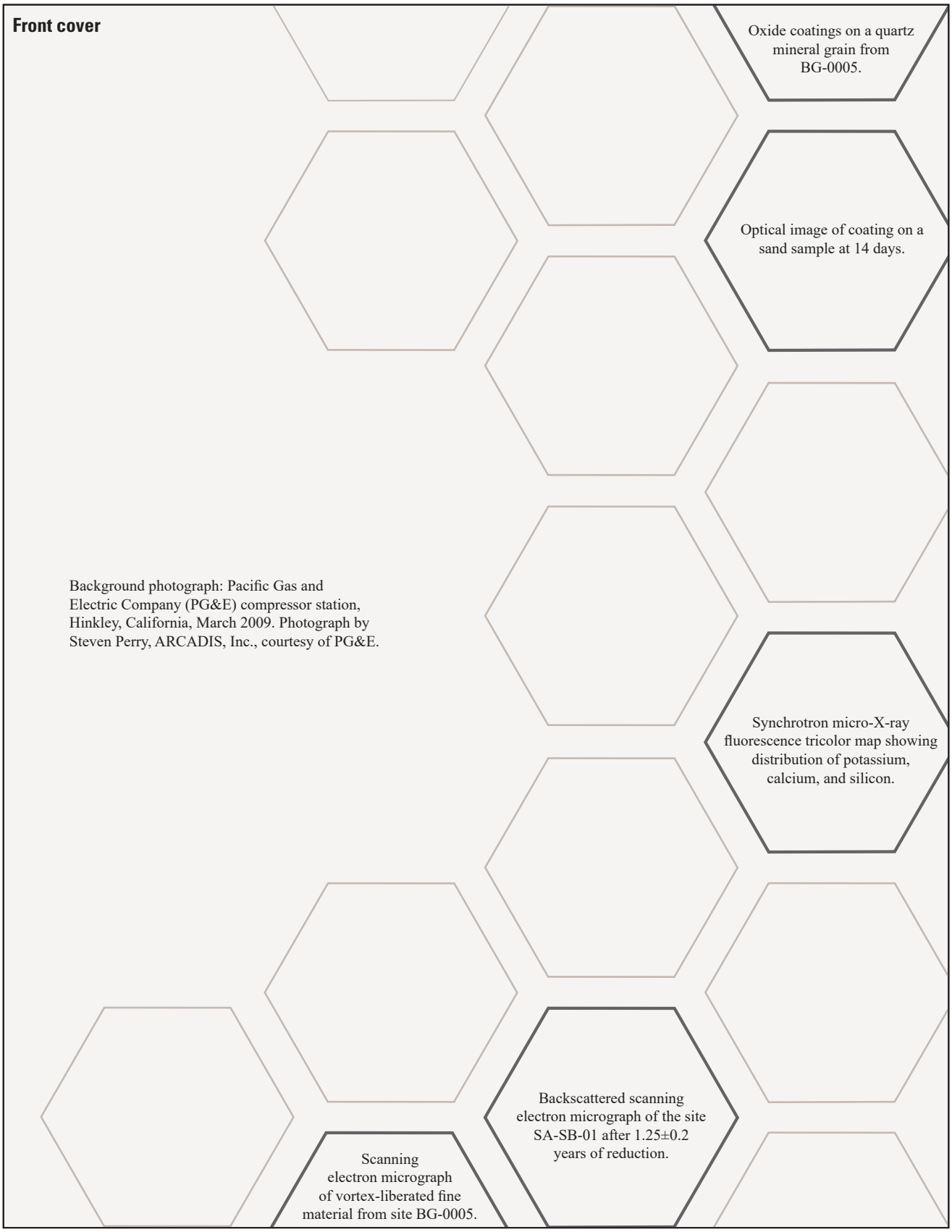

Oxide coatings on a quartz mineral grain from BG-0005.

Optical image of coating on a sand sample at 14 days.

Background photograph: Pacific Gas and Electric Company (PG&E) compressor station, Hinkley, California, March 2009. Photograph by Steven Perry, ARCADIS, Inc., courtesy of PG&E.

Synchrotron micro-X-ray fluorescence tricolor map showing distribution of potassium, calcium, and silicon.

Backscattered scanning electron micrograph of the site SA-SB-01 after 1.25±0.2 years of reduction.

Scanning electron micrograph of vortex-liberated fine material from site BG-0005.

Sequestration and Reoxidation of Chromium in Experimental Microcosms

Chapter I of

Natural and Anthropogenic (Human-Made) Hexavalent Chromium, Cr(VI), in Groundwater near a Mapped Plume, Hinkley, California

By Laurence G. Miller, Callum E. Bobb, Andrea L. Foster, Emily G. Wright, Stacy C. Bennett, Krishangi D. Groover, and John A. Izbicki

Prepared in cooperation with the Lahontan Regional Water Quality Control Board

Professional Paper 1885-I

U.S. Department of the Interior
U.S. Geological Survey

U.S. Geological Survey, Reston, Virginia: 2023

Suggested citation:
Miller, L.G., Bobb, C.E., Foster, A.L., Wright, E.G., Bennett, S.C., Groover, K.D., and Izbicki, J.A., 2023, Sequestration and reoxidation of chromium in experimental microcosms, Chapter I of Natural and anthropogenic (human-made) hexavalent chromium, Cr(VI), in groundwater near a mapped plume, Hinkley, California: U.S. Geological Survey Professional Paper 1885-I, 72 p., https://doi.org/10.3133/pp1885I.

Associated data for this publication:
Foster, A.L., Wright, E.G., Bobb, C., Choy, D., and Miller, L.G., 2023, Optical petrography, bulk chemistry, micro-scale mineralogy/chemistry, and bulk/micron-scale solid-phase speciation of natural and synthetic solid phases used in chromium sequestration and re-oxidation experiments with sand and sediment from Hinkley, CA: U.S. Geological Survey data release, https://doi.org/10.5066/P9ENBLGY.

Groover, K.D., and Izbicki, J.A., 2018, Field portable X-ray fluorescence and associated quality control data for the western Mojave Desert, San Bernardino County, California: U.S. Geological Survey data release, https://doi.org/10.5066/P9CU0EH3.

Miller, L.G., Bobb, C., Bennett, S., and Baesman, S.M., 2020, Aqueous and solid phase chemistry of sequestration and re-oxidation of chromium in experimental microcosms with sand and sediment from Hinkley, CA: U.S. Geological Survey data release, https://doi.org/10.5066/P9U8C82V.

Morrison, J.M., Benzel, W.M., Holm-Denoma, C.S., and Bala, S., 2018, Grain size, mineralogic, and trace-element data from field samples near Hinkley, California: U.S. Geological Survey data release, https://doi.org/10.5066/P9HUPMG0.

ISSN 2330-7102 (online)

Acknowledgments

This study was developed by the U.S. Geological Survey (USGS) with input from a technical working group (TWG) composed of community members, the Lahontan Regional Water Quality Control Board (RWQCB), the Independent Review Panel Manager (Project Navigator, Ltd.), Pacific Gas and Electric Company (PG&E), and consultants for PG&E. The study was funded cooperatively under an agreement between the Lahontan RWQCB and the USGS. Funding for the study was provided by PG&E to the Lahontan RWQCB. Logistical support for field work, including access to wells, was provided by PG&E. The TWG met approximately quarterly during the study to provide input to the study, and the Hinkley community was updated annually on study progress.

The authors thank the many people involved in the design and implementation of this study including the staff of the Lahontan RWQCB, the staff of PG&E and their consultants, and the staff of Project Navigator, Ltd. Specifically the authors thank Margie Gentile of ARCADIS and Betsy Brunswick of PG&E for discussions in preparation for our experiments and Iain Baker and Kevin Sullivan of PG&E for providing the core material from SA-SB-01. The authors thank Doug Choy (USGS, Menlo Park, California) of the Reston Stable Isotope Laboratory for organic carbon analysis. The authors also acknowledge and thank the many involved community members who collectively donated thousands of hours on behalf of the local community in support of this project and for resolution of other issues related to anthropogenic hexavalent chromium, Cr(VI), within the Hinkley area.

Contents

Figures

Tables

Conversion Factors

International System of Units to U.S. customary units

Multiply	By	To obtain
	Length	
centimeter (cm)	0.3937	inch (in.)
millimeter (mm)	0.03937	inch (in.)
micrometer (µm)	0.00003937	inch (in.)
angstrom (Å)	0.000000003937	inch (in.)
nanometer (nm)	0.00000003937	inch (in.)
meter (m)	3.281	foot (ft)
kilometer (km)	0.6214	mile (mi)
meter (m)	1.094	yard (yd)
	Volume	
liter (L)	0.2642	gallon (gal)
milliliter (mL)	0.0338	fluid ounce (oz.)
microliter (µL)	0.00003381	fluid ounce (oz.)
	Mass	
gram (g)	0.03527	ounce, avoirdupois (oz)
kilogram (kg)	2.205	pound avoirdupois (lb)
	Concentration	
nanogram per gram (ng/g)	0.000000016	ounces per pound
	Pressure	
Torr	0.0193	pound per square inch (psi)
	Flow Rate	
milliliter per minute (mL/min)	0.016	gallon per hour (gph)

U.S. customary units to International System of Units

Multiply	By	To obtain
	Length	
inch (in.)	2.54	centimeter (cm)
inch (in.)	25.4	millimeter (mm)
foot (ft)	0.3048	meter (m)
mile (mi)	1.609	kilometer (km)
	Volume	
gallon (gal)	3.785	liter (L)
	Mass	
ounce, avoirdupois (oz)	28.35	gram (g)
pound, avoirdupois (lb)	0.4536	kilogram (kg)

Temperature in degrees Celsius (°C) may be converted to degrees Fahrenheit (°F) as follows:

$$°F = (1.8 \times °C) + 32.$$

Datum

Vertical coordinate information is referenced to the North American Vertical Datum of 1988 (NAVD 88).

Horizontal coordinate information is referenced to the North American Datum of 1983 (NAD 83).

Below land surface (bls) is the datum used to describe depth.

Supplemental Information

Additions to microcosms during the study are described on a volume per volume (v/v0 and a weight per weight (w/w) basis.

Ampere is the base unit for electric current in the Standard International (SI) system of units. A milliampere (mA) is one thousandth of an ampere.

Concentrations of chemical constituents in water are given in either milligrams per liter (mg/L) or micrograms per liter (µg/L).

Concentrations of chemical constituents in solid material are given in milligrams per kilogram (mg/kg).

Electron volt (eV) is the measure of an amount of kinetic energy gained by a single electron accelerating from rest through an electric potential difference of one volt in a vacuum. A gigaelectron volt is 109 eV.

One mole is 6.02214076×1023 units of a substance. Millimolar, or millimoles per liter (mM), is one thousandth of a mole of a substance in one liter of solvent.

Results for measurements of stable isotopes of an element in water, solids, and dissolved constituents commonly are expressed as the relative difference in the ratio of the number of the less abundant isotope (iE) to the number of the more abundant isotope of a sample with respect to a measurement standard.

Redox, a combination of the words reduction and oxidation, refers to chemical processes in which one substance or molecule gains an electron (is reduced and its oxidation state is decreased) and another loses an electron (is oxidized and its oxidation state is increased). The processes of oxidation and reduction occur simultaneously and cannot occur independently.

Abbreviations

±	plus or minus
µXANES	micro-X-ray absorption near edge structure
µXRF	micro X-ray fluorescence
µRaman	micro-Raman
Å	angstrom
Au	gold
BSE	backscattered electron

C	carbon
Ca	calcium
Cr	chromium
Cr(III)	trivalent chromium having an oxidation state of +3
Cr(VI)	hexavalent chromium having an oxidation state of +6
Dil	dilution
DPC	diphenylcarbazide
EDS	energy dispersive spectroscopy
EPA	U.S. Environmental Protection Agency
EPPS	N-(2-Hydroxyethyl)piperazine-N′-(3-propanesulfonic acid)
EtOH	ethyl alcohol
EXAFS	extended X-ray absorption fine structure
Fe	iron
Fe(II)	ferrous iron having an oxidation state of +2
Fe(III)	ferric iron having an oxidation state of +3
$FeCr_2O_4$	chromite
G	Gravitational constant
Ge	germanium
h	Planck's constant
HCl	hydrochloric acid
HEPES	4-(2-hydroxyethyl)-1-piperazineethanesulfonic acid
HFO	hydrous ferric oxide
HNO_3	nitric acid
ICP-MS	inductively coupled plasma-mass spectrometry
IRZ	in situ reactive zone
ISR	in situ reduction
K	potassium
k	photoelectron wave vector
$K_2Cr_2O_7$	potassium dichromate
KOH	potassium hydroxide
LED	light-emitting diode
$MgCl_2$	magnesium chloride
Mn	manganese
Mn(II)	manganese having an oxidation state of +2
Mn(III)	manganese having an oxidation state of +3

Mn(IV)	manganese having an oxidation state of +4
MnO_2	manganese oxide
MOPS	3-(N-morpholino) propanesulfonic acid
N	normal
N_2	nitrogen
NaOH	sodium hydroxide
O_2	oxygen
PG&E	Pacific Gas and Electric Company
PIPS	passivated implanted planar silicon
pXRF	portable X-ray fluorescence
Q4 2015	October–December 2015
R^2	coefficient of determination
RDF	radial distribution function
RPM	revolutions per minute
RWQCB	Regional Water Quality Control Board
S	sulfur
SE	secondary electron
SEM	scanning electron microscopy
Si	silicon
SO_4^{-2}	sulfate
SSRL	Stanford Synchrotron Radiation Lightsource
TIFF	tagged image file format
USGS	U.S. Geological Survey
x	times
XANES	X-ray absorption near edge structure
XAFS	X-ray absorption fine structure
XAS	X-ray absorption spectroscopy
XRD	X-ray powder diffraction
XRF	X-ray fluorescence
µXAS	micro-X-ray absorption spectroscopy
Z	atomic number, the charge number of an atomic nucleus

Sequestration and Reoxidation of Chromium in Experimental Microcosms

By Laurence G. Miller, Callum E. Bobb, Andrea L. Foster, Emily G. Wright, Stacy C. Bennett, Krishangi D. Groover, and John A. Izbicki

Abstract

Groundwater containing hexavalent chromium, Cr(VI), downgradient from the Pacific Gas and Electric Company (PG&E) Hinkley compressor station in the Mojave Desert, 80 miles northeast of Los Angeles, California, is undergoing bioremediation using added ethanol as a reductant in a volume of the aquifer defined as the in situ reactive zone (IRZ). This treatment reduces Cr(VI) to trivalent chromium, Cr(III), which is rapidly sequestered by sorption to aquifer particle surfaces and by co-precipitation within iron (Fe) or manganese (Mn) bearing minerals forming in place as reduction proceeds. Successful mitigation of the Cr(VI) plume is projected to require 10–95 years, at which time bioremediation with ethanol will likely cease. This projection assumes that Cr(VI) removal is permanent and that no Cr(III) will oxidize back to Cr(VI) in the event of changing hydrologic conditions that may cause oxygen-rich water to re-enter the IRZ. Laboratory microcosm experiments were done to explore the process of reductive sequestration of Cr(VI) to Cr(III) and the potential for reoxidation of Cr(III) to Cr(VI).

In reductive sequestration experiments, batch microcosms were prepared with aquifer materials collected from sites upgradient of the Cr(VI) regulatory plume. Control microcosms were prepared using Fe- and Mn-coated quartz sand. Unfiltered Mojave River groundwater containing an added tracer of isotopically labeled chromium-50 were reacted with microcosm materials for up to 2 years; during this time, bio-reduction was stimulated by repeated additions of diluted ethanol to maintain reduced conditions within appropriate ranges, avoiding sulfate reducing or methanogenic conditions as much as possible while mimicking field conditions. Analysis of chromium-50, Fe, and Mn obtained by sequential extraction from microcosms harvested (incubation terminated and microcosm contents analyzed) at various times showed that some aqueous chromium (Cr) was sorbed to particle surfaces within hours; reduction to Cr(III) and incorporation into amorphous and crystalline solid phases occurred during the next few months. Amorphous Cr-containing fractions included Fe and Mn hydroxides and organic matter. Ultimately, most of the chromium-50 tracer was present in the less reactive crystalline phase. However, Fe and Mn were broadly distributed at later stages of reduction, and both were spatially co-located with Cr on a micrometer (μm) scale. Solid-phase data collected using scanning electron microscopy with energy dispersive spectroscopy (SEM-EDS) and X-ray absorption spectroscopy (XAS) indicated that some Cr(III) was associated with mixed valence Fe oxides like magnetite and Fe-Mn oxides like jacobsite. Additionally, Cr(III) was observed within several μm of Fe and Mn embedded in clays and in mineral coatings.

To evaluate the potential for reoxidation of Cr(III) to Cr(VI), additional batch microcosms of aquifer materials and mixtures of Fe- and Mn-coated sand were first reduced for more than 1 year and subsequently oxidized for almost 2 years. Hexavalent chromium was formed and was available for release to the aqueous phase during oxidation of all materials; however, the timing and amount of Cr(VI) formed and released varied among substrates. Artificial substrates containing more Mn produced more Cr(VI). Site material characteristic of recent Mojave River deposits contained within the IRZ produced the least Cr(VI) during oxidation, while site materials composed of older Mojave River aquifer material (containing more Mn) produced more Cr(VI). Site material collected from within the IRZ contained more Cr but produced an intermediate amount of Cr(VI) following oxidation. The combined results of microcosm chemistry and solid-phase analyses showed that the nature and locus of Cr(III) sequestration influenced its vulnerability to reoxidation to Cr(VI). It was concluded that co-location of Cr with Mn at later stages of reduction influenced the susceptibility of Cr(III) to reoxidation in microcosms.

Reoxidation of Cr(III) to Cr(VI) was observed in experiments with previously reduced material after just 14 days exposure to oxygen. As much as 10 percent of added Cr was oxidized to Cr(VI) in microcosms prepared using recent Mojave River aquifer material, and as much as 20 percent of added Cr was oxidized to Cr(VI) in microcosms prepared using older Mojave River aquifer material. Less Cr(VI) (less than 3 percent of Cr added before reduction) was released to the aqueous phase, and this release occurred following longer oxygen exposure. Site managers may need to plan for long-term monitoring and the possibility of active maintenance of anoxic conditions within the IRZ to ensure permanent sequestration of Cr after bioremediation with ethanol ceases.

I.1. Introduction

The Pacific Gas and Electric Company (PG&E) Hinkley compressor station, in the Mojave Desert, 80 miles (mi) northeast of Los Angeles, California, is used to compress natural gas as it is transported through a pipeline from Texas to California. Between 1952 and 1964, cooling water used at the Hinkley compressor station was treated with a compound containing hexavalent chromium, Cr(VI), to prevent corrosion of machinery in the compressor station. Cooling wastewater containing Cr(VI) was discharged to unlined ponds, releasing Cr(VI) to soil and groundwater in the underlying unconsolidated aquifer (Lahontan Regional Water Quality Control Board, 2013). Since 1964, cooling-water management practices that do not release chromium (Cr) into groundwater have been used at the site.

Groundwater downgradient from the Hinkley compressor station is undergoing bioremediation using added ethanol as a reductant in a volume of the aquifer within the regulatory Cr(VI) plume (ARCADIS, 2016) defined as the in situ reactive zone (IRZ; Lahontan Regional Water Quality Control Board, 2015). Successful mitigation of Cr(VI) within the plume is projected to require 10–95 years (Haley and Aldrich, Inc., 2010; Pacific Gas and Electric Company, 2011), at which time ethanol loading will likely cease. This projection assumes that Cr(VI) removal is permanent and that no trivalent chromium, Cr(III), will oxidize back to Cr(VI) in the event of changing hydrological conditions causing oxygen-rich water to re-enter the IRZ.

The U.S. Geological Survey (USGS) was requested by the Lahontan Regional Water Quality Control Board to complete an updated background study of background Cr(VI) concentrations in Hinkley and Water Valleys. As part of the updated background study, the USGS was requested to do a series of experiments to evaluate the sequestration and potential for reoxidation of Cr(VI) from aquifer materials within the IRZ downgradient from the Hinkley compressor station.

I.1.1. Background

Hexavalent chromium is toxic and mutagenic and thus presents a serious risk to biota and human health (Fendorf and others, 2000; Saha and others, 2011). It is present in groundwater primarily as chromate oxyanions ($HCrO_4^{-1}$ or CrO_4^{-2}), which are weakly sorbed to particle surfaces at circumneutral pH and desorbed as pH increases to alkaline values (Kent and others, 1994; Hausladen and others, 2018). Hence, Cr(VI) is generally soluble and may pose a risk for migration to domestic and public water supplies (Mills and others, 2011). Anthropogenic sources of Cr(VI) include accidental or deliberate release from tanneries, electroplating facilities and other industrial processes (including metallurgy), wood preservation, and anti-corrosion practices (Saha and others, 2011). Wastes from these activities are the source of anthropogenic Cr in soil and groundwater at more than 1,300 sites in the United States alone (Fruchter, 2002). Typically, lower levels of naturally occurring aqueous Cr(VI) originate from slow oxidation of chromite ($FeCr_2O_4$) and other trivalent chromium-, Cr(III), bearing minerals present in the subsurface (Schroeder and Lee, 1975; Oze, and others, 2007). Oxidation of Cr(III) is accelerated by its reaction with ubiquitous manganese (Mn) oxides (Bartlett and James, 1979; Eary and Rai, 1987; Fandeur and others, 2009b; Namgung and others, 2014; Hausladen and Fendorf, 2017). Most hydrogeologic settings contain sufficient oxidized Mn for this process to occur (Tang and others, 2014).

Bioremediation is a common strategy for removing anthropogenic metals from groundwater (Lovley and Coates, 1997; Tokunaga, and others, 2003) whereby injection of a soluble electron donor stimulates the extant microbial community. Bio-reduction is remediation that drives dissimilatory metabolic processes to reduce various electron acceptors including nitrate, nitrite, iron (Fe), Mn, and sulfate (SO_4^{-2}). Conversion of Cr(VI) to Cr(III) also may be stimulated (Faybishenko and others, 2008; Jobby and others, 2018). The Cr(III) produced is less toxic and less soluble than Cr(VI), which facilitates its removal from solution. Thus, the aim of bio-reduction of Cr(VI) is to provide sufficient reducing potential to the system to convert all Cr(VI) to Cr(III). Although clearly mediated by microbes, the mechanism of Cr(VI) reduction is largely unknown. Hexavalent chromium may be directly reduced via chromium-reductase enzymes (Lovley, 1993; Lovley and Phillips, 1994) or similar enzymes (Marsh and others, 2000; Thatoi and others, 2014), or it may be abiotically reduced by reduced Fe or sulfur (S) species that also are products of dissimilatory reduction (Eary and Rai, 1989; Fendorf and others, 2000, Beller and others, 2014).

Hexavalent chromium is immobilized or sorbed to aquifer materials by several mechanisms. Hexavalent chromium may be weakly sorbed (and potentially more reactive), more strongly sorbed (and potentially less reactive), complexed with organic matter, or further sequestered by incorporation into the crystalline structure of silicates or Fe and Mn oxyhydroxides, hydroxides, or oxides (hereafter referred to more simply as hydroxides) precipitating on or within the mineral grains that compose the aquifer. Sorption is pH dependent, with stronger sorption under circumneutral and slightly acidic conditions and weaker sorption under alkaline conditions. Sorption may change with time as weakly sorbed Cr incorporates into less reactive fractions.

The nature and location of Cr sequestration likely determines its vulnerability to reoxidation (Sass and Rai, 1987). Examination of core material collected within the regulatory Cr(VI) plume and within IRZ treated portions of the plume shows massive accumulations of Fe- and Mn-containing hydroxides co-located on mineral grain surfaces and shows fine-scale accumulations of Fe- and Mn-containing hydroxides distributed on mineral grains in a spider-web manner at otherwise imperceptible lithologic contacts within the Cr(VI) regulatory plume (chapter C). These hydroxides contain a high fraction of weakly sorbed, potentially reactive Cr; similar hydroxide accumulations were not observed at sites outside the mapped Cr(VI) regulatory plume (chapter C).

I.1.2. Fate of Chromium During and After In Situ Reduction

Bioremediation of groundwater at Hinkley, California (chapter A), occurs by injection of ethanol into the Cr(VI) plume to create anoxic conditions (dissolved oxygen absent) in a volume of aquifer defined as the IRZ (Lahontan Regional Water Quality Control Board, 2015). The updated U.S. Geological Survey (USGS) background study included a series of laboratory microcosm studies designed to determine if Cr is permanently removed from solution by reactions occurring within the IRZ or if future changes in hydrology (for example, large amounts of groundwater recharge from the Mojave River) that result in oxic conditions (dissolved oxygen present) can convert Cr(III) back to Cr(VI) and allow Cr(VI) to re-enter groundwater (chapter A, table A.2). The purpose and scope of the microcosm studies were described by Izbicki and Groover (2016, 2018).

Several factors may control the mobility of Cr that was previously reduced and sorbed to or precipitated (sequestered) within aquifer materials comprising the IRZ. Two factors evaluated in the laboratory include (1) changes to the fraction or phase in which Cr is sequestered over time during reduction and (2) whether sorbed Cr(III) could be reoxidized to Cr(VI) and released to the aqueous phase. Five experiments were carried out to elucidate these processes (table I.1). The first four experiments were designed to determine what Cr(III)-bearing fractions likely form during in situ reduction (ISR). The preliminary experiment was designed to test the methodology. The reduction experiment was designed to follow the added Cr tracer, chromium-50, through various fractions over time. A sterile washed sand experiment was designed to determine if Cr sequestration was controlled by biotic or abiotic factors. Finally, the elevated Cr reduction experiment was needed to obtain enough Cr product in sequestered phases to observe with the instruments available. The single oxidation experiment was designed to determine whether Cr sequestered during more than a year of reduction was vulnerable to reoxidation and to determine the time scales of reoxidation.

A range of site materials including native material from representative sites with similar hydrogeochemical properties and material from within the IRZ that had previously been reduced in situ using ethanol were evaluated. These materials were used to ascertain the role that aquifer geology plays in sequestering and releasing Cr. The impact of Fe- and Mn-surface coatings was further evaluated by including a suite of artificial substrates. Finally, replicate assays of all samples were included at every timepoint during the incubations to assess variability in the rates of biogeochemical processes. The hundreds of incubations required for this scheme allowed for examination of multiple variables with a high degree of confidence, but they precluded the use of flow-through laboratory columns for this study. Flow-through columns may better represent the conditions of the aquifer because soluble reaction products are removed by advection. Batch microcosms are useful for evaluating the importance of reactions and for evaluating mass balances of reactants and products.

I.1.3. Purpose and Scope

The purpose of this chapter was to evaluate the fate of Cr during and after in situ reduction and determine if Cr within the IRZ may reoxidize or is permanently removed from groundwater (chapter A, Task 8, table A.2). The experiments were previously described by Izbicki and Groover (2016, 2018). The U.S. Geological Survey was requested by the Lahontan Regional Water Quality Control Board (RWQCB) to do these experiments as part of the updated Cr(VI) background study. This work was funded by the Lahontan RWQCB with financial support from PG&E.

The scope of the work included a long-term (2-year) reduction experiment and a long-term (2-year) oxidation experiment. Material used in the oxidation experiment was reduced for 1.25 years prior to the onset of the experiment. The reduction and oxidation experiments were preceded by a short-term (146-day) preliminary experiment. The results of the preliminary experiment were used to evaluate and optimize the design of the reduction and oxidation experiments.

Table I.1. Overview of microcosm experiments.

[Data about the natural materials used are available in Miller and others (2020b) and in chapter C within this professional paper. **Abbreviations**: Fe, iron; Mn, manganese; mL, milliliters; wt., weight; g, grams; Cr(VI), hexavalent chromium; µg/L, microgram per liter; *, denotes material used in microcosm; —, no data; Cr, chromium; ft, foot; bls, below land surface; N, Normal; HCl, hydrochloric acid;]

Experiment	Site materials				Artificial substrates						Microcosm volume (mL)	Liquid volume (mL) solid wt. (g)	Initial aqueous Cr(VI) (µg/L)	Number of sterile controls
	SA-RW-34[1]	BG-0004[2]	BG-0005[3]	SA-SB-01[4]	Washed sand[5]	Fe sand[6]	Mn sand[7]	Fe/Mn 100[8]	Fe/Mn 50[9]	Fe/Mn 25[10]				
Preliminary	*	—	—	—	—	—	—	—	—	—	36	15/10	500	2
Reduction	—	*	*	—	*	*	—	—	—	—	56	30/10	1,000	0
Sterile washed sand	—	—	—	—	*	—	—	—	—	—	56	30/10	1,000	4
Elevated Cr reduction	—	*	*	—	*	—	—	—	*	—	56	50/5	1,000	0
Oxidation	—	*	*	*	—	*	*	*	*	*	56	30/10	1,000	0

[1]Older Mojave River aquifer/lake margin, 92–96 ft bls.

[2]Recent Mojave River aquifer, 53.0–61.2 ft bls.

[3]Older Mojave River aquifer, 104.0–114.5 ft bls.

[4]Anoxic aquifer material from the in situ reduction zone, 103–108 ft bls.

[5]Acid (6N HCl) washed Ottawa sand.

[6]Washed Ottawa sand with physisorbed hydrous ferric oxide.

[7]Washed Ottawa sand with physisorbed manganese oxide.

[8]Mixed Fe sand and Mn sand (Fe/Mn 100).

[9]Mixed Fe sand and Mn sand (Fe/Mn 50).

[10]Mixed Fe sand and Mn sand (Fe/Mn 25).

More than 380 experimental microcosms were prepared in 30 milliliter (mL) or 50 mL serum bottles and analyzed as part of this study. Microcosms consisted of fresh site material (or artificial substrates used as study controls) and native groundwater sampled from wells upgradient from the Hinkley compressor station. Artificial substrates (consisting of various mixtures of Fe- and Mn-coated sand grains) were included as controls for comparison with aquifer site materials in microcosm experiments. Chromium-50 was added to trace the fate of Cr within study microcosms. Selected microcosms were sterilized to evaluate microbial processes occurring within unsterilized microcosms. Headspace gasses were monitored within the microcosms to ensure desired environmental conditions were maintained during the experiments. Microcosms were harvested at selected times, and Cr and other elements were analyzed within the aqueous phase and within phases extractable from surface coatings on particle surfaces within the microcosms. Minerals composing surface coatings on particles within the harvested microcosms also were analyzed using a variety of techniques.

Microcosm experiments do not simulate all aspects of field settings where dissolved materials may move downgradient with groundwater. However, results from microcosm experiments can be used to evaluate processes controlling reduction of Cr(VI) to Cr(III) at the mineral-grain scale, and to evaluate the potential for reoxidation of Cr(III) to Cr(VI) if environmental conditions change.

I.2. Methods

The reduction and oxidation experiments were done between June 2015 and December 2019. The study design included a 146-day preliminary experiment, done between June and November 2015, to evaluate and optimize the design of the reduction and oxidation experiments.

Site materials for microcosm experiments were obtained from freshly drilled core material collected using an auger rig at sites BG-0004, BG-0005, SA-RW-34 and SA-SB-01 (fig. I.1). Sites BG-0004 and BG-0005 are upgradient of the Hinkley compressor station. Site BG-0004 is located in the incised alluvial channel of the Mojave River. The core material collected from 53 to 61.2 feet below land surface (ft bls) was composed of recent Mojave River deposits. Site BG-0005 is located on an upland alluvial terrace. The core material collected from 104 to 114.5 ft bls was composed of older Mojave River deposits. In general, older Mojave River deposits partly eroded from mafic rock in the San Gabriel Mountains (about 40 mi southwest of Hinkley Valley, not shown on fig. I.1) contain more Cr, Fe, and Mn than recent Mojave River deposits (chapters B and C). Sites SA-RW-34 and SA-SB-01 are located in Mojave River deposits downgradient from the Hinkley compressor station within the regulatory Cr(VI) plume. Most core material was oxic and only required protection from ambient and microbial contamination prior to use; core material collected at SA-SB-01 was within the IRZ and anoxic conditions within this core were maintained during sample collection, handling, shipment to the laboratory, and storage prior to use.

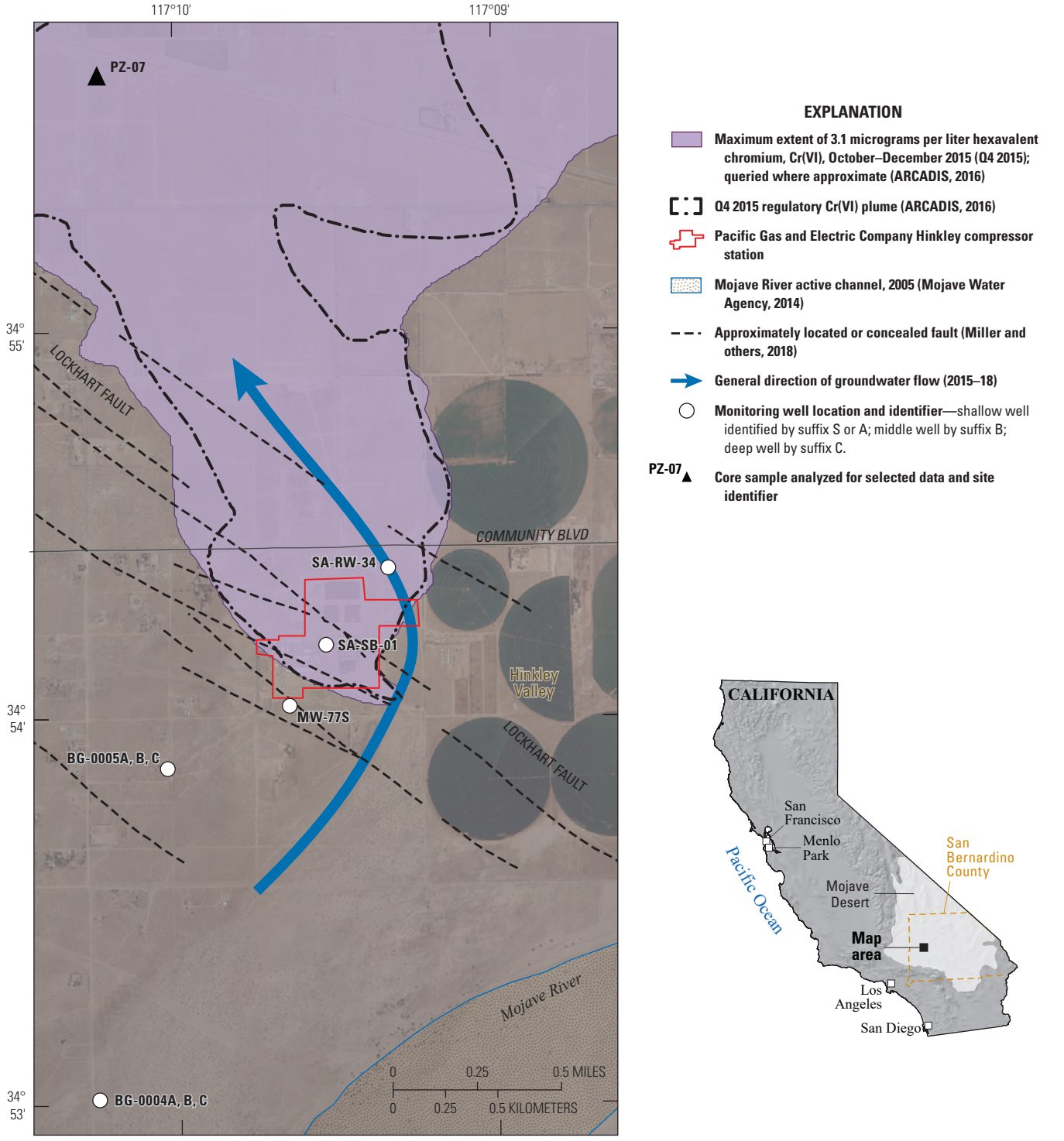

Base from U.S. Geological Survey and other Federal and State digital data, various scales; Lambert Conformal Conic projection, standard parallels are 34.0333° N. and 35.4667° N.; North American Datum of 1983

Figure I.1. Locations of sites sampled in Hinkley Valley, San Bernardino County, California, with respect to the regulatory hexavalent chromium, Cr(VI), plume and the Pacific Gas and Electric Company (PG&E) compressor station. Site information is available in ARCADIS (2016).

The depositional history of older and recent Mojave River deposits in Hinkley Valley is presented in chapter A within this professional paper and discussed by Miller and others (2018, 2020a). Lithologic and provenance descriptions of these materials are available in Miller and others (2020a) and Groover and Izbicki (2019); elemental and mineralogic analyses of these materials are available in Groover and Izbicki (2018) and Morrison and others (2018) and discussed in chapters B and C within this professional paper. Groundwater flow in Hinkley Valley is from recharge areas along the Mojave River downgradient to the north (Stamos and others, 2001; Jacobs Engineering Group, Inc., 2019). Predevelopment (pre-1930) and 2017 depth to water and water-level contour maps are provided in chapter H within this professional paper (chapter H, figs. H.8*A–D*). The Lockhart fault impedes the movement of groundwater near the Hinkley Compressor station. The extent of the Q4 2015 (October–December 2015), regulatory Cr(VI) plume is from ARCADIS (2016; fig. I.1).

Water for microcosm experiments was obtained from wells MW-77S and BG-0004A, upgradient from the Hinkley compressor station (fig. I.1). Both wells were representative of uncontaminated native groundwater upgradient of the Q4 2015 regulatory Cr(VI) plume. Water from wells upgradient from the Hinkley compressor station was oxic, slightly alkaline, and typical of native (uncontaminated) groundwater recently recharged from the Mojave River. Additional analyses of water from these wells are available in chapter E within this professional paper (chapter E, appendix E.1, table E.1.1).

I.2.1. Preliminary Experiment

A short-term (146 day) reduction experiment was done between June and November 2015 to evaluate and optimize the reduction strategy used for later experiments. The preliminary experiment was designed to test (1) the optimal dose rate of ethanol required to ensure rapid reduction, (2) the progress of key redox reactions influencing Cr, and (3) the desirability of adding organic buffers to control pH. These tests were completed on slurries of aquifer material using 10 grams (g) of material from site SA-RW-34 (table I.1; fig. I.1) located within the regulatory Cr(VI) plume, downgradient from the Hinkley compressor station but not within the IRZ.

I.2.1.1. Sample Preparation and Incubations

Slurries were prepared in 30 mL serum bottles (stoppered volume=36 mL) using 15 mL unfiltered oxic (contains dissolved oxygen) water from well MW-77S (table I.2), representative of uncontaminated native groundwater upgradient of the regulatory Cr(VI) plume. To minimize pH changes during the experiment, all but one of the microcosms received additions of organic buffers HEPES [4-(2-hydroxyethyl)-1-piperazineethanesulfonic acid]; MOPS [3-(N-morpholino) propanesulfonic acid]; or EPPS [N-(2-Hydroxyethyl)piperazine-N′-(3-propanesulfonic acid)] to achieve final concentrations of 10 millimolar (mM, millimoles per liter) and 50 mM each. Controls were prepared without aquifer material using deionized water or with a mixture of aquifer material and site water that had been sterilized by gamma irradiation. A Cr spike consisting of 0.05 mL of 150 milligrams per liter (mg/L) of potassium dichromate ($K_2Cr_2O_7$) in deionized water was added to each microcosm to create an initial concentration of 0.5 mg/L Cr, before sealing the bottles with butyl rubber stoppers. No replicates were prepared.

Microcosms were reduced by stimulating microbial activity using repeated additions of 88 microliters (µL) of 1 percent volume per volume (v/v) ethanol (to approximately 1 mM ethanol aqueous concentration). Ethanol additions occurred every 3–5 days for several weeks, followed by less frequent additions (weekly) during the next several months. Controls received fewer additions of ethanol because it was not consumed. Incubations were maintained with gentle shaking in the dark at 22 degrees Celsius (°C) for nearly 5 months.

Table I.2. Characteristics of native groundwater from wells MW-77S and BG-0004A.

[Samples collected January 13, 2016, and analyzed at the U.S. Geological Survey Environmental Geochemistry and Geomicrobiology Laboratory in Menlo Park, California. Additional water chemistry data are available in chapter E (appendix E.1, table E.1.1). **Abbreviations**: ft bls, foot below land surface; mg/L milligram per liter; µS/cm, microSieman per centimeter; °C, degrees Celsius; $CaCO_3$, calcium carbonate; SO_4^{-2}, sulfate; Fe, iron; µg/L microgram per liter; <, less than; Cr(VI), hexavalent chromium; NO_3^-, nitrate; NO_2^-, nitrite; NH_4^+, ammonium; N_{org}, organic nitrogen]

Characteristic	MW-77S	[1]BG-0004A
Screened depth of well (ft bls)	80–100	58–68
Depth of water sample (ft bls)	82	65
pH	7.8	8.0
Dissolved oxygen (mg/L)	6.9	6.3–6.8
Specific conductance (µS/cm at 25 °C)	556	837–844
Total dissolved solids (mg/L)	339	522–527
Alkalinity (mg/L as $CaCO_3$)	125	164–166
SO_4^{-2}(mg/L)	64.7	119–120
Total nitrogen (mg/L)[2]	1.00	4.94–5.19
Fe(II) + Fe (III) (µg/L)[3]	5.6	<4.0
Cr(VI) (µg/L)	0.9	2.3–3.1

[1]Values show the range of duplicate analyses of BG-0004A.

[2]Total nitrogen = ($NO_3^- + NO_2^- + NH_4^+ + N_{org}$).

[3]Dissolved Fe only.

I.2.1.2. Headspace and Aqueous Phase Analyses

Headspace oxygen (O_2) within microcosms was sampled initially and approximately weekly thereafter by syringe through 25-gauge needles. Headspace O_2 was determined by electron capture detection-gas chromatography (ECD-GC) using a molecular sieve 5A (5-micrometers, µm) column (3.2 millimeters, mm, outer diameter by 2.4 meters, m) operated at 75 °C using a hydrocarbon-free, ultra-high-purity nitrogen gas (N_2) carrier. Background O_2 was minimized by flushing syringes and needles with O_2-free N_2 before sampling. The detection limit was 0.05 millimoles (mmol) of O_2 /L. Headspace values were converted to total O_2 (aqueous plus headspace) using liquid and gas phase volumes and a dimensionless Henry's Law constant of 31.44.

Aqueous samples (1 mL) were collected for analysis of pH, SO_4^{-2} and dissolved metals (Cr, Fe, and Mn) initially and after 1 week, then again after 2 months, and about monthly thereafter. An Orion pH meter with a Ross micro-electrode, calibrated daily with pH=10 and pH=7 buffers, was used to monitor pH. Dissolved Cr(VI) was measured by colorimetric spectrophotometry using the diphenylcarbazide (DPC) method, U.S. Environmental Protection Agency (EPA) Method 7196 (U.S. Environmental Protection Agency, 1992). Colorimetry was confined to 1.5 mL volume plastic cuvettes (ultraviolet transparent) by sequentially pipetting 0.125 mL DPC (made fresh monthly) and 1.0 mL sample or standard and allowing it to react for 20 minutes. Absorbance was determined over a 1-centimeter (cm) pathlength using a Thermo Scientific Genesys 20 spectrophotometer at a wavelength of 540 nanometers (nm). Standards were prepared by serial dilution of a potassium dichromate stock solution.

Dissolved SO_4^{-2} was measured on diluted (1:10 with deionized water) samples using a Dionex ICS-2000 ion chromatograph with conductivity detection (Oremland and others, 2002), configured with a Dionex AS-18 column, and using 32 mM potassium hydroxide (KOH) mobile phase flowing at 1.0 mL per minute (mL/min). Dissolved Fe and Mn were determined on diluted (1:10) samples by established colorimetric methods, using the spectrophotometer described in the previous paragraph. Iron, as Fe(II), and total Fe were measured by the ferrozine method (Stookey, 1970) before and after reduction by hydroxylamine hydrochloride (Viollier and others, 2000). Dissolved Mn was measured following reduction by hydroxylamine hydrochloride using the formaldoxime method of Brewer and Spencer (1971) as modified by Armstrong and others (1979) for small samples. Standards were prepared by serial dilution of certified atomic absorption standards.

I.2.2. Reduction Experiments

Batch reactor microcosms were prepared in 50 mL serum bottles to study the effects of extended (2 year) anoxic conditions upon Cr reduction and sequestration; these included incubations of (table I.1) native aquifer (site) materials sampled at depth at two locations upgradient of the IRZ (BG-0004 and BG-0005) and sieved to less than 2 mm diameter, acid washed Ottawa sand (washed sand), and acid washed Ottawa sand coated with hydrous iron [Fe(III)] oxide (Fe sand; see section "I.2.2.1 Preparation of Artificial Substrates" for details of artificial substrate preparation). Washed sand and Fe sand were included as controls to compare with site materials in studying the fate of Cr and the influence of Fe on rates of Cr reduction.

The naturally occurring stable isotopes of Cr (chromium-50 and chromium-54) were added at the outset of incubations to track the sequestration of Cr by aquifer materials and characterized artificial substrates through time within experimental microcosms. Chromium-50 and chromium-54 are less abundant than other naturally occurring stable isotopes of Cr, chromium-52 and chromium-53 (chapter F). Chromium-54 was less useful to track the sequestration of Cr than chromium-50 because of interference with a stable isotope of Fe, iron-54, during analysis; therefore, only results using chromium-50 are discussed. Tracking was accomplished by following chromium-50 though sequential extractions. Recovery of the tracer in various fractions indicated the degree of mineralization of Cr. Site material (10 g, field moist, table I.1) and native groundwater from BG-0004A (30 mL, unfiltered, table I.2) were combined and sealed with butyl rubber stoppers. Site materials harbored additional extant microbes, but artificial substrates did not harbor extant microbes.

All incubations were maintained in the dark at 22 °C in oxic and anoxic conditions; however, only results for the anoxic incubations are reported because little difference was observed in Cr(VI) reduction between these conditions (data not shown). Glassware and plasticware were washed using 6 Normal (N) hydrochloric acid (HCl), rinsed six times in deionized water, and air dried before use.

To begin the incubations, Cr(VI) stock containing about 50 percent chromium-50 was added to a final aqueous Cr concentration of 1 mg/L, which is within the range of Cr concentrations found within the Q4 2015 regulatory Cr(VI) plume (ARCADIS, 2016) and equivalent to 1,600 nanograms (ng) chromium-50 per g of aquifer material. All samples received additions of 88 µL of 1 percent weight per weight (w/w) ethanol (to 1 mM) using a sterile technique approximately weekly for 3 months, followed by less frequent (monthly) additions. Triplicate samples were harvested immediately after the microcosms were prepared and at selected times (41, 83, 168, 350, and 720 days) after the start of the experiment. One sample of each type of reacted material (site material, washed sand, and Fe sand) from every timepoint was immediately frozen at −80 °C for later use in solid-phase studies. The remaining duplicate samples were designated for sequential extraction.

Separate incubations with sterilized site water from BG-0004A were done using washed sand to determine the effects of prolonged exposure to ethanol in the absence of living biota. Site water (30 mL) was sterilized in reactor serum bottles by autoclaving at 121 °C and 15 pounds per square inch (lb/in^2) for 30 minutes on 3 successive days. Washed sand (10 g) was considered microbe free following the acid cleaning procedure described in the "I.2.2.1 Preparation of Artificial Substrates" section. Incubations were initiated as above with added chromium-50, followed by pulsed additions of 1 percent w/w ethanol. Individual bottles were harvested at 108 and 248 days and analyzed for chromium-50, Fe, and Mn following sequential extraction.

I.2.2.1. Preparation of Artificial Substrates

Clean Ottawa sand was washed using concentrated HCl to remove traces of metals including Cr, Fe, and Mn. Several kilograms (kg) of sand were treated overnight with 12 N HCl at 60 °C and mild stirring. Sand was rinsed with solutions of successively weaker acid concentrations (6N, followed by 1N, followed by 0.1N) followed by a final rinse with deionized water. This sequence was then repeated twice for a total of three washings. Washed sand was dried at 60 °C for several days and used directly or as a substrate for coated sands.

Hydrous ferric oxide (HFO also known as two-line ferrihydrite; $(Fe^{+3})_2O_3.0.5H_2O$) was prepared according to methods described in Lovley and Phillips (1986) and Schwertmann and Cornell (2000) and was modified by Waychunas and others (1996). A 16.7-g/L solution of ferric chloride hexahydrate ($FeCl_3.6H_2O$) was titrated to a pH of 7 with 6N sodium hydroxide (NaOH) and allowed to settle. The precipitate was centrifuged, washed, and re-suspended in deionized water four times to remove salts. A concentrated HFO suspension was added to 1 kg of acid washed Ottawa sand and allowed to evaporate overnight with gentle stirring. The HFO/sand mixture was manually homogenized (massaged) and completely dried for another 24 hours to create what is referred to as "Fe sand." The dried HFO/sand was washed three times in deionized water to remove unbound HFO and dried a final time.

I.2.2.2. Sequential Extractions

Sequential extractions followed protocols modified from Chao and Sanzolone (1989) and Wenzel and others (2001; see table I.3 for an overview of procedures). Procedures were similar to sequential extraction procedures used in chapter C within this professional paper (chapter C, table C.2). Extractions began by separating aqueous and solid phases. Measurement of pH and initial transfer of the contents of each microcosm to 50 mL centrifuge tubes occurred in an anaerobic chamber. Centrifugation at 8,000 revolutions per minute times the gravitational constant (RPM x G) for 12 minutes was followed by syringe filtration of the aqueous phase using a 0.45 µm nylon filter. Sample pH was adjusted to less than 2 using several drops of nitric acid (HNO_3). Liquid samples were stored at 4 °C in 30 mL opaque Nalgene bottles before measurement. This initial liquid fraction is referred to as the aqueous phase.

Solids recovered after centrifugation were reacted for 4 hours using 30 mL 0.05 molar (M) potassium chloride (KCl) in centrifuge tubes with shaking. All extractions were done at 22 °C. The liquid and solid phases were separated by centrifugation, the liquid phase was filtered, and the pH was adjusted before storage. This extract was operationally defined as the weakly sorbed fraction. Solids were rinsed twice following this process and each subsequent extraction (resuspended in 30 mL of the previous extractant and centrifuged), and the supernatant was discarded.

A second extraction was made of the solid material recovered after the first extraction using 30 mL of 0.05 M ammonium phosphate, $(NH_4)_2PO_4$, reacted for 16 hours with shaking, followed by centrifugation, filtering, and pH adjustment; this fraction is operationally defined as the specifically sorbed fraction. After rinsing, a third extraction of solids was done using 30 mL of 0.2 M ammonium oxalate ($C_2H_8N_2O_4$) with shaking for 4 hours, followed by centrifugation, filtering, and pH adjustment; this was operationally defined as the amorphous fraction. After rinsing, a fourth extraction of solids was done using 30 mL of 4N nitric acid (HNO_3) with shaking for 16 hours; this fraction is operationally defined as the crystalline fraction (or strong acid extractable fraction; chapter C, table C.2).

Table I.3. Overview of sequential extractions.

[µm, micrometer; M, molar; h, hours; Fe, iron; Mn, manganese; N, normal]

Extraction	Target phase or fraction	Means of extraction	Extractant
0	Aqueous	Filter 0.45 µm nylon	None
1	Weakly sorbed	Change of ionic concentration	0.05 M potassium chloride (4 h)
2	Specifically sorbed	Competing sorbing anion	0.05 M ammonium phosphate (16 h)
3	Bound to amorphous Fe-Mn oxides	Dissolution through complexation	0.2 M ammonium oxalate (4 h)
4	Residual primary and secondary minerals (crystalline)	Strong acid digestion	4 N nitric acid (16 h)

[1]Modified from Chao and Sanzolone (1989) and Wenzel and others (2001).

I.2.2.3. Analysis of Extraction Solutions

The Cr, chromium-50, Fe, and Mn contents of sequential extracts were analyzed by inductively coupled plasma-mass spectrometry (ICP-MS) using a Perkin Elmer NexIon 300Q. Standards, mixed within the sample queue, were analyzed each day along with samples. Standards were prepared by serial dilution of commercial atomic absorption standards in 2 percent v/v HNO_3. Extraction 4 (4N HNO_3) was diluted to 10 percent of its original concentration with deionized water before analysis to adjust the matrix to approximately 2 percent v/v HNO_3. All other extracts were analyzed without dilution. Slight variations of the amount of HNO_3 (1.5–2.5 percent) in the matrix had little effect on the measurement of standards or samples. An internal standard of 100 micrograms per liter (µg/L) germanium (Ge) was added to each sample and standard analyzed to correct for variation in ionization efficiency. Total Fe was calculated from measured iron-57 (2.119 percent of the total Fe). Aqueous and sequential extraction data were reported as nanogram per gram (ng/g) of the solid material. Reporting levels for chromium-50 were less than 5 µg/L in solution, corresponding to less than 15 ng/g of solid material (less than 150 ng/g in extraction 4). Standard replication error was plus or minus (±) 5 percent. Duplicate sample analyses (expressed as the sum of all five extracts for each element) agreed within 30 percent in all but 1 timepoint (out of 60 timepoints).

I.2.3. Oxidation Experiment

Batch reactor microcosms were prepared in 50-mL serum bottles for use in oxidation experiments. Initial reduction began with 30 mL unfiltered groundwater and 10 g of the following materials (table I.1) (1) native aquifer material collected at depth upgradient from the IRZ (sites BG-0004 and BG-0005), (2) aquifer material collected at depth within the IRZ and maintained anoxically (site SA-SB-01), (3) cleaned Ottawa sand coated with hydrous Fe(III) Fe oxide (Fe sand), (4) cleaned Ottawa sand coated with Mn(III) and Mn(IV) manganese oxide (Mn sand), and (5) mixtures of Fe- and Mn-coated Ottawa sand prepared at three (w/w) ratios (as Fe/Mn 100, 50, and 25) to bracket the environmental range of element ratios in native Mojave River aquifer materials. Artificial substrates were included as controls for comparison with site materials in microcosm incubations. These characterized materials of known composition and mineralogy were prepared to evaluate the roles that Fe and Mn play in reoxidation of Cr. In situ reactive zone samples (site SA-SB-01) were processed in an anaerobic chamber using N_2-sparged site water to avoid air contact. Additional site information is available in chapter C within this professional paper.

I.2.3.1. Preparation of Artificial Substrates and Incubations

Iron-coated sand (Fe sand) for reduction experiments was prepared as described in section “I.2.2.1 Preparation of Artificial Substrates.” Manganese-coated sand (Mn sand) was prepared after first making a suspension of Mn oxide by overnight bubbling of a cooled solution of manganous sulfate ($MnSO_4.H_2O$) and potassium hydroxide using oxygen (McKenzie, 1971). The precipitate was centrifuged, washed, and re-suspended in deionized water four times to remove salts. This concentrated manganese dioxide (MnO_2) suspension was added to 0.2 kg of acid washed Ottawa sand and allowed to evaporate overnight with gentle stirring. The Mn-sand mixture was manually homogenized (massaged) and completely dried for another 24 hours to create Mn-coated sand (Mn sand). Manganese-coated sand was washed three times in deionized water to remove unbound MnO_2 and dried a final time. Combined Fe sand and Mn sand mixtures were prepared by weight and homogenized in 1-gallon sealable plastic bags. Combined mixtures were prepared to bracket the ratio of Fe:Mn found in native Mojave River aquifer materials and consisted of sand grains separately coated with either Fe or Mn but not both.

All glassware and plasticware was acid washed in 6-normal hydrochloric acid (6N HCl), rinsed six times in deionized water, and air dried before use. Bottles were sealed with butyl rubber stoppers and 1.0 mg/L Cr(VI) (as potassium chromate) was added at the start (equivalent to 3,000 ng Cr(VI)/g of material). All samples received additions of ethanol (1 percent v/v) using sterile technique approximately weekly for 3 months, followed by less frequent (monthly) additions for a year or more. Incubations were maintained at 22 °C in dark, anoxic conditions.

Following reduction for 1.25±0.2 years, reoxidation of microcosms was initiated by piercing the rubber stoppers of microcosms with two 25-guage needles using aseptic technique (flame sterilization). A short (2.2-cm) needle was inserted to act as an exit for the initial flush with 60 mL of sterile air (three times the headspace volume). Sterile air was introduced through 0.2-µm nylon syringe filters using a needle sufficiently long (5 cm) to reach the liquid in each bottle, effectively sparging the liquid phase. After sparging, the longer needle was removed, and the shorter (exit) needle was capped with a 0.2-µm nylon syringe filter, allowing sterile air to exchange with the bottle headspace during the oxidation period. Microcosms were oxidized at 22 °C with gentle reciprocal shaking that was sufficient to overcome diffusion barriers and keep the liquid oxidized but not vigorous enough to suspend microcosm material and thereby increase surface area.

Triplicate bottles were harvested immediately after the microcosms were prepared (0 days) and after various oxidation times (14, 56, 125, 285, 365, and 679 days). The first extractions of solid samples on the first day (0 days of oxidation) were done without added magnesium chloride ($MgCl_2$; see the "Alkaline Extractions" section). On the basis of the data, this omission resulted in erroneously high yields of Cr(VI) from recently precipitated Cr(III); therefore, $MgCl_2$ was added in all subsequent extractions. The presence or absence of $MgCl_2$ had no effect on the aqueous Cr(VI) values at 0 days or any subsequent time. Therefore, an additional single bottle was harvested for solid and aqueous Cr(VI) at 0 days. In total, one solid value and four aqueous values for Cr(VI) were measured at 0 days.

Aqueous and solid phases were separated by centrifugation (8,000 x *G*) for 12 minutes, followed by pH determination and syringe filtration through 0.45-µm filters. Aqueous samples were stored in opaque 30-mL Nalgene bottles at 4 °C for 1–2 days before analysis of Cr(VI). Portions of the solid phase not used for alkaline extractions were frozen (−80 °C) and later subsampled for determination of Fe and Mn oxidation state. Other aliquots of the solid phase were subsequently thawed, air-dried, and ground for additional study.

I.2.3.2. Alkaline Extractions

Extraction of solid-phase Cr(VI) followed the protocol outlined in EPA Method 3060A (U.S. Environmental Protection Agency, 1996). This alkaline digestion displaces free and sorbed Cr(VI) from particle surfaces and interstices and stabilizes the extracted Cr(VI) in solution. Briefly, 2.5- or 5.0-g of separated solids were reacted with 50 mL of digestion solution (0.5-M NaOH with 0.28-M sodium carbonate; Na_2CO_3) in 250-mL borosilicate glass conical flasks for 1 hour in a shaking water bath at greater than 90 °C. Phosphate buffer (0.5 mL of 1.0 M) was added to enhance desorption of Cr(VI), and 850 milligrams (mg) of magnesium chloride hexahydrate ($MgCl_2.6H_2O$) was added to inhibit oxidation of Cr(III). After digestion, samples were cooled slowly and filtered through 0.45-µm filters, the pH was adjusted to 7.5 using 5N HNO_3, and the volume was adjusted to 100 mL with deionized water. Samples were stored in 125-mL opaque Nalgene bottles at 4 °C for 1–2 days before analysis for Cr(VI).

I.2.3.3. Hexavalent Chromium Analysis

Aqueous and extracted samples were analyzed for Cr(VI) by colorimetric spectrophotometry using the DPC method (U.S. Environmental Protection Agency, 1992). Aqueous and extracted (solid) data were reported as ng Cr(VI)/g of material. The detection limit for Cr(VI) was less than 5 µg/L in solution which corresponded to a reporting level of 15 ng/g of material for aqueous samples and 150 ng/g for solid samples. The fraction of added aqueous Cr(VI) recovered as a matrix spike (potassium dichromate) was 0.82±0.08. Recovery of solid Cr(VI) matrix spike (lead chromate; $PbCrO_4$) was 0.97±0.12 and 1.05±0.19 with addition of $MgCl_2$. Values were sufficiently close to 1.0, so corrections were not required.

I.2.4. Preparation of Solid-Phase Samples

Solid-phase samples were handled and stored using procedures intended to preserve reactive surfaces on mineral grains. Similarly, sample preparation before portable (handheld) X-ray fluorescence (pXRF) analyses, microbeam analyses, and loading on instruments was done using procedures intended to preserve sample integrity while maximizing instrument sensitivity.

I.2.4.1. Sample Receipt and Storage

The experimental timepoint microcosms that were used for solid-phase analyses are available in appendix I.1 (appendix table I.1.1). Microcosms from reduction experiments and natural samples assumed to be anoxic (for example, the elevated Cr reduction experiment and all depth intervals of site SA-SB-01) were subsampled in an anaerobic (mixed nitrogen and hydrogen) chamber. A subsample (or the entire amount for some microcosms) was dried in the chamber, and the remainder (if any) was stored frozen (−40±5 °C). Subsequently, and as needed, frozen samples were thawed briefly to subsample for drying. Once dried in the anaerobic chamber, assumed anoxic samples were removed and stored in air at room temperature before additional processing and analyses.

Solid-phase samples from oxidation microcosms were frozen at −80±5 °C for storage. Aliquots of briefly thawed samples were dried (aerobically) for subsequent preparation. Dried material from all experiments (and from selected sites described in chapter C) intended to become polished thin sections were sent to a commercial laboratory (Spectrum Petrographics, Vancouver, Washington) for preparation of professional-grade, standard thickness (30 µm) petrographic sections suitable for optical, Raman, scanning electron microscopy (SEM), and synchrotron X-ray absorption spectroscopy-X-ray fluorescence (XAS-XRF) analyses. Thin section preparation included epoxy embedding (in low trace metal, low-temperature curing epoxy, EPOTEK-301) and sectioning/polishing to the prescribed thickness using quality-control mineral grains embedded at the margins of the sample.

Biofilms and inorganic surface coatings were collected from incubations of selected site materials and artificial substrates after reduction. Biofilms and surface coatings were disaggregated in the anaerobic chamber by vortex mixing for 2 minutes. The suspended fraction was decanted and concentrated via centrifugation of the aqueous phase. Biofilm and surface-coating samples were dried overnight inside the anaerobic chamber, or outside using a critical-point dryer, and later mounted for analysis by SEM-energy dispersive spectroscopy (EDS) at the USGS in Menlo Park, California, or mounted for analysis by XAS analysis at the Stanford Synchrotron Radiation Lightsource (SSRL) in Menlo Park, Calif.

A summary of precursor and timepoint samples from the experiments whose solid-phase fraction was analyzed by multiple techniques are available in appendix I.1 (appendix table I.1.1). Data are available in Miller and others (2020b) and Foster and others (2023).

I.2.4.2. Sample Preparation for Bulk X-Ray Absorption and Portable X-Ray Fluorescence Spectroscopy

Particle-size reduction is a physical transformation of the sample that increases data quality from bulk (multi-particle) X-ray based analyses including pXRF and bulk synchrotron XAS. Particle size was reduced by hand grinding or mechanical grinding (using a McCrone "micronizer" mill). Acetone (preferably) or ethyl alcohol (EtOH, when acetone was not available) was the lubricant used for hand grinding in agate mortar and pestles because of its rapid evaporation and minimal interaction with inorganic components of the samples. Quantitative metrics of final particle-size distribution were not obtained; instead, the criterion of achieving a "flour-like" or "non-gritty" slurry with acetone/EtOH was applied to determine if grinding time was sufficient. This procedure was usually repeated 2–3 times when grinding by hand, adding acetone (or EtOH) to cover the sample, grinding until the lubricant was evaporated (less than 5 minutes), checking the texture, and repeating until the desired texture was obtained. Grinding the coated sands was particularly difficult because of the large size and hardness of the quartz sand grains. Although the hand-ground, coated-sand materials were given at least one additional grind relative to site materials, the quality of data collected indicates that final grain size of ground coated sands was qualitatively larger than for other sample types, and this had deleterious effects on the analyses.

Self-absorption is an artifact observed in bulk X-ray absorption spectra as diminished intensity of spectral features within a sample. Self-absorption is driven by the size of specific particles high in the element of interest: if they are too large then self-absorption is enhanced, independent of the size of other particles. The "critical size" of a particle can be estimated if its density and composition are known, but in natural materials it is difficult to know a priori which phases should be considered. Therefore, the accepted strategy used in this study to minimize self-absorption effects was to (1) hand-grind samples and model mineral specimens and (2) dilute samples intended for Cr, Fe, or Mn spectroscopic analysis so that they contain close to but less than 1 percent of any of those elements (separate dilutions for each element were required in some cases). A pXRF spectrometer was used to determine element concentrations (not shown). Boron nitride (greater than 99.9 percent purity) was used as the diluent because it does not attenuate the energy of X-rays over the range of interest of (approximately) 5,000–8,000 electron volts (eV).

I.2.4.3. Sample Loading for Bulk X-Ray Absorption Spectroscopy

Samples were mounted perpendicular to the X-ray beam, in "spacers" (slots) made of rigid material (aluminum or plastic) into which four or eight rectangular slots were cut. Single-sample holders made of Teflon also were used for some samples. After sealing one side of a slot with X-ray transparent tape (usually Kapton but occasionally Sellotape), the ground, diluted (if required) sample was packed into the slot using a spatula or edge of glass slide, compressing the material occasionally to allow maximum packing. After cleaning away excess material, another piece of tape was applied to the open side, sealing the sample inside tape "windows" on both sides through which the beam could pass and interact with the sample when the two were aligned in the same horizontal plane. The presence of multiple slots on a single spacer means that multiple samples can be loaded, using automated "queue" programs.

After identifying and removing a contamination signal from Cr in steel screws and other beamline components, it was determined that some of the aluminum sample holders also contained Cr. Fortunately, the X-ray absorption spectrum of the contaminant Cr signal, which is elemental Cr(0), is uniquely different than the forms of Cr predicted or found to be present in precursor materials or in materials after reduction or oxidation experiments. The contaminant Cr signal was greatest when coated sands were analyzed and the increased particle-induced X-ray scattering from the ground sand samples (due to slightly larger particle size) likely excited more of the contaminant Cr atoms in the holder than other samples loaded in the same spacer. Plastic holders were a possible workaround, and by the end of the study it had been determined that the best way to ensure the absence of the "contaminant" Cr signal was to collect data from samples loaded into smooth-surfaced plastic holders, such as Teflon or polycarbonate, using a glass slide for packing instead of a metal spatula.

I.2.4.4. Sample Preparation for Microbeam Analyses

Petrographic thin sections were primarily used for synchrotron microbeam XAS-XRF, micro-Raman (μRaman) spectroscopy, and SEM-EDS, because identical "regions of interest" could be analyzed by each of the techniques with this type of preparation. Polished, 30-μm-thick sections were prepared at a contract laboratory from billets of unground, dried material immobilized in high-purity epoxy. Some samples and model compounds were analyzed by microbeam methods without preparation simply by sprinkling or smearing grains on conductive carbon tape. This preparation method was used primarily for model compounds in which all particles were compositionally homogeneous, but it also was used for samples with minimal material volume, such as the fine fractions of the elevated Cr reduction experiment (appendix table I.1.1). Model compounds, representing unique Cr, Mn, and Fe species, were prepared as one sample for validation of techniques such as synchrotron micro-XRF (μXRF) redox mapping by first encapsulating each compound separately in tape, then mounting thin strips of tape-encapsulated compounds together on a single 35-mm slide holder. Additional layers of tape were applied to minimize particle leakage and cross-contamination.

All samples intended for SEM-EDS were coated with either carbon (C) or gold (Au) by vacuum deposition using methods standard to the instrument in use (two C coaters and one Au coater). Samples were placed in a bell jar and vacuum applied (to a pressure value less than or equal to 4 x 10^5 Torr). Next, atoms of the coating material (C or Au) were released via an electrochemical method (sputter coating or thermal evaporation) to coat the non-conductive samples. The coating thickness achieved using the electrochemical method was not quantified on any of the instruments, but the scientist in charge of the SEM (who coated most of the samples) provided an expert estimate about the C and Au coatings during each experimental run (see section "I.2.5.4 Collecting and Analyzing Scanning Electron Microscopy-Energy Dispersive Spectrometry Maps and Point Spectra" for additional details). The deposited C coating on petrographic thin sections did not interfere with synchrotron micro-X-ray absorption spectroscopy (μXAS)/XRF at energies greater than 5,000 eV (the conditions for Cr, Mn, and Fe determinations).

I.2.4.5. Sample Loading for Microbeam Analyses

All samples were mounted perpendicular to the propagating direction of the microanalytical beams to fixed sections on horizontal holders for μRaman and SEM-EDS, and to fixed sections on vertical holders for synchrotron XAS-XRF. Petrographic sections were easy to immobilize; for grains on tape, vertical immobilization was accomplished by sandwiching grains between two pieces of tape, then affixing this assembly to an empty 35-mm slide holder so that the sandwiched grains were suspended in the open slot of the holder. For X-ray energies greater than 5,000 eV used in this study, the tape was effectively transparent.

I.2.4.6. Elevated Chromium Reduction Experiment

The low amounts of Cr (less than 10 milligrams per kilogram, mg/kg, not presented here) in the "Reduction," "Sterile washed sand," and "Oxidation" experiments (table I.1) prohibited collection of "clean" bulk XAS spectra. (in other words, minus the contaminating Cr signal described in section "I.2.4.3 Sample Loading for Bulk X-Ray Absorption Spectroscopy"). Therefore, a brief (8-month) third reduction experiment was conducted (see "Elevated Cr reduction" in table I.1) using 10 times greater mass of added Cr(VI)/g of material. Microcosms included material from BG-0004, BG-0005, washed sand, and Fe/Mn 50. The amounts of liquids and solids were modified to keep the initial aqueous concentration of Cr(VI) around 1 mg/L. All other conditions were identical to the reduction experiment and first stage of the oxidation experiment (pulsed additions of 1 percent ethanol with shaking). Analysis of Cr(VI) after 5 months of reduction indicated complete removal from the aqueous phase by that time.

Microcosms were harvested after 5- and 8-months of incubation, and the solids were size-fractionated after physically abrading any coatings (including biofilms) from the bulk of the clastic grains (quartz sand and feldspars). Abrasion was achieved in an anaerobic chamber by vortex mixing of sealed serum bottles for 2 minutes, removing stoppers, and successively pipetting 1.5 mL of liquid and suspended flocculants into microcentrifuge tubes and centrifuging (3,000 x G for 1 minute; where G is the gravitational constant having a value of $6.674 \times 10^{-11} m^3 \bullet kg^{-1} \bullet s^{-2}$) until all liquid was processed. Samples were dried in the anaerobic chamber and were either mounted directly on double-stick carbon tape, attached to aluminum stubs, and then Au coated for SEM-EDS analysis or ground in acetone using a mortar and pestle and transferred to Teflon sample holders for bulk XAS analysis.

I.2.5. Analysis of Solid-Phase Samples

Total organic carbon in microcosm materials before and after the reduction experiment were measured on air-dried samples of aquifer material using a Carlo Erba NA 1500 elemental analyzer connected to an IsoPrime mass spectrometer. Inorganic carbon (carbonate and bicarbonate) was first removed by fuming the samples overnight in a desiccator containing concentrated HCl. Samples were analyzed along with working standards that were calibrated against international standards. Standards were run in size series at the beginning of each run, after each group of 10 samples, and at the end of the run. These working standards served as quality assurance and quality control (QA/QC). The results of total organic carbon analysis before and after reduction with added ethanol are provided in table I.4.

Five additional independent techniques were used to characterize the solid phase of selected microcosms prepared from materials inside and outside the IRZ. Data from these techniques were used to evaluate changes to materials within microcosms that occurred during the reduction, oxidation, and elevated Cr reduction experiments. The pXRF at the USGS in Menlo Park, Calif., was used to determine the chemical composition of bulk and size-fractionated materials that were not analyzed by pXRF at the USGS facility in San Diego, Calif. (Groover, 2016). Optical microscopy was used to characterize changes in thickness of "coatings" on quartz sand grains of artificial substrates and to characterize the density of Fe- and Mn-rich particles associated with the coatings (when present) or exterior of sand grains (when absent). The μRaman spectroscopy technique was used to collect information on composition and structure of phases at the grain to sub-grain scale that complemented the information gained from other solid-phase analytical techniques. The SEM-EDS technique, integrated with chemical and topological imaging capabilities, was used for semiquantitative chemical mapping to derive sub-μm-scale information on the distribution of solid phases of characteristic composition. Finally, synchrotron-based XAS was used to determine the solid-phase speciation of S, Cr, Mn, and Fe to track the progress of geomicrobiological processes occurring during the reduction and oxidation experiments. The XAS and μXAS techniques provided in situ (without pre-treatment) information on S, Cr, Mn, and Fe speciation (valence and molecular-scale coordination) that was used to indicate with which solid phase(s) each element was associated.

Table I.4. Amount of organic carbon in aquifer materials before and after reduction with added ethanol.

[Data available in Foster and others (2023).
Abbreviation: N.D., not determined]

Site	Precursor organic carbon (percent by weight)	Post-reduction organic carbon (percent by weight)
SA-RW-34	[1]0.05	N.D.
BG-0004	0.05	6.72
BG-0005	0.20	6.63
SA-SB-01	[1]0.04	6.84

[1]Precursor SA-RW-34 and SA-SB-01 measured in 2015. All others measured in 2021.

I.2.5.1. Collecting Portable X-Ray Fluorescence Data

Bulk elemental composition (particularly of Cr, Mn, and Fe) of selected samples were determined using pXRF data collected using a portable Thermo Niton XL3t GOLD+ spectrometer in the USGS Environmental Geochemistry and Geomicrobiology Laboratory, in Menlo Park, Calif. Dried samples prepared by a variety of methods were loaded into plastic cups, with 6-μm polypropylene film windows, for analysis. In situations where the amount of sample was insufficient, the sample was placed directly on the 6-μm polypropylene film and arranged to cover the analysis window. Use of an analysis chamber designed for pXRF ensured a uniform sample-to-detector distance regardless of the amount of sample, but it did not remove potential analytical artifacts arising from insufficiently thick samples.

The pXRF data presented in table I.5 were collected in the instrument soils calibration mode, which uses Compton normalization performed by the instrument software based on manufacturer calibration parameters determined. A 60-second count time per filter was used for the 3 filters in soils mode (180 seconds total analysis time per sample). These parameters are consistent with published protocols for pXRF analysis (U.S. Environmental Protection Agency, 2007). A blank sample (99.999-percent reagent-grade silica) and a certified standard reference material were analyzed before, during, and at the end of the analytical run to ensure that values obtained were within ± 20 percent of certified values and that contamination during sample handling and measurement did not occur. With such a wide acceptance criterion, the results were designated as "qualitative."

Table I.5. Results of qualitative (± 20 percent) portable X-ray fluorescence (pXRF) analyses (in milligrams per kilogram) of selected precursor and elevated chromium reduction timepoint samples.

[Three sigma analytical error is given in parentheses. Data available in Foster and others (2023). **Abbreviations**: Cr, chromium; Mn, manganese; Fe, iron; precursor, material before incubation; <, less than; mm, millimeter; micronized, high-speed mechanical agitation to reduce average particle size to 10 micrometers or less; LOD, limit of detection; ground, ground to a fine powder with a mortar and pestle; HiCr Red, elevated chromium reduction; fine, vortex liberated fine material]

Experiment	Sample	Notes	Cr	Mn	Fe
Precursor	BG-0004	Sieve < 0.5 mm, micronized	12 (7)	79 (36)	4,475 (98)
Precursor	BG-0005	Sieve < 0.5 mm, micronized	<LOD[1]	<LOD	3,792 (91)
Precursor	2SA-SB-01	Sieve < 0.5 mm, micronized	12 (8)	104 (38)	6,221 (117)
Precursor	Washed sand	Ground	27 (6)	<LOD	216 (37)
Precursor	Mn sand	Ground	99 (6)	3,898 (195)	572 (99)
Precursor	Fe sand	Ground	<LOD	<LOD	381 (35)
HiCr Red	BG-0004 8 month-1	Fine fraction, in Teflon holder	123 (12)	<LOD	7,124 (108)
HiCr Red	BG-0004 8 month-2	Bulk sample, ground	34 (8)	133 (47)	14,699 (207)
HiCr Red	BG-0005 8 month-1	Fine fraction, in Teflon holder	139 (14)	204 (41)	18,548 (189)
HiCr Red	BG-0005 8 month-2	Bulk sample, ground	50 (7)	113 (51)	7,922 (172)
HiCr Red	Washed sand 8 month	Bulk sample, ground	39 (6)	<LOD	76 (32)

[1]LOD values for Cr, Mn, and Fe reported by instrument software were approximately 8, 51, and 36, respectively.

[2]Median value of four subsamples, each prepared separately and analyzed in triplicate.

I.2.5.2. Collecting and Analyzing Optical Microscopy Data

To semi-quantitatively assess physical differences between samples and timepoints during the oxidation portion of the experiment, sample grains were measured from optical images of prepared thin sections. Images were collected using a Canon EOS Rebel T3i mounted with a LMScope VTC4X2 mount on a Wild Photomakroskop M400 with a rotating stage with a slide translation assembly. The microscope was set to 32x magnification, and the eyepieces were set to a magnification of 10x, for a total of 320x magnification. Illumination was set to 8, and a polarizing plate was partially inserted to provide a shadow view that emphasized grain coatings. The remote shooting feature of the EOS Utility software was used to preview and collect images, which were saved in the camera's native highest-quality format (*.RAW) and then exported as tagged image file format (TIFF) images using the camera manufacturer's software (Canon Digital Photo Professional). At least 25 unique grains were photographed for each individual thin section.

The software "ImageJ/FIJI" was used to measure the diameter of grains vertically and horizontally on the digital images, approximately in the middle; these measurements included any potential coatings on the grain. Additionally, measurements of coatings were collected at the four cardinal directions on each imaged grain, at approximately the same points as the diameter measurements were taken. In places where the presence of a coating was unclear or the analyst was unable to distinguish between the coating and grain, measurements were not collected. Measurements and scale were taken in millimeter units and based on the calibration of an image of Pattern G's 0.1-mm-wide squares on a PS20 Universal Calibration Slide taken during the same conditions as grain images. The calibration of 2012.292 pixels per mm was noted and used for every measurement session. Error was estimated by measuring the same 0.1-mm-wide square from the calibration slide 10 times, after applying the specified calibration, and then calculating the standard deviation.

I.2.5.3. Collecting and Analyzing MicroRaman Spectra

Raman spectra were collected with micrometer scale laser beams focused through microscope objectives (for example, "microRaman" or "μRaman") during ambient conditions using a Thermo DXR μRaman spectrometer equipped with 455-, 532-, and 780-nm lasers, pin and slit collection aperture choices (25 and 50 μm), 10x, 20x, 50x, and 100x objectives, and a variety of grating/filter combinations that enable data collection from 50 to 6,000 cm^{-1} with spectral resolution decreasing stepwise (± 2, ± 5, and ± 10 cm^{-1} for low-range, standard-range, and extended-range gratings, respectively). Spectra were collected using 100x or 50x objectives, which provide a laser spot size of 1 and 2 μm, respectively, using the 532-nm laser. Spectra were collected from a variety of sample types, including polished thin sections, pressed pellets, and loose powders (bulk or size-fractionated) laid or smeared on uncoated or aluminum-coated glass slides.

Quality assurance and quality control for μRaman data collection was performed each day before instrument use and included alignment of the laser, spectrometer, and optical system (using a light-emitting diode [LED] light); wavelength correction (polystyrene target); and intensity correction (neon lamp). The measured position of the 1,001.4±0.5 cm^{-1} peak of a separate polystyrene film card standard was used as an internal QC check, requiring that the measured position be within the stated resolution of the grating used. The count time of spectral collections and the number of spectra averaged to produce a single spectrum varied widely with collection conditions and sample type.

Raman spectra were used to identify minerals and solid-phase materials not strictly qualified as minerals because they lacked long range order. Spectra were background-subtracted using a sixth-order polynomial with 50 iterations (subtraction was generally over the entire range; occasionally, the spectrum might have been clipped on the high or low end). A commercialized version of the RRUFF database (Lafuente and others, 2015) of more than 3,000 mineral Raman spectra was used in an automated, pattern-matching query feature in Omnic v9.2 software (Thermo Scientific, Waltham, Massachusetts) to rank and display the highest-quality matches in the database to the unknown spectrum. Although sensitive to differences in molecular structure, atomic charge, and ionic radii, Raman is not an inherently trace-sensitive technique and could not be used in this default mode to identify Cr-bearing phases or to identify hexavalent Cr in phases at the micrometer scale. Optical images for correlating with Raman spectra acquisition locations were collected from samples using the digital camera system on the Thermo DXR μRaman spectrometer; Thermo Atlas v 9.1.2 software was used to control the Prior high-precision (±0.1 micrometer) X-Y stage and to obtain images with calibrated x, y dimensions.

I.2.5.4. Collecting and Analyzing Scanning Electron Microscopy-Energy Dispersive Spectrometry Maps and Point Spectra

A TeScan VEGA-3 SEM with a thermionic emitter and Oxford X-Max Silicon Drift Detector (50 mm) EDS was used to collect secondary electron (SE) and backscattered electron (BSE) images as well as semiquantitative compositional data. Secondary electron images highlight topography, whereas BSE images provide qualitative chemical composition; brighter grains in the gray-scale images indicate higher average atomic number (Z). Details of the analysis conditions for each SEM data-collection session are summarized in Foster and others (2023). Compositional data were collected as element maps and as grain (area) or point analyses. The elements Cr, Fe, and Mn. Carbon (C) and Au were required to be quantified (even if those quantifications were below detection) and were deconvolved when analyzing sections coated with C or Au; tungsten was ignored because of interference with other elements' X-ray emission lines. Elements of interest were not deconvolved, window artifact corrections were enabled, and factory standards were used for semiquantitative compositional analyses. Semiquantitative individual and combined element maps (particularly of Fe, Mn, and Cr) and morphological features were used to identify sites of interest for point grain (area) or line spectral data collection. Point spectra have the advantage of greater spatial resolution and better quantification statistics than spectra generated from maps. Compositions are presented as normalized data, in atom percent, with oxygen calculated by difference. Compositions are reported at the three-sigma (99.7 percent) confidence interval.

I.2.5.5. Collecting and Analyzing Bulk and Microbeam X-Ray Absorption Spectrometry Data

X-ray absorption spectroscopy data were collected at SSRL in Menlo Park, Calif. The photoelectron storage ring was operated at 3 gigaelectron-volts (GeV) and 500 milliamperes (mA) in top-off mode (ring current maintained by reinjection every 10 min) during all data-collection periods (calendar years 2017–19). Bulk XAS data was collected on beamlines 4-3 and 11-2 and microbeam data on beamlines 10-2 and 2-3 (Foster and others, 2023). Information about the optical setup of each of these lines is available at the SSRL website (link easily obtained via internet search). Silicon (Si) double-crystal monochromators and harmonic rejection mirrors were used on all beamlines. Monochromators have inherent imperfections that lead to sharp deviations at specific, invariant energies, called glitches. There was no available monochromator that was glitch-free over the 3,000-eV interval encompassing the Cr, Mn, and Fe energy regions of interest (5,000–8,000 eV). Monochromators that were glitch-free over the Cr energy region (5,000–6000 eV) were selected whenever possible to optimize analysis of this element, and the vertical gap of the monochromator hutch slits was set at 1 mm to optimize resolution in the Cr pre-edge region.

Initial energy calibration of the monochromator was accomplished by (1) collecting a spectrum of reference material, (2) measuring its edge position (by convention, taken as the first inflection point, as determined by the first derivative), and (3) shifting the absolute energy scale of the monochromator so that the measured edge position was equivalent to the agreed-upon value. Thin (about 5 μm) foils of the native forms of Cr, Mn, and Fe were used for energy calibration, with standard values of 5,989.0, 6,539.0, and 7,112.0 used for energy calibration at each edge (Thompson and Vaughan, 2001).

Highly sensitive solid-state detectors with arrays of 100 (BL 11-2) or 30 (BL 4-3) sensing elements (made of Ge) were used to measure the characteristic X-rays arising from Cr and Mn at low concentration (less than 500 mg/kg). Less sensitive "drift" detectors made of one or more Si elements were used to analyze Fe and Mn (at concentrations greater than 500 mg/kg) in bulk mode (a one-element Si drift detector was used for microbeam data collection). The lower-sensitivity passivated implanted planar silicon (PIPS) detector also was used on BL 4-3 to collect data from concentrated Fe samples. Silver "soller" slits and Z-1 elemental filters also were used to remove background radiation when using these detectors (for bulk XAS data collection only). The solid-state Ge detectors are particularly sensitive to deadtime, a situation in which the rate of counts into the detector exceeds its ability to accurately count them, leading to a non-linear relation between total incoming and total outgoing counts (both in counts per second). Making deadtime corrections to the solid-state Ge detectors were avoided by keeping the amount of total outgoing counts below the value at which the plot starts to "flatten out" and become non-linear. This was primarily accomplished by moving the detector closer to or farther from the sample.

X-ray absorption fine structure (XAFS) data collection was in step-scan mode, with 10 eV steps to define the shape of the background, 0.1 eV steps in the pre-edge region, 0.2 eV steps in the main X-ray absorption near edge structure (XANES) region, and approximately 3 eV steps in the extended XANES region for Cr, Mn, and Fe. Count time at each step was 1–2 seconds. Samples intended for extended X-ray absorption fine structure (EXAFS) analysis had count times in the extended XANES region starting at 3 seconds and increasing to 15 seconds to the endpoint as defined by a cubic function. This is standard procedure and is meant to lower the random noise, which is enhanced by cubic weighting applied to the EXAFS region for analysis (Koningsberger and Prins, 1988).

I.2.5.6. Processing Bulk and Microbeam X-Ray Absorption Spectroscopy Data

Calibration of bulk and microbeam Cr, Mn, and Fe spectra was accomplished by shifting the sample spectrum by the same amount required to align the measured edge position of the respective calibration foil with its known value (Thompson and Vaughan, 2001). However, the frequency of calibration as well as the time between collection of calibration foil spectra differed by beamline/analysis date (bulk spectra). Calibration checks for micro-XANES (μXANES) spectra were performed at the beginning and end of beamtime only. Bulk Fe XAS spectra could usually be calibrated using the Fe foil spectrum recorded along with the sample (as the log of the ratio of the second N_2-filled ion chamber and the third argon gas-filled ion chamber), but this was not done for Mn or Cr because of the attenuation of the incident X-ray beam by air.

For Mn and Cr, calibration foil spectra were collected before and after collecting spectra of multiple samples using automation queues (calibration foil placed in the position of the sample cassette). If the measured calibration edges did not vary by more than 0.3 eV, they were considered identical within error. If they varied by more than 0.3 eV, the uncorrected edge positions were examined to determine if the difference was due to slow drift or to a sudden change in beam orbit or energy, which also could produce a sudden change in calibration.

Data processing was performed in SixPack 1.5.6 software, (Webb, 2005) according to standard procedures described elsewhere (Hansel and others, 2003b; Foster and Kim, 2014). The pre-edge (background) energy of the calibrated spectrum was fit with a linear or Gaussian function, which was then subtracted from the spectrum. Next, normalization to a single point 50–100 eV beyond the edge was performed to remove the concentration dependence of the intensity (y-axis) of the XAS spectrum, allowing direct qualitative and quantitative comparison of samples with different concentrations of Cr, Mn, or Fe. Samples were normalized to a single point located 50–100 eV beyond the edge where absorbance approaches invariance for all species.

At this stage, the complete spectrum is called the "extended XANES." The (XANES) spectra are produced from the extended XANES by simply removing the higher energy region. The length (in energy) of a XANES spectrum beyond the absorption edge varies with the user's need. In general, XANES spectra extend 50–200 eV beyond the absorption edge, depending on factors such as the type of analysis to be conducted and the quality of the data.

Extended XANES are converted to EXAFS, by fitting the spectrum with a stiff spline function (5–9 knots) starting at the energy position attributed to the promotion of a core-level electron to the continuum band (known as the "Fermi level" or "Eo" in some EXAFS software; one value was used for each element). The spline function approximates the spectrum of the element in the absence of neighboring atoms; this was subtracted from the data to leave the spectrum of the element in the presence of neighboring atoms. The EXAFS spectrum was generated by clipping data below the Fermi level energy and converting from energy (in eV) to momentum, represented in wave vector state photoelectron wave vector, k, preferred units of inverse angstroms) using Planck's constant (h). Extended X-ray absorption fine structure spectra are typically weighted by k^3.

The EXAFS spectrum is a sum of sinusoidal waves, each with a frequency and amplitude unique to the absorbing atom (Cr, Mn, or Fe) and its backscattering neighbor (O, Cr, Mn, Fe, Si, or any other element within about 7 angstroms of the absorber). Taking a Fourier transform of the data separates the sinusoidal waves, producing a pseudo-radial distribution function (RDF) with units of angstroms (Å), with the absorbing atom at 0 Å. A window function is used for the Fourier transform to reduce "ringing" effects in the resulting RDF. The pseudo-RDF is not corrected for phase shift effects, with the result that the plotted distances are about 0.5 Å less than true distances.

I.2.5.7. Analysis of Bulk and Microbeam X-Ray Absorption Near-Edge and Extended X-Ray Absorption Fine Structure Spectra

After processing as described above, the bulk and microbeam XANES spectra analyzed in this study were equivalent in effective resolution (a combination of crystal monochromator Bragg reflection, distance from monochromator collimating slits to the collimating slits inside the sample hutch, and the data-collection parameter "step size") and were qualitatively and quantitatively compared. Bulk and microbeam EXAFS spectra also were equivalent in effective resolution but for a different reason: EXAFS features are broad relative to XANES features and are not affected by the resolution-affecting variables outlined above.

The primary assumption in qualitative and quantitative analyses of XANES and EXAFS spectra is that the overall line shape of the unknown spectrum is representative of one or more particular "solid-phase species." The term "solid-phase species" encompasses the oxidation state of the element, its mineral/phase residence, and its assumed geochemical mode of association. The assumed geochemical mode of association is critically important because it discriminates among adsorbed, co-precipitated, and substituting (in crystalline phases) modes of mineral/phase association. Identifying the primary mode of association helps to understand the likelihood of changes that could occur under dynamic geochemical conditions. The small spot size used in collection of μXANES increases the likelihood of analyzing a single solid-phase species, but when analyzing bulk XANES of heterogeneous materials such as aquifer materials used in these experiments, this assumption does not hold.

Methods of qualitative comparison presented in this professional paper include stack and overlay plots of XANES and EXAFS spectra in which spectral similarity and difference are visualized without fitting. Smoothed first or second derivatives of XANES spectra are commonly used in qualitative comparison instead of raw spectra, because they provide greater sensitivity to subtle changes in peak positions and line shape (Koningsberger and Prins, 1988). The positive second derivative positions are coincident with positive peak positions in the XANES spectrum (and therefore easier to intuitively understand in a visual analysis), whereas the first derivative maxima reveal the inflection points in the spectrum—these positions are not equivalent to peak heights. Nevertheless, first derivative spectra are useful for qualitative (tabulated) and quantitative analysis for two reasons: (1) peaks vary in width, therefore defining the maximum is problematic and (2) all derivative spectra amplify noise, which increases exponentially with derivative order; as a result, second derivative spectra require a greater amount of smoothing to produce a spectrum that can be analyzed. Smoothing removes information from the spectrum, and therefore was minimized when possible.

I.3. Results

Preliminary experimental results and results from the longer-term reduction and oxidation experiments are presented. Time-series results for the reduction experiment by extraction type and mass-balance results for the reduction experiment by sample type for selected elements are presented separately. Also presented are the reduction of site material and artificial substrates and the changes of those materials through time.

I.3.1. Preliminary Experiment

Oxygen removal began with the addition of ethanol, and oxygen was completely removed within 77 days during the 146-day incubation of preliminary microcosms, commensurate with reduction of SO_4^{-2} and metals (fig. I.2). Ethanol additions did not remove oxygen in control microcosms (deionized water or gamma-irradiated site water containing no viable microbes), demonstrating that oxygen removal was controlled biologically (fig. I.2*A*).

In seven of nine microcosms containing buffers and one microcosm without a buffer, pH ranged between 7.3 and 7.6 during the 146-day incubation (fig. I.2*B*). However, pH decreased markedly after 56 days in bottles with 10 mM HEPES and 10 mM EPPS buffers. Hexavalent chromium was completely removed from the solution within 7 days in microcosms buffered with HEPES (fig. I.2*C*), and within 56 days in all other microcosms, including one with no buffer. Hexavalent chromium depletion occurred before oxygen was completely removed from the bottles. Reduction of Cr(VI) in the presence of oxygen was demonstrated in environmental settings in Hinkley Valley upgradient from the Hinkley compressor station (chapter F, fig. F.27). Sulfate reduction occurred in all microcosms containing buffers but was absent in the microcosm without buffers (fig. I.2*D*). Aqueous Fe (fig. I.2*E*) only increased in the two microcosms where pH had decreased significantly (10 mM HEPES and EPPS buffers). By contrast, dissolved Mn decreased slightly in all microcosms (fig. I.2*F*) during the first 5 days then increased. The largest increases in dissolved Mn also occurred in microcosms containing 10 mM HEPES and EPPS, following decreased pH.

Results of all chemical analyses of samples from the preliminary reduction, elevated Cr reduction, and oxidation experiments are available in Miller and others (2020b). Based on the results of the preliminary experiment, buffers were not used to control pH in the later reduction experiments because their use resulted in low redox conditions outside the environmental range found within the IRZ.

I.3.2. Reduction Experiment Time Series (by Extraction)

During the 2-year reduction experiment, Cr sequestration was observed in all materials tested (BG-0004, BG-0005, washed sand, and Fe sand). Sequestration is presented graphically on figure I.3 as a time series of the amount of chromium-50 extracted from each of the five operationally defined fractions (table I.3). As part of the experimental design, 1,000 mg/L aqueous Cr(VI), equivalent to 1,600 ng of chromium-50 per g of material, was added to each microcosm; the added Cr(VI) included chromium-50 used as a tracer. Figure I.3*A* shows the rapid removal of the chromium-50 tracer from the aqueous phase during incubations with BG-0004 and BG-0005 materials. Removal of chromium-50 was slower in incubations with washed sand and Fe-coated sand but was nonetheless nearly complete by 168 days.

A small amount of chromium-50 was recovered initially in the weakly sorbed fraction extracted from all samples (fig. I.3*B*), which indicated rapid and finite sorption processes (ion exchange) on particle surfaces. As with the aqueous phase, the amount of chromium-50 recovered during the extraction of weakly sorbed fractions decreased rapidly with time in the site materials and less rapidly in artificial substrates. By 720 days, no chromium-50 remained associated with this fraction in any sample.

No chromium-50 was recovered initially in the specifically sorbed fraction of any sample (fig. I.3*C*), indicating that some time was required for specifically sorbed fractions to form. However, after 41 days, some chromium-50 was recovered in the specifically sorbed fraction of all samples. Low, but consistently higher (2x) values were measured for washed sand than for the other sample types. Overall, there was little change through time in the amount of chromium-50 associated with this fraction.

No chromium-50 was recovered initially in the amorphous fraction extractions (fig. I.3*D*), indicating that this fraction also did not form immediately. Pronounced increases in the amount of chromium-50 associated with this fraction were observed for site materials extracted after 41 and 83 days. A lesser increase was observed for Fe sand, whereas almost no chromium-50 was associated with this fraction in washed sand.

Nearly all added chromium-50 (1,600 ng/g) resided in the operationally defined crystalline phase of site materials after 350 days of reduction (fig. I.3*E*). This was entirely the case for BG-0004 and somewhat less so for BG-0005. Initial 4N HNO_3 (crystalline) extractions from BG-0004 and BG-0005 materials yielded 300 and 225 ng/g chromium-50, respectively, which is consistent with partitioning of Cr isotopes based on estimates of the total Cr present in native Mojave River aquifer materials as measured by pXRF (Groover and Izbicki, 2019). Initial extractions of artificial substrates did not yield chromium-50. Crystalline-phase extractions of site materials generally yielded twice the chromium-50 as artificial substrates, and the chromium-50 was recovered at higher levels earlier in the incubations. Mineralization patterns were similar among sample types (site materials and artificial substrates) with the exception that BG-0004 (composed of recent Mojave River materials having lower Fe and Mn concentrations) continued to mineralize chromium-50 after 183 days, whereas incorporation of chromium-50 into the crystalline phase of other samples including BG-0005 (composed of older Mojave River materials having higher Fe and Mn concentrations) and the Fe-coated sand control was complete by this time (fig. I.3*E*).

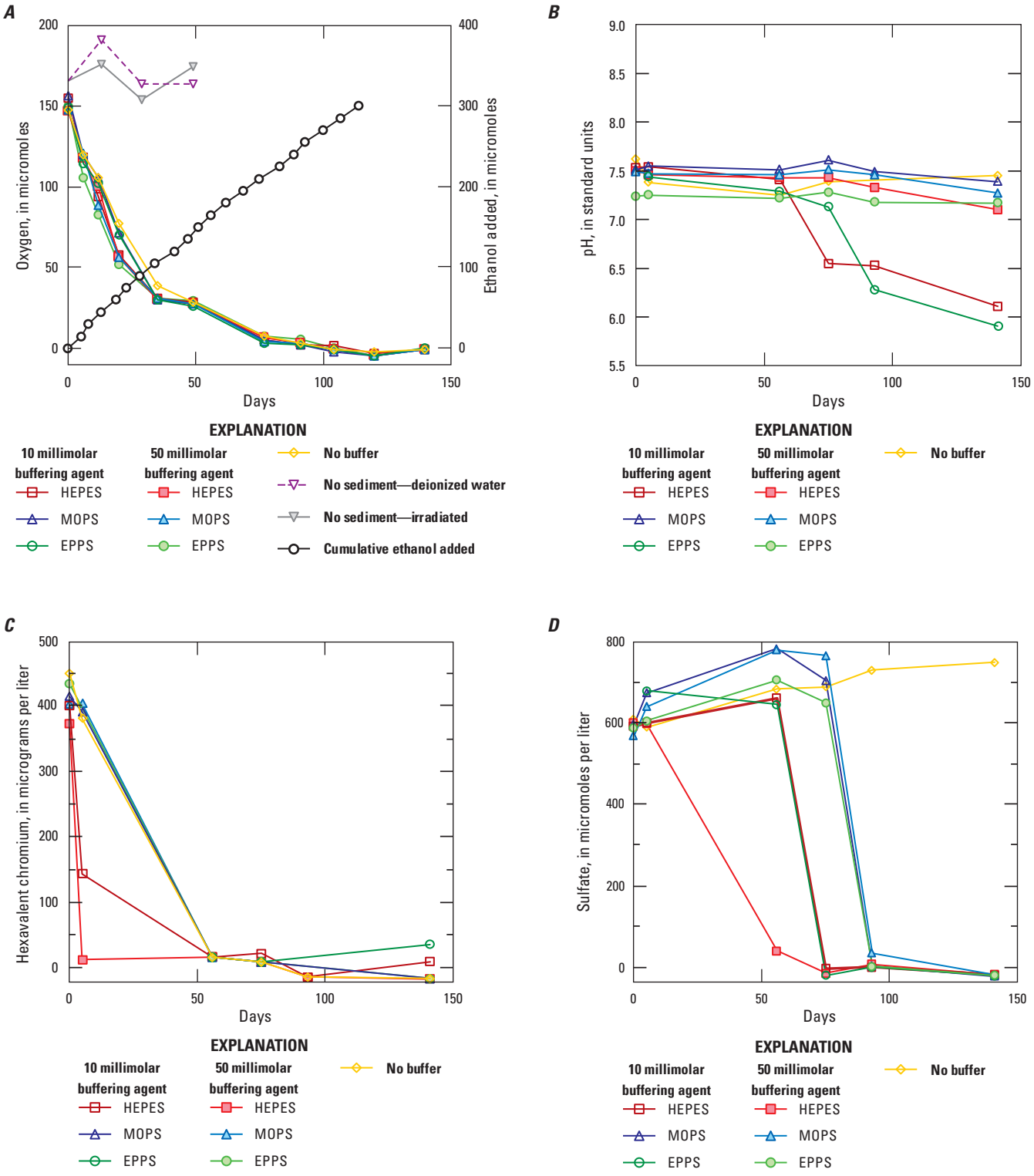

Figure I.2. Time-series results of a preliminary experiment demonstrating *A*, oxygen (O_2) removal with repeated ethanol additions and *B*, corresponding changes to aqueous pH; and concentrations of *C*, hexavalent chromium (Cr); *D*, sulfate (SO_4^{-2}); *E*, iron (Fe); and *F*, manganese (Mn) in buffered and un-buffered microcosms. Buffers included HEPES [4-(2-hydroxyethyl)-1-piperazineethanesulfonic acid]; MOPS [3-(N-morpholino) propanesulfonic acid]; or EPPS [N-(2-Hydroxyethyl)piperazine-NÁ(3-propanesulfonic acid)]. Data are available in Miller and others (2020b).

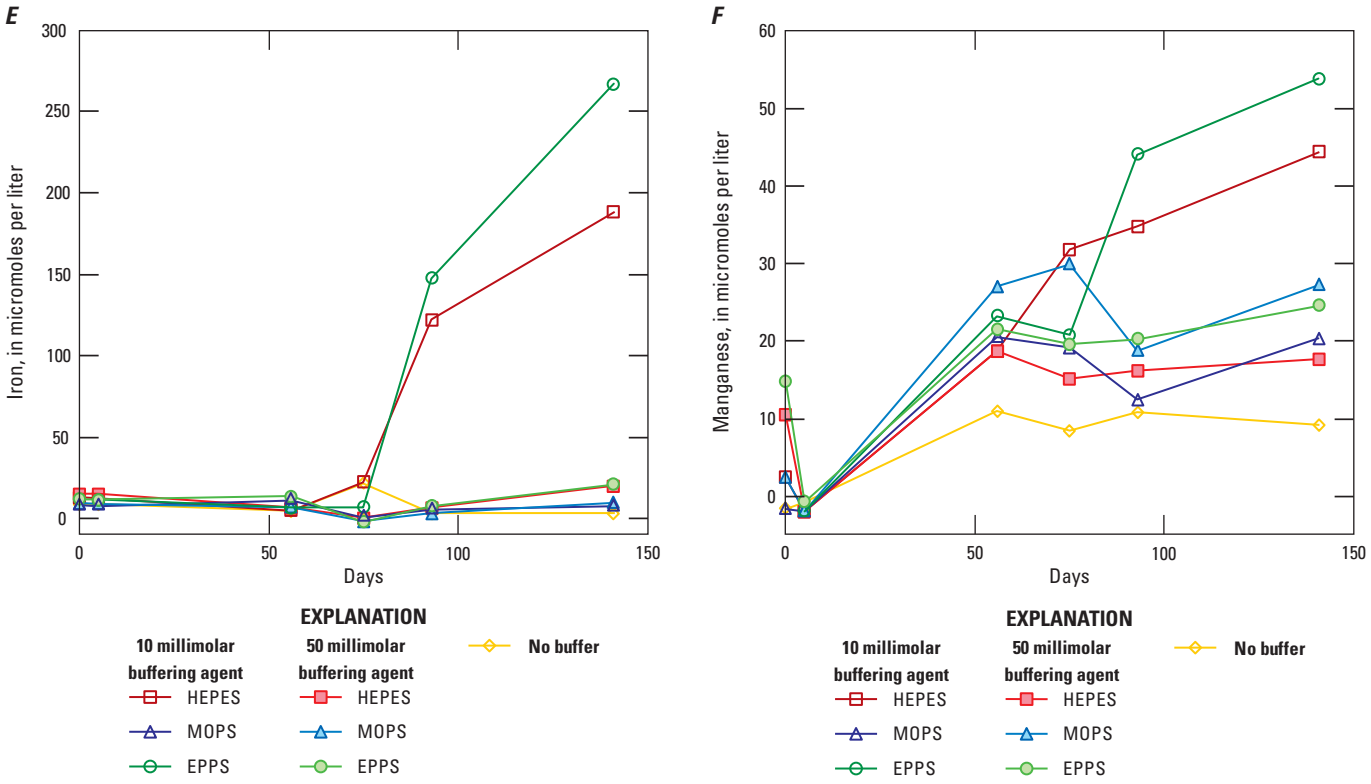

Figure I.2.—Continued

I.3.3. Reduction Experiment Mass Balance (by Sample Type and Element)

The mass of Cr and other elements in site materials and artificial substrates reduced during microcosm experiments is presented. The changes with time, of Cr and other elements on surface sorption sites also are presented.

I.3.3.1. Reduction of Site Materials

Figure I.4 shows the total amounts of chromium-50, Fe, and Mn recovered over time by sequential extractions of site materials. Data from duplicate incubations (when available) are presented side by side in stacked bar graphs. Sites BG-0004 and BG-0005 totals (figs. I.4*A–C*, I.4*D–F*, respectively) indicated that some of the added chromium-50 was unaccounted for, especially during the period between 41 and 350 days (figs. I.4*A*, *C*). This discrepancy indicates that Cr may be sequestered in a fraction that was not fully recovered by the method of sequential extractions (possibly microbial biomass) and is explained more fully in the "I.4 Discussion" section. Full recovery of the chromium-50 spike (aqueous plus weakly sorbed) at the outset of all incubations and in all fractions after 720 days in BG-0004 indicates that the sampling and analytical protocols were robust. Although rinsing of solids between extractions could result in minor chromium-50 loss this did not seem to be an important issue in this experiment.

Total extractable Fe from the five operationally defined fractions increased over time in incubations with site materials. Total Fe increased by 100 percent in BG-0004 (fig. I.4*B*) and by 50 percent in BG-0005 (fig. I.4*E*) during the 720-day incubations. Aqueous Fe appeared at later stages of reduction of site materials; however, most of the Fe was recovered in the crystalline fraction. More Fe was recovered with time in the crystalline fraction in BG-0004 than in BG-0005. As with chromium-50, crystalline Fe increased until day 720 of reduction in BG-0004 but remained roughly constant in BG-0005.

The total amount of extractable Mn recovered from the five operationally defined fractions (figs. I.4*C*, *F*) increased somewhat with duration of reduction. Environmental increases in manganese concentrations within the IRZ were of regulatory and public health concern (Lahontan Regional Water Quality Control Board, 2011). Manganese was initially present within microcosms mostly in the crystalline phase of sites BG-0004 and BG-0005. At later incubation times, more than half of the Mn was extracted from solid fractions (sorbed, amorphous, and crystalline); however, a large fraction of the Mn was dissolved. Total Mn recovered was three times greater in BG-0005 than in BG-0004.

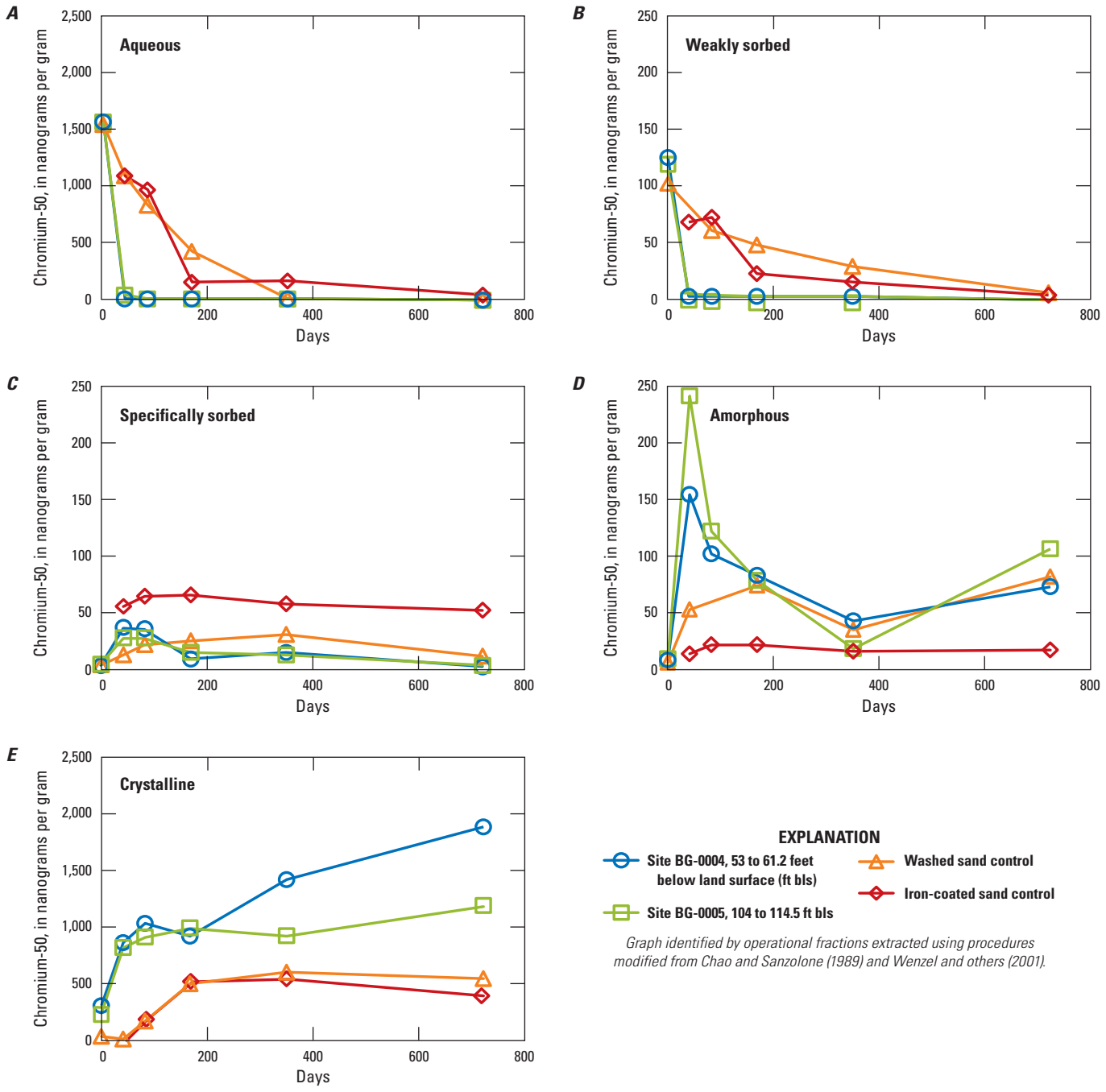

Figure I.3. Time-series of the median (n=2) amount of chromium-50 recovered in each of five operationally defined phases or fractions by sequential extractions of materials during 2 years of reduction: *A*, aqueous; *B*, weakly sorbed; *C*, specifically sorbed; *D*, amorphous; and *E*, crystalline. Note the 10 times higher scale for chromium-50 recovered in the aqueous phase *A* and strong acid extract *E*. Data are available in Miller and others (2020b).

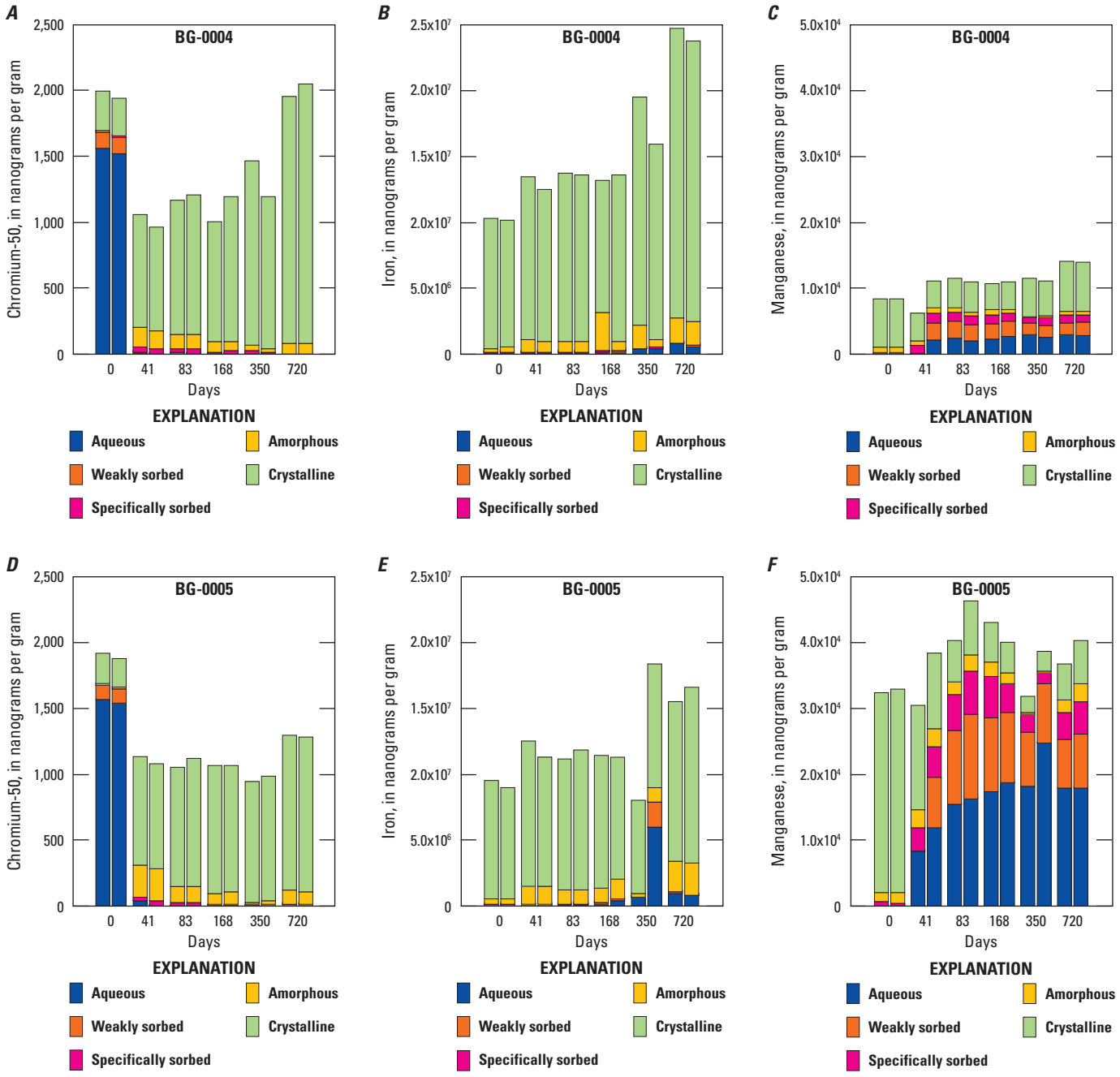

Figure I.4. Cumulative amounts of *A*, chromium-50; *B*, iron (Fe); and *C*, manganese (Mn) obtained from site BG-0004 and cumulative amounts of *D*, chromium-50; *E*, Fe; and *F*, Mn obtained from site BG-0005, during sequential extractions of site materials reduced for various times. Replicate analyses are presented side by side when available for the six incubation periods. The horizontal axis is not scaled. Data are available in Miller and others (2020b).

I.3.3.2. Reduction of Artificial Substrates

Conversion of chromium-50 from aqueous to solid phases occurred more slowly during reduction within microcosms containing artificial substrates (fig. I.5). There was no difference in the rate of chromium-50 removal from the aqueous phases of washed sand and Fe sand, indicating that reduction of Fe played a minor role in adsorption and sequestration of Cr in artificial substrates. A regular decrease was observed in the total amount of chromium-50 recovered through time (figs. I.5*A*, *D*). Half of the chromium-50 initially present in the aqueous phase remained unaccounted for in the washed sand and Fe sand incubations after 720 days.

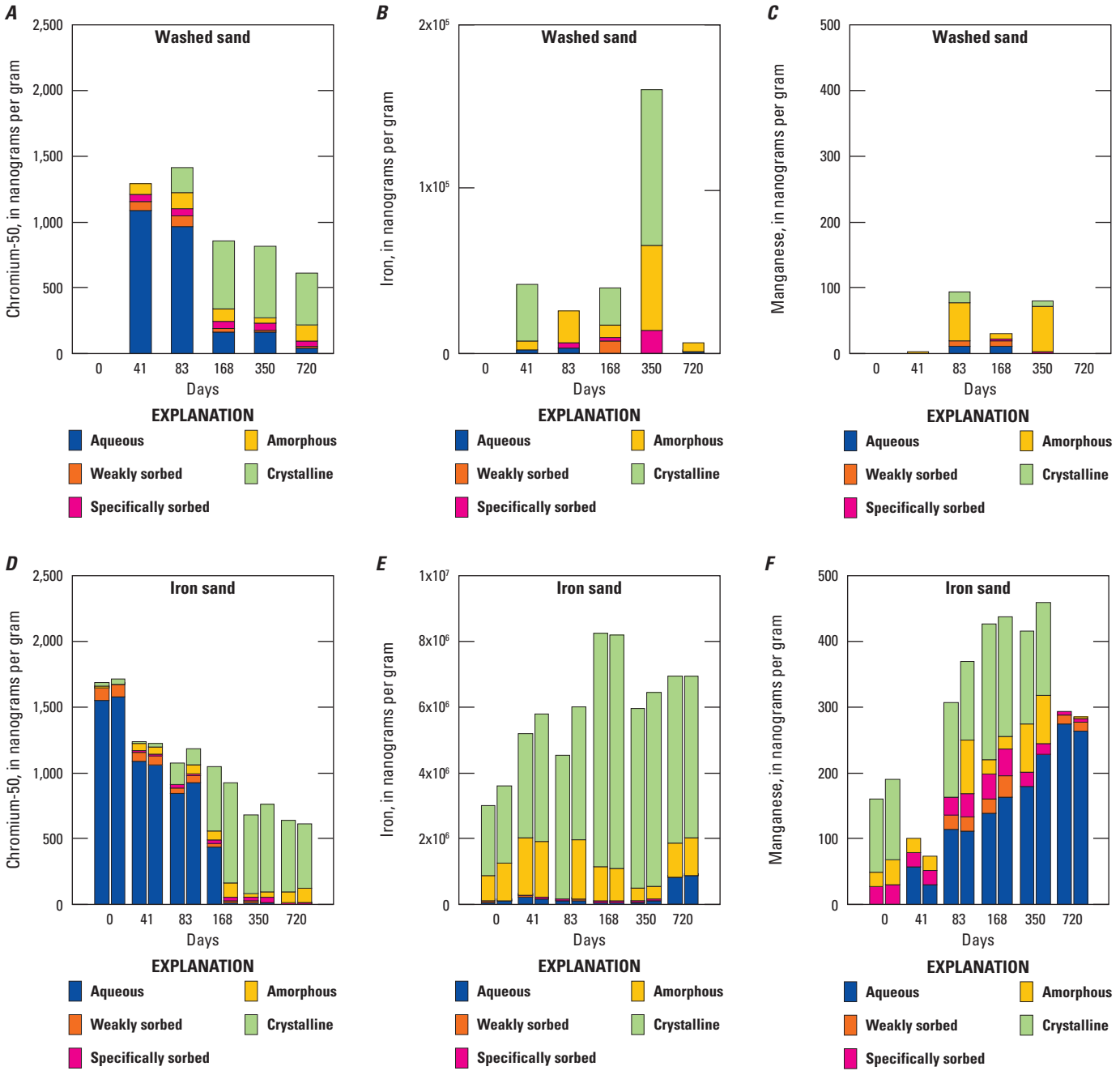

Figure I.5. Cumulative amounts of *A*, chromium-50; *B*, iron (Fe); and *C*, manganese (Mn) obtained from washed sand and cumulative amounts of *D*, chromium-50; *E*, Fe; and *F*, Mn obtained from iron-coated sand during sequential extractions of artificial substrates. Replicate analyses are presented side by side when available for the six incubation periods. Not all periods were sampled for washed sand. The horizontal axis is not scaled. Data are available in Miller and others (2020b).

Most of the chromium-50 recovered (greater than 600 ng/g) was in the crystalline phase after 168 days of reduction. This result was unexpected for washed sand incubations and indicated that substantial mineralization of Cr occurred in the absence of added Fe. Uptake of chromium-50 did not occur in separate incubations of sterile washed sand reacted for 108 and 248 days with autoclaved groundwater (fig. I.6).

Manganese was nearly absent (below reporting level) in all fractions recovered during sequential extractions of washed sand (fig. I.5*C*). In contrast, Mn values in Fe sand extractions (fig. I.5*F*) were low (hundreds of ng/g) and broadly distributed among the five operationally defined fractions. This Mn was identified as a minor contaminant of ferric chloride ($FeCl_3$) used to prepare the Fe sand.

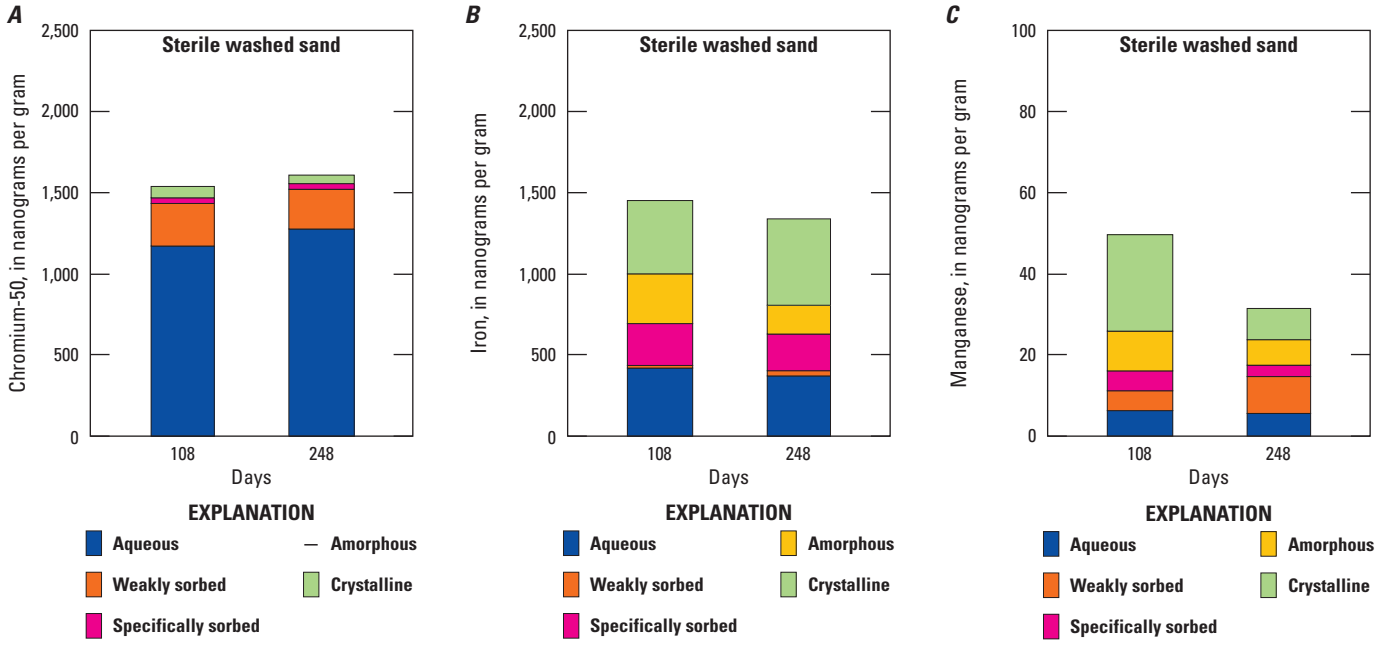

Figure I.6. Cumulative amounts of *A*, chromium-50; *B*, iron; and *C*, manganese obtained during sequential extractions of washed sand incubated with heat sterilized water from site BG-0004A. Microcosms were harvested after two periods without replication. The horizontal axis is not scaled similarly for all figure parts. Data are available in Miller and others (2020b).

I.3.3.3. Evolution of Solid Phases During Reduction

The aqueous chemical changes described above were coincident with and indicated transformations that occurred in solid phases during reduction. Solid-phase organic carbon was initially low (less than or equal to 0.2 percent by weight) in samples of aquifer material (table I.4) and increased to more than 6.6 percent by weight in samples measured after 1 year of reduction with added ethanol. Preliminary results indicate that the oxidation states of Cr-, Fe-, and Mn-bearing minerals evolved from more oxidized forms to more reduced forms during reduction of site materials and artificial substrates.

Interpretation of the physico-chemical state of solid phases at any time required diligent maintenance of the sample inventory (appendix table I.1.1) and direct comparison of analytical results with minerals and compounds of known chemical composition, mineralogy, and oxidation state (Foster and others, 2023). Concentrations of Cr, Fe, and Mn in bulk site materials measured by pXRF (table I.5) were comparable to results from other Mojave River aquifer material presented in Groover and Izbicki (2019). The pXRF analyses of Cr and Mn in precursor site BG-0004 also agreed well with (were overlapped by) results reported in chapter C within this professional paper. There was minor variation in the concentration of Cr and Mn with the method of sample preparation (bulk, sieving, grinding, or micronizing). Chromium was below or just slightly above the approximate detection limit of 8 mg/kg in all bulk precursor site materials (table I.5).

Precursor site materials had identifiable Fe- and Mn-oxide fractions present as surface coatings on larger grains including hematite (fig. I.7), hausmannite (fig. I.8), and ferrihydrite (fig. I.9) and within distinct primary minerals, whereas precursor artificial substrates had surface coatings only and lacked primary minerals. Direct μRaman analysis of loose grains of precursor Mn-oxide coatings revealed that the mixed valence [Mn(II)/Mn(III)]-oxide hausmannite, was the predominant surface mineral coating. Similarly, direct μRaman analysis of precursor Fe sand confirmed that two-line ferrihydrite was the dominant surface mineral coating. This form of ferrihydrite is the least crystalline and forms only two broad peaks (lines) in conventional X-ray powder diffraction (XRD).

Based on SEM-EDS, precursor site materials consisted of sand grains, minerals, and mineral fragments in a variety of weathering states, from sharp angular quartz and feldspars to distinct oxide minerals and clays; many particles were coated with material that included Fe, Mn, and occasionally Cr (table I.6; fig. I.10). Chromium was present mostly as embedded grains in coatings on larger mineral fractions or associated with clay minerals, as seen in site BG-0004 (figs. I.10*A–B*). Site SA-SB-01 (figs. I.10*C–E*) from within the IRZ showed Cr associated with potassium (K) and S (possibly in the sulfate mineral jarosite; fig. I.10*D*) in addition to Cr associated with clays (fig. I.10*E*). Although only limited substitution of chromium within clay minerals in Hinkley Valley was identified by Morrison and others (2019), higher chromium concentrations were associated with clay-rich material weathered from mafic, lacustrine, and granitic provenances than in coarse-textured felsic materials in the study area (chapter C, fig. C.11).

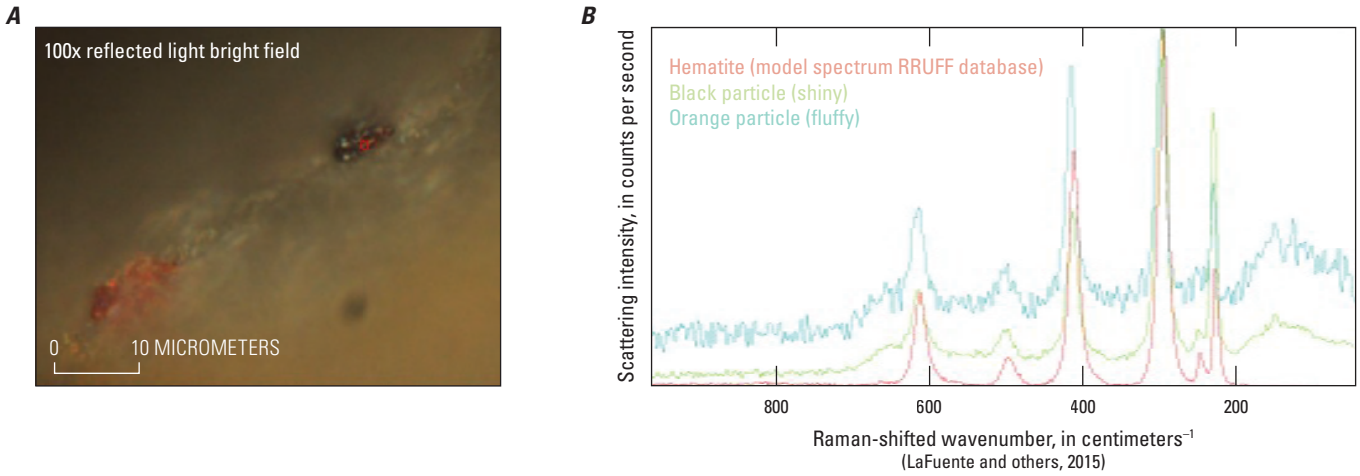

Figure I.7. *A*, An example microRaman image of iron oxides on quartz from site BG-0004 precursor material and *B*, a graph showing spectra of two oxide particles (red dots in figure I.7*A*) and a library model compound (hematite). Data are available in Foster and others (2023).

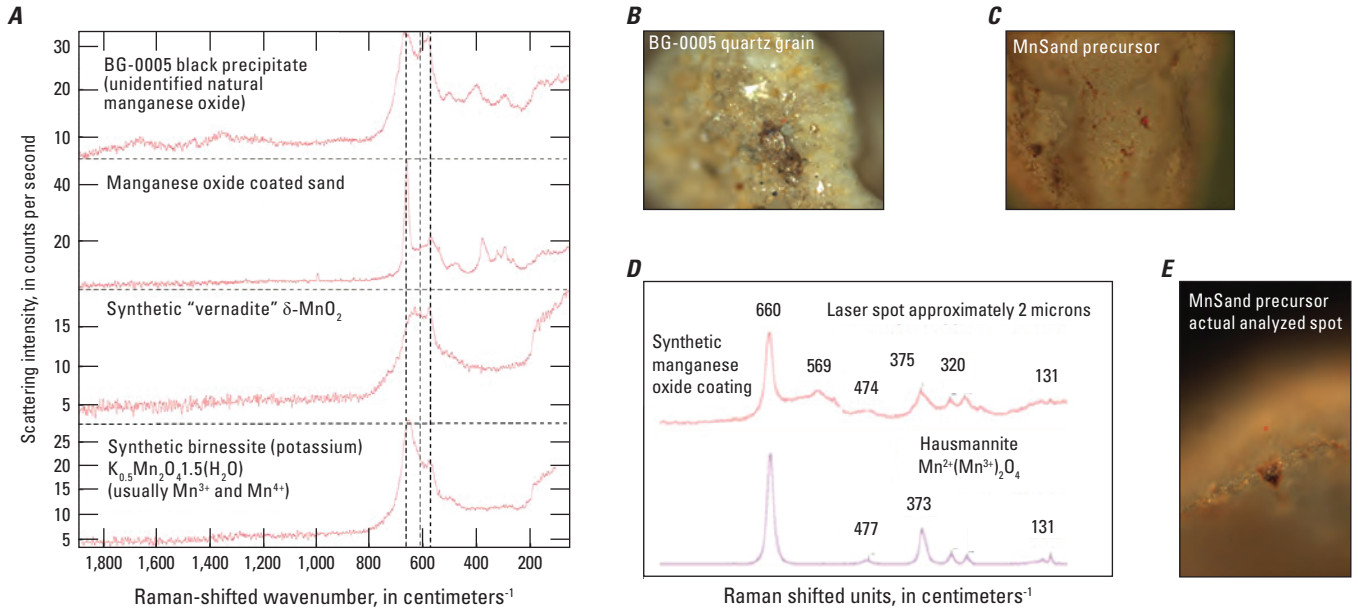

Figure I.8. MicroRaman spectra *A,* from black precipitate on site BG-0005, manganese-oxide coated sand, synthetic vernadite, and synthetic birnessite; photomicrographs showing *B,* oxide coatings on a quartz mineral grain from BG-0005 and *C,* manganese sand precursor; *D,* microRaman spectra from synthetic manganese coating and hausmannite, and *E* photomicrograph showing manganese sand location analyzed. Data show lack of congruence between spectra of library model compounds vernadite and birnessite and congruence between spectra of hausmannite. Data are available in Foster and others (2023).

To avoid working near the detection limits of SEM-EDS and XAS, Cr was concentrated in reduced solid phases by a factor of 10 during the elevated Cr experiment. This allowed an investigation into which crystalline phases were associated with Cr after reduction. Even so, it was only possible to analyze Cr effectively after the fine-grained Cr-containing coatings were separated from the bulk site material and coated sands. Abrasion provided by 2 minutes of vortex mixing dislodged enough fine material after drying to collect for direct observation by SEM-EDS or for grinding and loading into sample holders for XAS analysis.

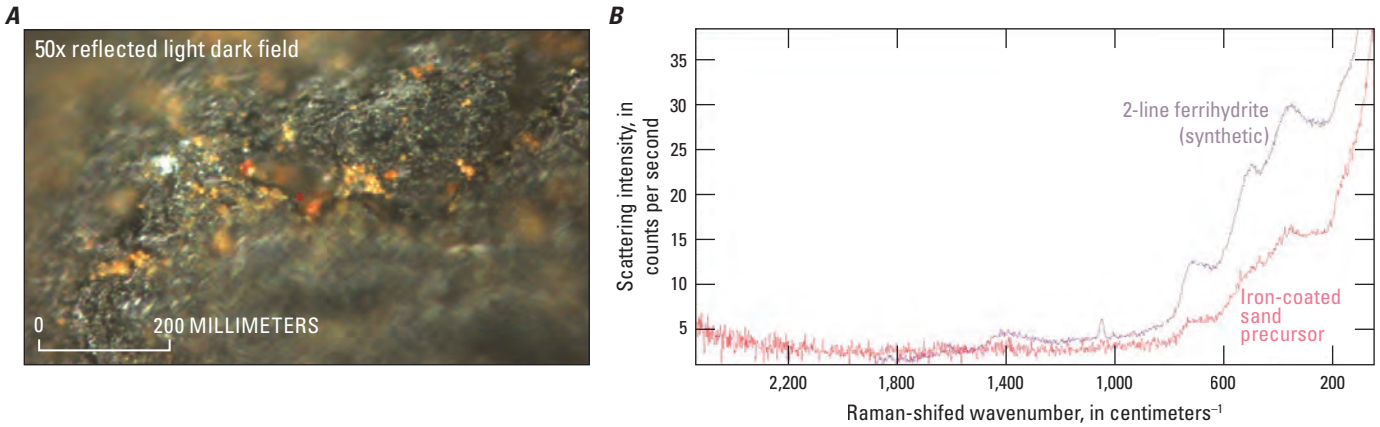

Figure I.9. *A*, A reflected light (RL), dark field optical image and *B*, a microRaman spectrum of iron-coated sand precursor depicting congruence with synthetic two-line ferrihydrite. Data are available in Foster and others (2023).

Table I.6. Compositional data (selected elements) derived from scanning electron microscopy with energy dispersive spectroscopy (SEM-EDS) spectra.

[Due to space limitations, data are presented only for samples shown in the figures of this report and are further restricted to analyses in which chromium (Cr) was detected at or above the three-sigma threshold (0.1 percent by weight). Data are available in Foster and others (2023). See text for preparation details. **Abbreviations**: Mn, manganese; Fe, iron; Si, silicon; Al, aluminum; Cl, chlorine; S, sulfur; Na, sodium; Mg, magnesium; K, potassium; Ca, calcium; TS, thin section; GM, grain mount]

Preparation	Preliminary mineral identification	Cr	Mn	Fe	Si	Al	Cl	S	Na + Mg + K + Ca
	SA-SB-01 precursor								
TS	Fe-clay 2:1, illite like	0.2	0.0	42.4	12.7	5.2	0.3	0.0	5.6
TS	Iron hydroxide	0.0	0.1	53.3	4.4	0.2	1.2	0.8	2.4
TS	Secondary Fe silicate	0.0	0.0	51.9	15.8	0.2	1.2	0.5	2.1
TS	Quartz	0.0	0.0	7.8	43.4	0.1	0.4	0.1	0.2
	Mn sand precursor								
TS	Manganese oxide	0.0	74.8	0.0	1.4	0.0	0.8	0.0	0.2
TS	Manganese silicate	0.0	39.4	0.0	16.2	0.3	0.3	0.2	0.6
TS	Quartz	0.0	0.0	1.0	32.4	0.1	0.0	9.0	0.7
	BG-0005, elevated Cr reduction, 8 months (fine-texture fraction)								
GM	Spinel group-Mn free	12.9	0.0	85.9	1.1	0.0	0.0	0.0	0.0
GM	Hematite or spinel like	11.9	7.4	73.3	2.0	0.0	0.0	0.0	0.0
GM	Spinel-like or Fe-Cr hydroxide	10.7	8.4	69.5	3.1	1.7	0.0	0.0	0.0
GM	Fe-Cr hydrox-substituted	8.4	6.0	51.4	5.9	2.8	0.0	0.0	0.0
GM	Altered illite	5.7	4.8	37.7	7.9	3.5	0.0	0.0	1.5
GM	Altered chlorite	3.7	2.5	21.2	11.4	5.0	0.0	0.0	5.3
GM	2:1 clay montmorillonite	3.9	3.1	24.0	13.7	6.1	0.0	0.0	4.2
GM	Chlorite	4.0	1.4	23.9	10.5	5.3	0.0	0.0	2.1
GM	Magnetite (1)	0.6	0.0	43.0	9.4	4.2	0.0	0.0	3.6
GM	Altered amphibole, for example anthophyllite	3.4	2.5	21.6	25.3	0.9	0.0	0.0	7.3
GM	Magnetite (2)	13.3	0.0	76.5	0.0	0.0	0.0	0.0	0.0
GM	Altered chlorite	6.7	0.0	52.3	9.0	4.7	0.0	0.0	0.0

Table I.6. Compositional data (selected elements) derived from scanning electron microscopy with energy dispersive spectroscopy (SEM-EDS) spectra.—Continued

[Due to space limitations, data are presented only for samples shown in the figures of this report and are further restricted to analyses in which chromium (Cr) was detected at or above the three-sigma threshold (0.1 percent by weight). Data are available in Foster and others (2023). See text for preparation details. **Abbreviations**: Mn, manganese; Fe, iron; Si, silicon; Al, aluminum; Cl, chlorine; S, sulfur; Na, sodium; Mg, magnesium; K, potassium; Ca, calcium; TS, thin section; GM, grain mount]

Preparation	Preliminary mineral identification	Cr	Mn	Fe	Si	Al	Cl	S	Na + Mg + K + Ca
	SA-SB-01, oxidation experiment, 14 days								
TS	Fe sulfide (clay contamination)	0.0	0.2	25.9	9.3	3.8	0.0	19.2	4.7
TS	Clay surrounding sulfide grain	0.0	0.0	13.6	18.1	9.1	0.0	0.4	4.9
	BG-0005, oxidation experiment, 0 days								
TS	Fe hydroxide with Mn and Cr	0.2	0.2	61.2	3.3	1.3	0.3	0.0	0.0
	Fe/Mn 50, oxidation experiment, 0 days								
TS	Unknown; likely mixed analysis	47.6	1.0	4.9	16.2	1.2	0.5	0.5	5.6
TS	Fe hydroxide (substituted) or FeCr hydroxide	0.8	1.1	32.7	10.4	3.4	2.1	0.9	3.9
TS	Fe silicate with Cr	0.2	0.0	28.7	24.0	0.5	0.5	0.5	1.8
	Fe/Mn 25, oxidation experiment, 56 days								
TS	Fe hydroxide or aluminosilicate	0.5	0.5	44.6	8.4	0.8	0.4	0.8	2.7
TS	Mn hydroxide	0.4	52.7	9.8	3.0	0.9	0.9	0.8	2.0
TS	Jacobsite (intermediate between 1 and 2 endmembers	1.0	41.4	35.1	6.8	1.3	0.5	0.7	2.4
TS	CaFe silicate, highest S outside of sulfide	0.2	1.6	30.1	6.5	1.4	0.3	7.2	2.4
TS	Fe silicate	0.0	0.0	15.0	29.4	0.9	0.8	0.0	11.3
	Quality control samples								
	Fe/Mn 25, oxidation experiment, 56 days								
TS	Epoxy (see Cl)	0.0	0.0	4.0	0.0	0.0	19.6	0.0	4.7
	BG-0005, elevated Cr reduction, 8 months (fine-texture fraction)								
GM	Quartz	0.0	0.0	0.0	26.3	0.0	0.0	0.0	0.0
	SA-SB-01, oxidation experiment, 0 days								
TS	Quartz	0.0	0.0	0.0	47.1	0.0	0.0	0.0	0.0

Precursor fine materials were analyzed, and Cr was not found by any method of detection. Precursor fine materials dislodged from BG-0004 and BG-0005 (figs. I.11*A–B*) were composed mostly of mineral fragments and some clays. Almost no fine material was associated with precursor washed sand (fig. I.11*C*), whereas quartz grains were blanketed by ferrihydrite in precursor Fe sand (fig. I.11*D*).

Scanning electron micrographs of site materials collected after 1–2 years of reduction showed an increase in the amount of secondary minerals, especially clays. Figures I.12*A* and I.12*B* show the presence of a variety of large and small particles in BG-0004 and BG-0005 as well as agglomerations of particles of different sizes and textures. Figure I.13 shows site SA-SB-01 in slightly greater detail, emphasizing the presence of diffuse coatings on grain surfaces and the presence of stacked clay platelets. The small (less than 5 micrometers wide), bright minerals visible between clay layers (figs. I.13*C–D*) are assumed to be secondary minerals formed within the reduced microcosms; they were primarily composed of Fe and S, according to EDS spectra. The habit, geochemical condition, and composition all indicated that the small particles were Fe sulfide.

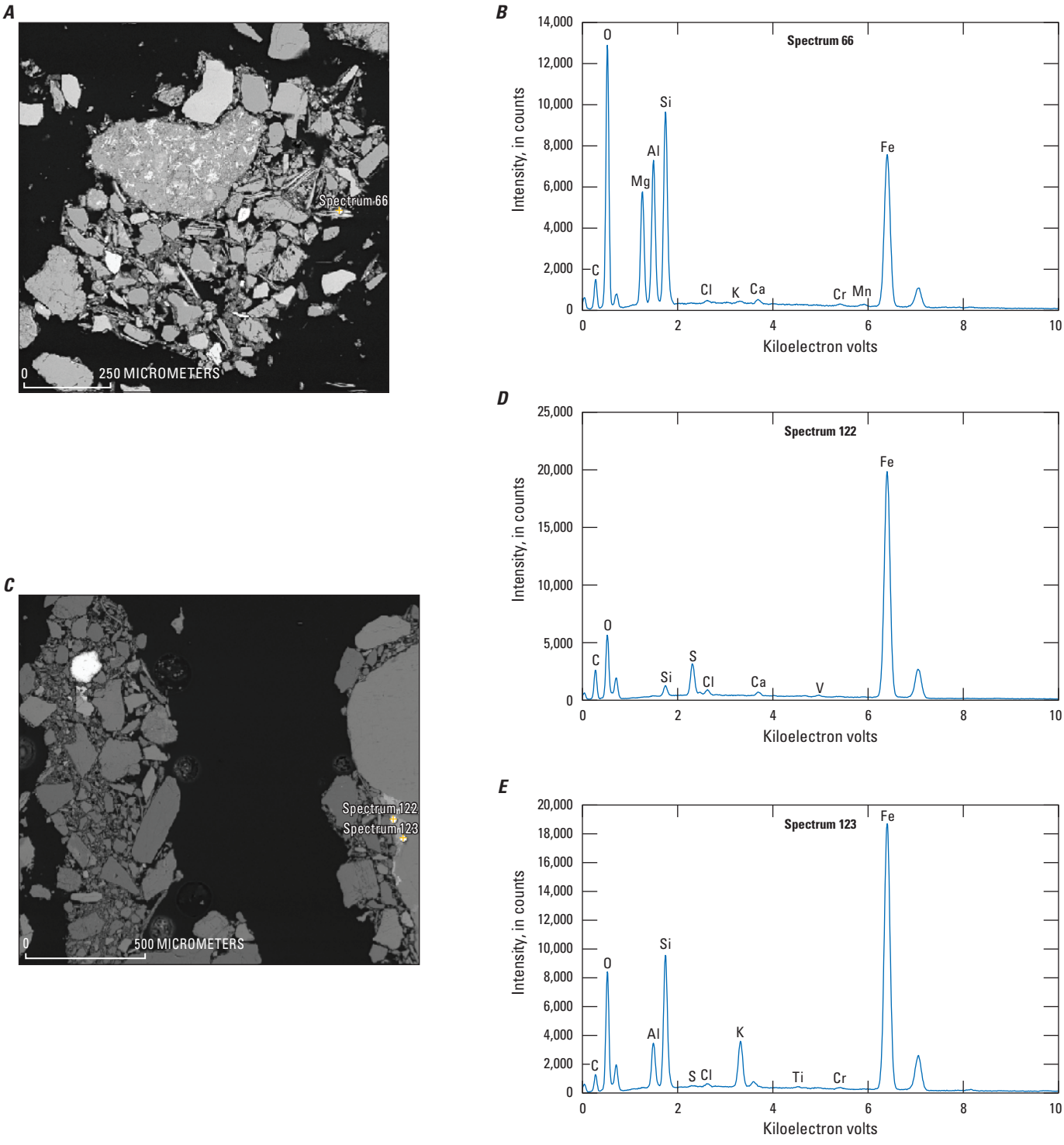

Figure I.10. Backscatter scanning electron micrographs (*A*, site BG-0004; *C*, site SA-SB-01) and example spectra (*B*, site BG-0004; *D* and *E* site SA-SB-01) of selected bright areas of thin sections prepared using bulk precursor site materials illustrating chromium (Cr) surrounded by Cr-free areas. Data are available in Foster and others (2023). [Al, aluminum; C, carbon; Ca, calcium; Cl, chloride; Cr, chromium; Fe, iron; K, potassium; Mg, magnesium; Mn, manganese; O, oxygen; S, sulfur; Si, silicon; T, titanium; V, vanadium]

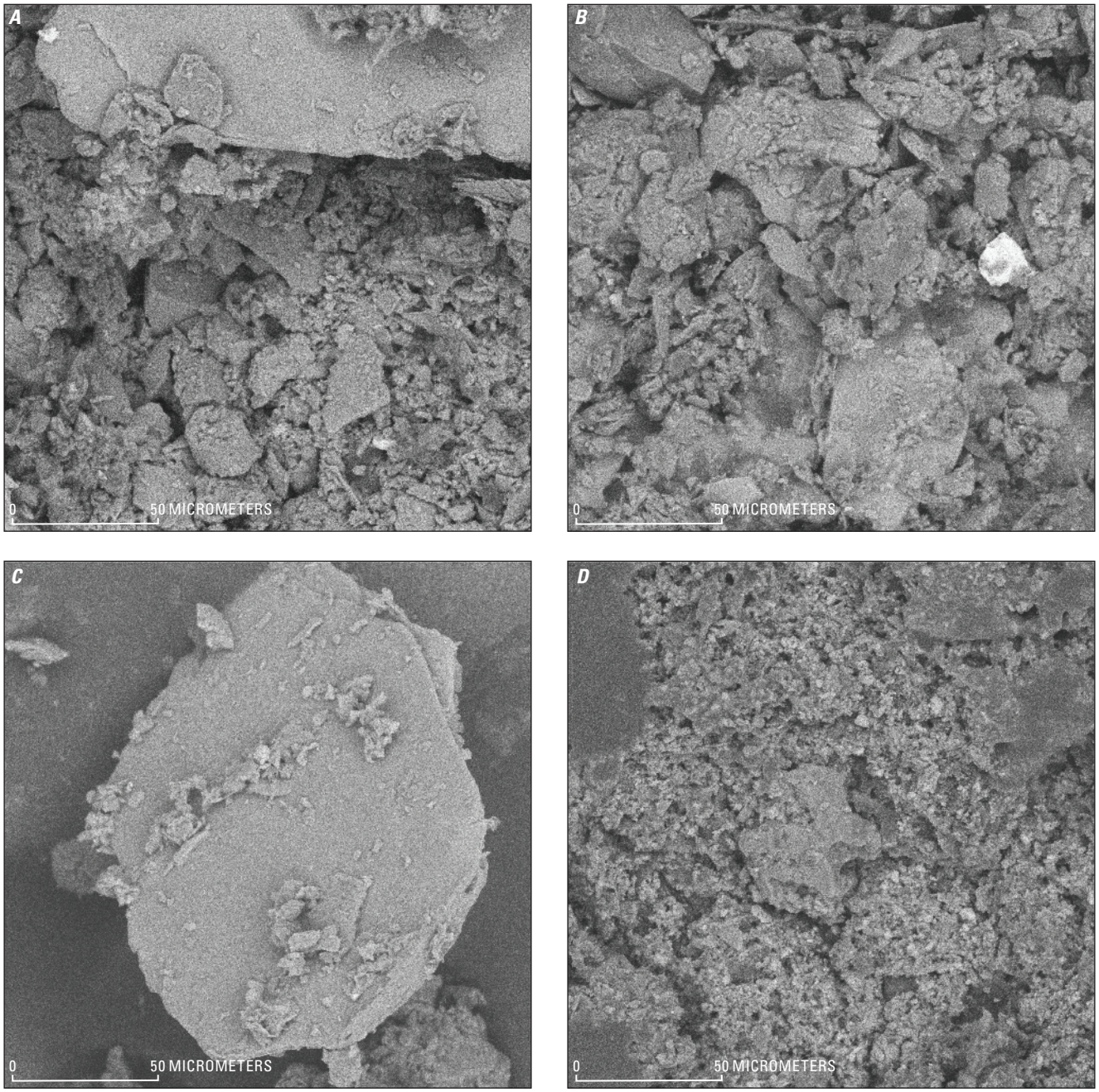

Figure I.11. Scanning electron micrographs of vortex-liberated fine material from precursor materials at sites *A*, BG-0004 and *B*, BG-0005 artificial substrates *C*, washed sand, and *D*, iron-coated sand. Data are available in Foster and others (2023).

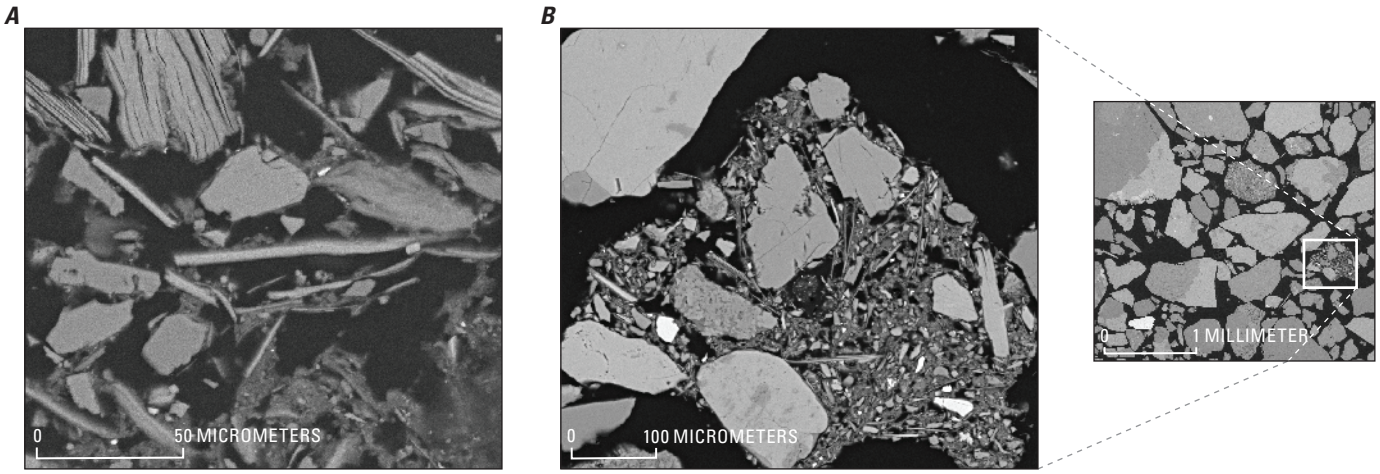

Figure I.12. Backscattered scanning electron micrographs of sites *A*, BG-0004 and *B*, BG-0005 sampled after 1.25±0.2 years of reduction (day 0 of the oxidation experiment). Brightness corresponds with higher average atomic number (Z) and density of particles. Data are available in Foster and others (2023).

Fine material collected after 5 and 8 months of reduction in the elevated Cr reduction experiment contained enough Cr to measure by pXRF, SEM-EDS, and XAS. As measured by pXRF (table I.5), the fine fraction of BG-0004 material contained 123±12 mg/kg Cr, approximately ten times that of the BG-0004 precursor material and more than three times that of the corresponding bulk sample from the microcosm. Similarly, the fine fraction of BG-0005 material measured 139±14 mg/kg Cr, which is approximately three times that measured in the corresponding bulk sample from the microcosm (table I.5). In contrast, after 8 months of reduction the washed sand was only slightly higher than the initial concentration (10 mg/kg Cr), and the measured concentration was just barely higher than the ±20 percent three-sigma instrument error associated with these measurements (table I.5).

The SEM-EDS analysis of site materials from the elevated Cr experiment (fig. I.14) revealed areas of elevated Cr concentration which also were associated with high concentrations of Fe or Mn (or both). Numerous bright spots were observed on the edges of grains and as coatings on top of larger minerals which when analyzed contained marked amounts of Cr and Fe together and in some cases, Cr, Fe, and Mn.

Plotting Cr, Mn, and Fe together in a ternary diagram (fig. I.15*A*) illustrates the relations among Cr, Fe, and Mn in BG-0004 and BG-0005 after reduction. Data plotting along the base of the diagram represent locations where Cr and Fe were co-located. Data plotting above the base represent locations where Mn also was present. Locations containing Fe and Mn but not containing Cr, plot along the Fe-Mn axis. The cluster of data in the mid-field, containing between 10 and 20 percent Cr by weight, 10 percent Mn by weight, and between 70 and 80 percent Fe by weight were mostly collected from BG-0005 fines. Only three samples containing Cr, Mn, and Fe were from BG-0004, although a comparable number of locations were analyzed from each site. Additionally, the ternary diagram (fig. I.15*A*) shows Cr is co-located with Mn in iron minerals at ratios almost an order of magnitude greater than the ratio of Mn to Fe in the surface coatings of native materials (chapter C, fig. C.14), consistent with a preferred tendency for co-location and substitution of Cr together with Mn in iron mineral structures during reduction.

Separately evaluating the relations of Cr to Fe and Cr to Mn revealed additional patterns in these data. Figure I.15*B* demonstrates that samples containing Cr and Fe plot on a line with slope greater than the ideal Fe/Cr ratio of 3.0 found in Fe-Cr hydroxide (Fe_{1-x} $Cr_x(OH)_3.nH_2O$) (Klein, 1998). Figure I.15*C* shows that samples containing Mn and Cr plot on a line with a slope (Mn/Cr) less than 1, and that co-location of Cr with Mn was far more commonly observed in BG-0005 than in BG-0004 fines.

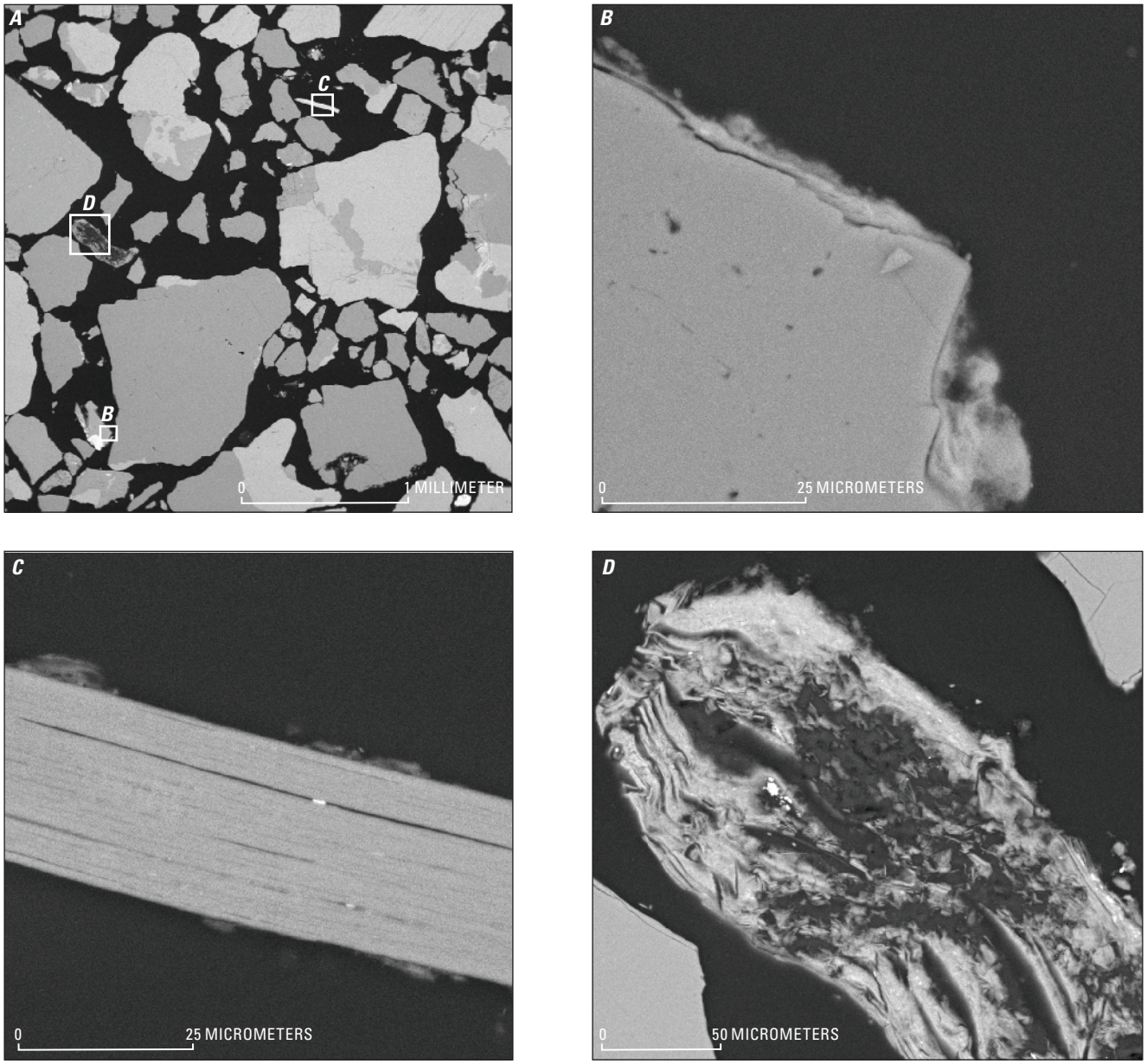

Figure I.13. Backscattered scanning electron micrographs of site SA-SB-01 sampled after 1.25±0.2 years of reduction (day 0 of the oxidation experiment) in *A,* a full field image and *B–D,* in close-up images. Brightness corresponds with a higher average atomic number (Z) and density of particles. Data are available in Foster and others (2023).

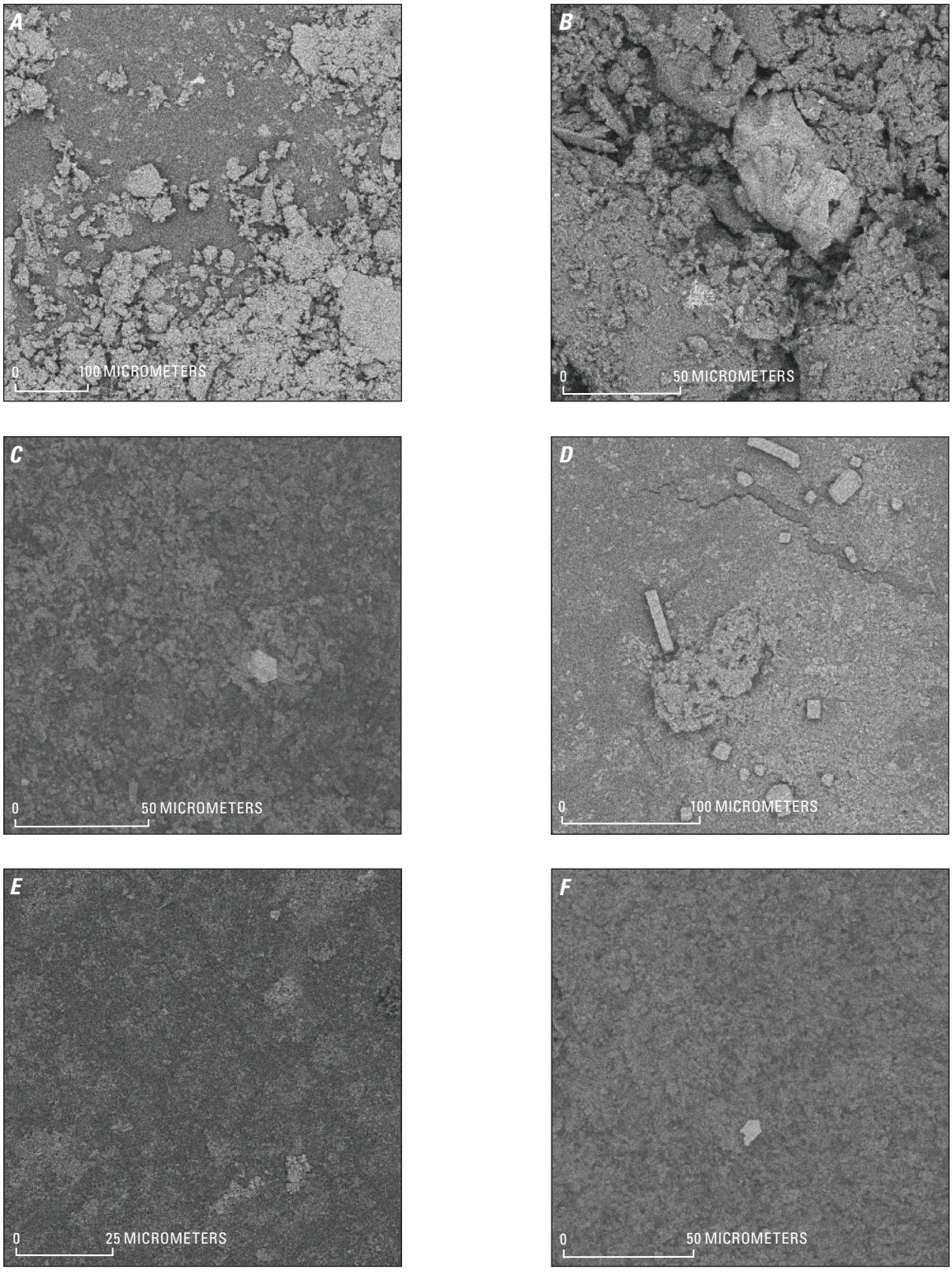

Figure I.14. Scanning electron micrographs of vortex-liberated fine fraction from site materials *A*, BG-0004 and *B*, BG-0005 after 8 months of reduction during the elevated chromium experiment and artificial substrates *C*, Fe/Mn 25; *D*, Fe/Mn 50; *E*, Fe/Mn 100; and *F*, manganese-coated sand after 1.25 years reduction in the oxidation experiment. Compositional data collected from particles in these images are available in Foster and others (2023).

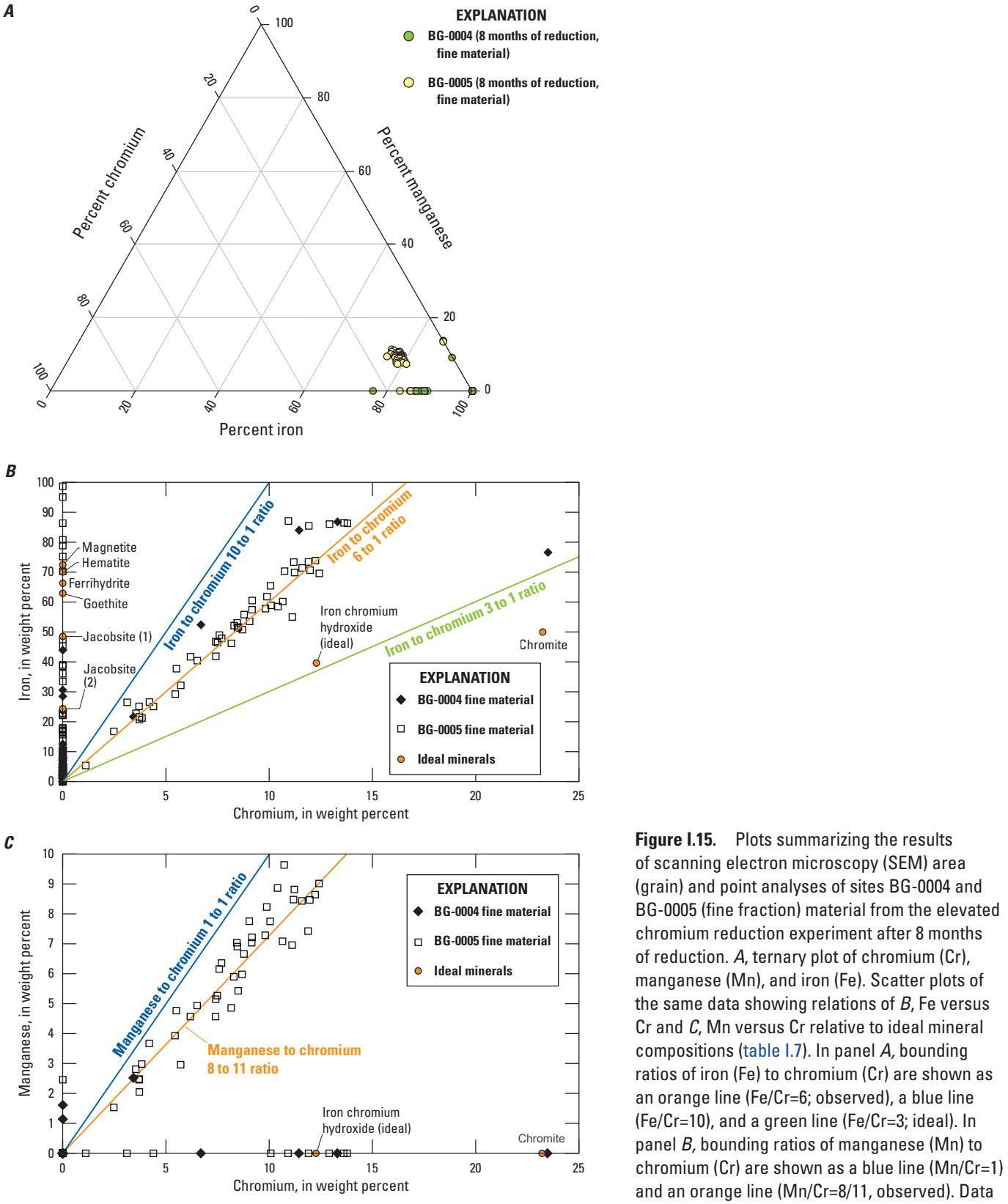

Figure I.15. Plots summarizing the results of scanning electron microscopy (SEM) area (grain) and point analyses of sites BG-0004 and BG-0005 (fine fraction) material from the elevated chromium reduction experiment after 8 months of reduction. *A*, ternary plot of chromium (Cr), manganese (Mn), and iron (Fe). Scatter plots of the same data showing relations of *B*, Fe versus Cr and *C*, Mn versus Cr relative to ideal mineral compositions (table I.7). In panel *A*, bounding ratios of iron (Fe) to chromium (Cr) are shown as an orange line (Fe/Cr=6; observed), a blue line (Fe/Cr=10), and a green line (Fe/Cr=3; ideal). In panel *B*, bounding ratios of manganese (Mn) to chromium (Cr) are shown as a blue line (Mn/Cr=1) and an orange line (Mn/Cr=8/11, observed). Data are available in Foster and others (2023).

Table I.7. Ideal mineral compositions (Klein, 1998).

[g/mol, grams per mole; Fe, iron; Mn, manganese; Cr, chromium; O, oxygen; H, hydrogen; δ, delta polymorph; K, potassium; α, alpha polymorph]

Mineral name	Ideal stoichiometry	Ideal formula weight (g/mol)	Composition in percent by weight				
			Fe	Mn	Cr	O	H
Hematite	Fe_2O_3	159.69	69.94	0.00	0.00	30.06	0.00
Bixbyite	$Mn^{2+}{}_2O_3$	157.87	0.00	69.60	0.00	30.40	0.00
Magnetite	$Fe^{2+}Fe^{3+}{}_2O_4$	231.53	72.36	0.00	0.00	27.64	0.00
Chromite	$Fe^{2+}Cr^{3+}{}_2O_4$	223.83	24.95	0.00	46.46	28.59	0.00
Jacobsite (1)	$Mn^{2+}Fe^{3+}{}_2O_4$	230.62	48.43	23.82	0.00	27.25	0.00
Jacobsite (2)	$Fe^{2+}Mn^{3+}{}_2O_4$	229.72	24.31	47.83	0.00	27.86	0.00
Hausmannite	$Mn^{2+}Mn^{3+}{}_2O_4$	228.81	0.00	72.03	0.00	27.97	0.00
Vernadite	δ-MnO_2	86.94	0.00	63.19	0.00	36.81	0.00
Birnessite	$K_{0.5}Mn_2O_4$	193.42	0.00	56.81	0.00	33.09	0.00
Ferrihydrite	$(Fe^{3+})_2O_3 \bullet 0.5H_2O$	168.69	66.21	0.00	0.00	33.19	0.60
Goethite	α-FeOOH	88.85	62.85	0.00	0.00	36.01	1.13
Chromium hydroxide	$Cr(OH)_3$	103.02	0.00	0.00	50.47	46.59	2.94
FeCr hydroxide	$Cr_{0.25}Fe_{0.75}(OH)_3$	105.90	39.55	0.00	12.27	45.32	2.86

Additional evidence of co-location of Fe and Mn on a µm scale is provided by SEM-EDS analysis of artificial substrates after prolonged reduction. Backscattered scanning electron micrographs of Fe/Mn 50 collected after 1.25±0.2 years reduction showed evidence of precipitate formation at the edges of large grains (fig. I.16). Full field and close-up images of two areas are shown on figures I.16*A–F*. Area EDS maps were collected at the locations shown in figures I.16*C–D*. The results of multi-element mapping of these areas are presented as tricolor maps (figs. I.16*G–H*). A single grain of Cr (greater than 27 percent by weight) as well as Mn-rich (green) areas are embedded in the filmy coating on the outside surface of the Fe-rich (blue) areas (fig. I.16*G*). In other regions, Fe exists without Mn (fig. I.16*H*).

X-ray absorption near edge structure spectra were used to determine the oxidation state of Cr, Fe, and Mn in field samples and from samples collected during reduction, elevated-Cr, and oxidation experiments. Shifts in peak energies or the relative height of adjacent peaks indicate changes in the valence state or relative abundance of co-occurring valence states of a given element. An operational Cr detection limit of 10–50 mg/kg was determined by analyzing serial dilutions (by 10) of a mixture of chromite and sodium chromate/silica (ES7; Mills and others, 2017) containing about 1 percent by weight total Cr with about 95 percent as Cr(III) and about 5 percent as Cr(VI) (fig. I.17). Detectable dilutions included 1:100 (100–500 mg/kg Cr) and 1:1,000 (10–50 mg/kg Cr) but not 1:10,000 (1–5 mg/kg Cr). Although many of the experimental solid-phase samples were below this operational 10–50 mg/kg limit, it was possible to collect XANES spectra and derive useful information for Cr from several samples where Cr concentration exceeded the detection limit, even when some Cr(0) contamination signal was present.

Differences in line shape between the Cr XANES spectra of site BG-0004 samples from the 83- and 350-day timepoints of the preliminary reduction experiment indicate a change in speciation during this period (fig. I.18*A*). At 83 days, the Cr XANES spectrum resembles the "Fe-Cr^{3+} hydroxide" spectrum in which Cr(III) is co-precipitated with Fe(III) in a hydroxyl coordination environment (fig. I.18*A*, *B*; panel *B* from Hansel and others, 2003a). By 350 days, Cr in BG-0004 more closely resembles spectra of Cr(III)-substituted within magnetite or chromite; this is consistent with sequential extraction results from site BG-0004 (fig. I.3), which reports an increase in the amount of added chromium-50 associated with the crystalline phase after 83 days of reduction.

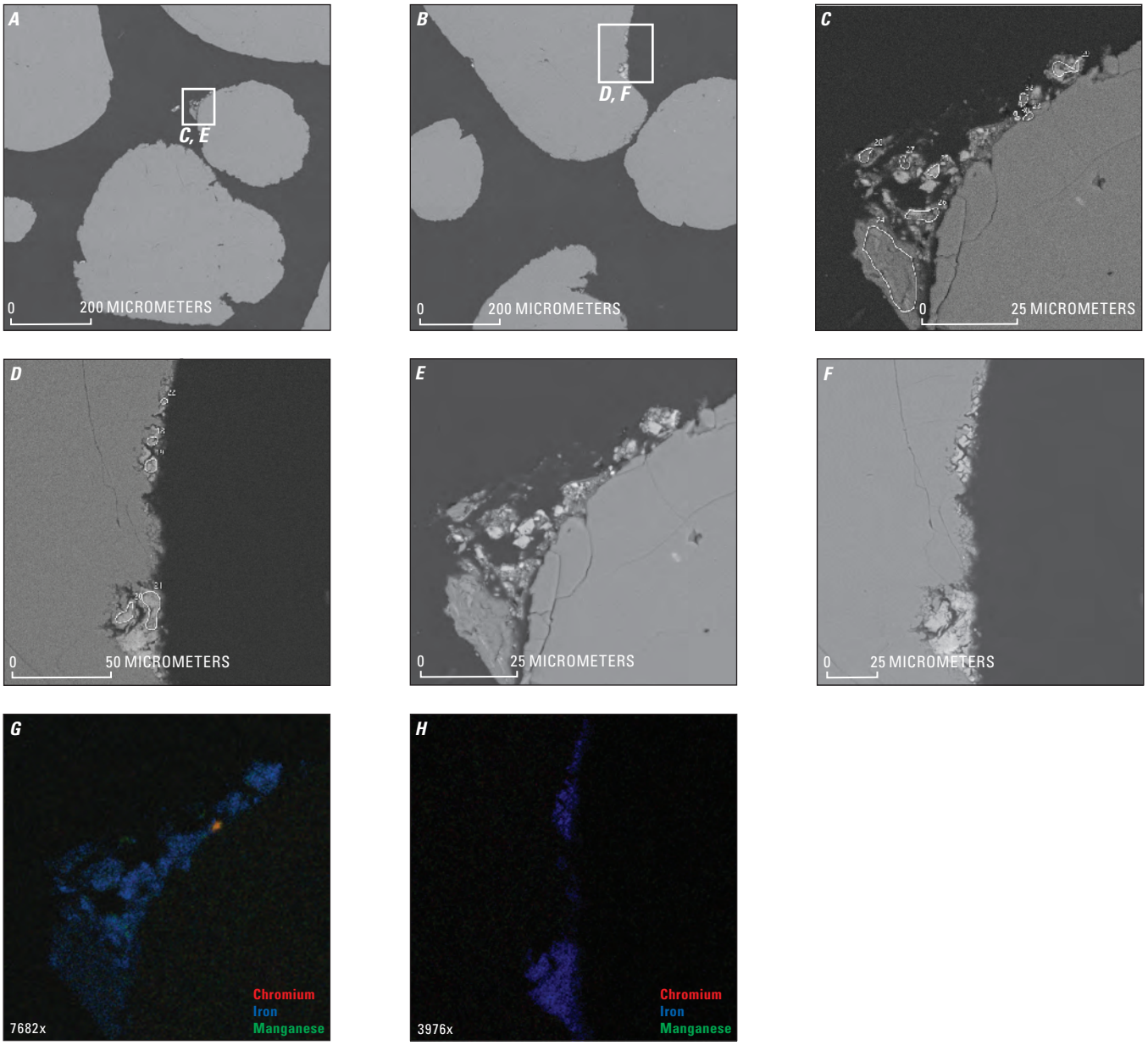

Figure I.16. Backscattered scanning electron micrographs showing (*A* and *B)* locations of two coatings on Fe/Mn 50 after 1.25±0.2 years of reduction with added chromium (Cr). Multi-element energy dispersive spectroscopy (EDS) maps were collected from (*C* and *D*) the areas shown in the respective close-ups; (*E* and *F*) higher resolution images of these regions also are shown; and (*G* and *H*) tricolor maps show co-located Cr, Mn, and Fe. Spectra corresponding to the areas in (*C* and *D)* are presented in Foster and others (2023).

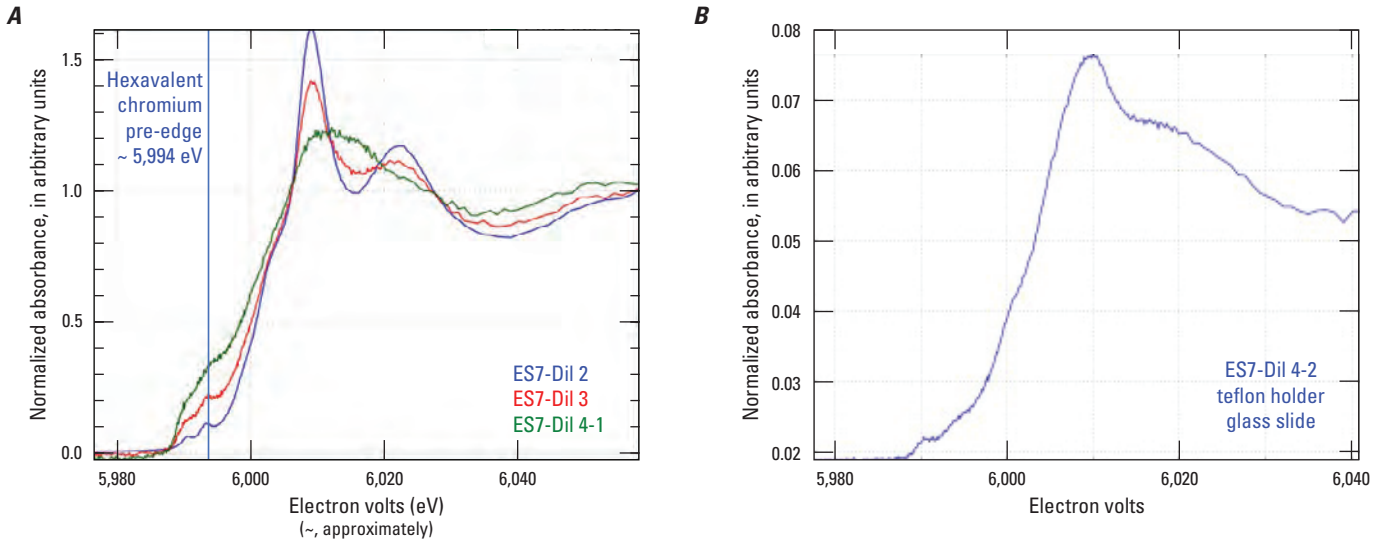

Figure I.17. *A,* Bulk chromium (Cr) X-ray absorption near edge spectra (Cr XANES) of external standard #7 (ES7; Mills and others, 2017) serial dilutions ("Dil") with Cr values of 100–500 milligrams per kilogram (mg/kg) for Dil 2, 10–50 mg/kg for Dil 3, and 1–5 mg/kg for Dil 4. The 5-percent hexavalent chromium, Cr(VI), content of ES7 is visible in Dil 2 and Dil 3 but not in Dil 4-1 primarily because of contamination from a metal spatula used to load the samples into Teflon holders, as well as from Cr in stainless steel components of the experimental setup. *B*, use of a glass slide instead of metal spatula to load Dil 4 into the Teflon holder (Dil 4-2) lowered but did not remove the Cr(0) contamination (compare to DIL 4-1 in I.17*A*). Data are available in Foster and others (2023).

Chromium was concentrated to observe reduced products greater than the detection limit in the elevated Cr reduction experiment. The XANES spectra of bulk and vortex-liberated fine material collected after 8 months of reduction for BG-0004 material showed greater similarity to magnetite (fig. I.19*A*) than to Fe-Cr hydroxide sand, whereas BG-0005 was more like Fe-Cr hydroxide sand (fig. I.19*B*). Extended X-ray absorption fine structure measured on fine material confirmed this pattern, with BG-0005 more like the Fe-Cr hydroxide sand model, and BG-0004 differing from the Fe-Cr hydroxide sand model (fig. I.19*C*). Panel *D*, a Fourier transform of the EXAFS in panel *C*, does not show meaningful differences in the samples beyond the first electron shell (k-shell). Additional information can be extracted from the data in fig I.19 to describe the potential phases represented, but there is a substantial limitation to analysis in that beyond the first-shell oxygen atoms, the next-closest neighbors are likely to be Fe or Mn atoms, both of which are difficult to distinguish from Cr (and from each other due to their similar number of electrons) by EXAFS spectroscopic analysis (Koningsberger and Prins, 1988); this emphasizes the need for the variety of bulk and micrometer-scale analytical techniques used in this study.

Areas of interest on petrographic thin sections were analyzed by backscattered SEM-EDS and XAS to obtain high resolution images and µXRF tricolor maps of Cr-Mn-Fe concentrations. The field of view on figure I.20*A* shows several large mineral grains and an on-edge clay grain (notable for its "frayed" sheet-like appearance) in BG-0005 after reduction. Figures I.20*B* and I.20*C* are tricolor maps (red, green, and blue) of either Cr, Mn, and Fe (respectively, on fig. I.20*B*) or potassium (K), calcium (Ca), and Si (respectively, on fig. I.20*C*) of a larger area encompassing the area on figure I.20*A* (the dashed-line rectangles on figs. I.20*B* and I.20*C* represent the fig. I.20*A* area). The backscattered electron-bright areas prominent on many grains in the upper left of figure I.20*A* contain Cr (red) or Cr associated with Fe (magenta), including the on-edge clay grain (fig. I.20*B*). A single particle of Mn-silicate can be observed (green on fig. I.20*B*; blue on fig. I.20*C*). Several of the Cr-rich regions co-occur with K (fig. I.20*C*) and appear to be surface coatings on potassium feldspar mineral grains. A Cr- and Ca-rich coating can be observed on the Ca-rich grain in the upper left of figure I.20*C*, tentatively identified as calcium feldspar (anorthite). Chromium-containing hydrocalcite surface coatings on mineral grains have been previously described within Cr(VI) plumes (Sedlazeck and others, 2017) and similar materials were observed coating aquifer materials within the regulatory Cr(VI) plume (chapter C, fig. C.21)

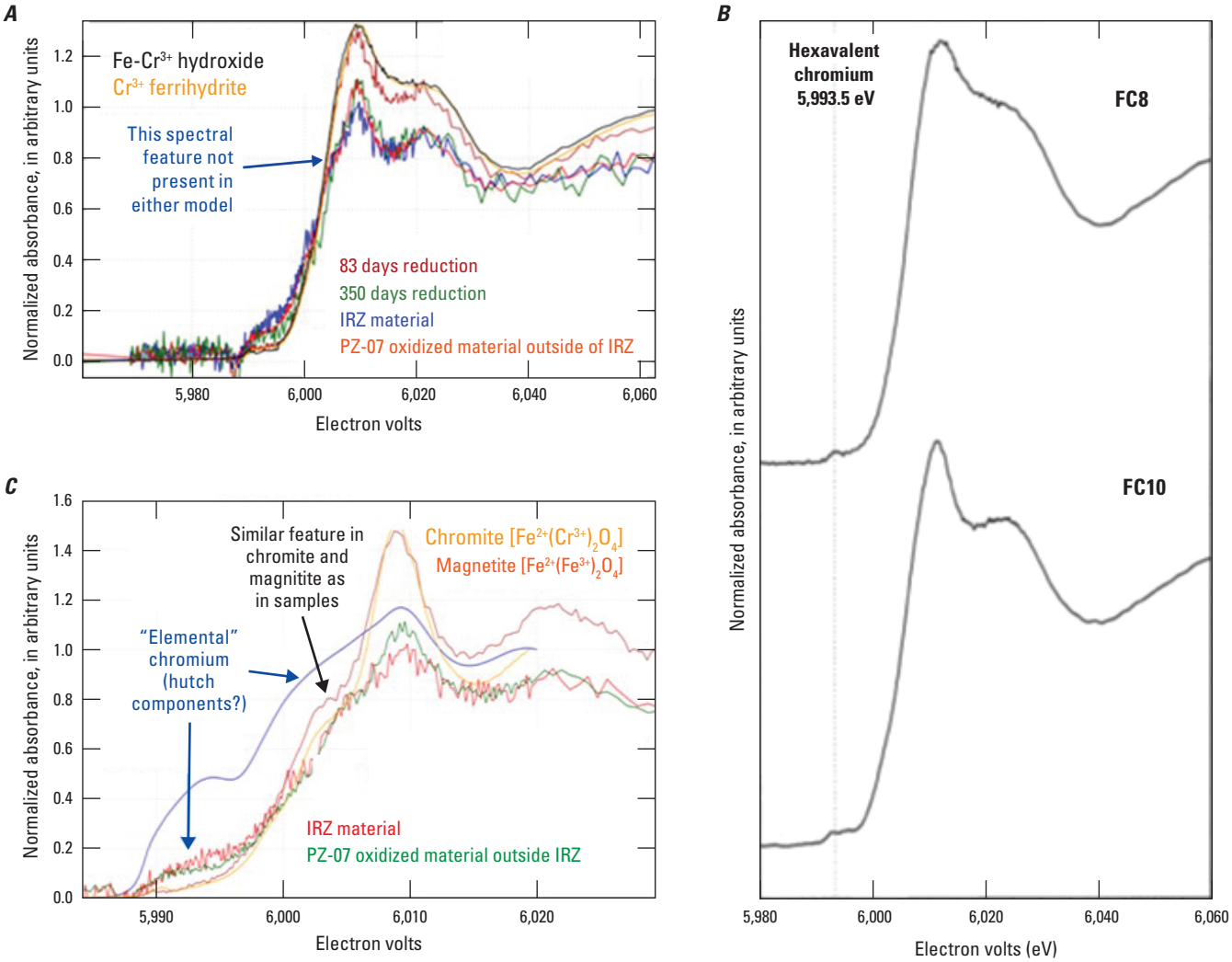

Figure I.18. Bulk chromium X-ray absorption near edge spectra (Cr XANES) *A*, comparing site BG-0004 at 83 days (HAF56) and 350 days (HAF53) of reduction with precursor SA-SB-01 (HAF14) and an environmental sample from PZ-07 (oxidized, non-contaminated aquifer material; see chapter C for details). The BG-0004 spectrum at 83 days of reduction resembles the spectrum of trivalent chromium coprecipitated with iron(III) but is not exactly the same; *B*, its features are similar to that of spectrum FC10 in Hansel and others (2003a); and *C*, site BG-0004 spectra at 350 days are like those of SA-SB-01 and PZ-07; all three resemble spectra of chromite and magnetite, in which chromium substitutes at trace to weight percent levels. Site BG-0004 spectra from 350 days of reduction plus SA-SB-01, and PZ-07 also show evidence of contamination by elemental chromium. Data are available in Foster and others (2023). [Cr^{3+}, trivalent chromium; Fe^{2+}, ferrous iron; Fe^{3+}, ferric iron; O, oxygen; IRZ; in situ reactive zone]

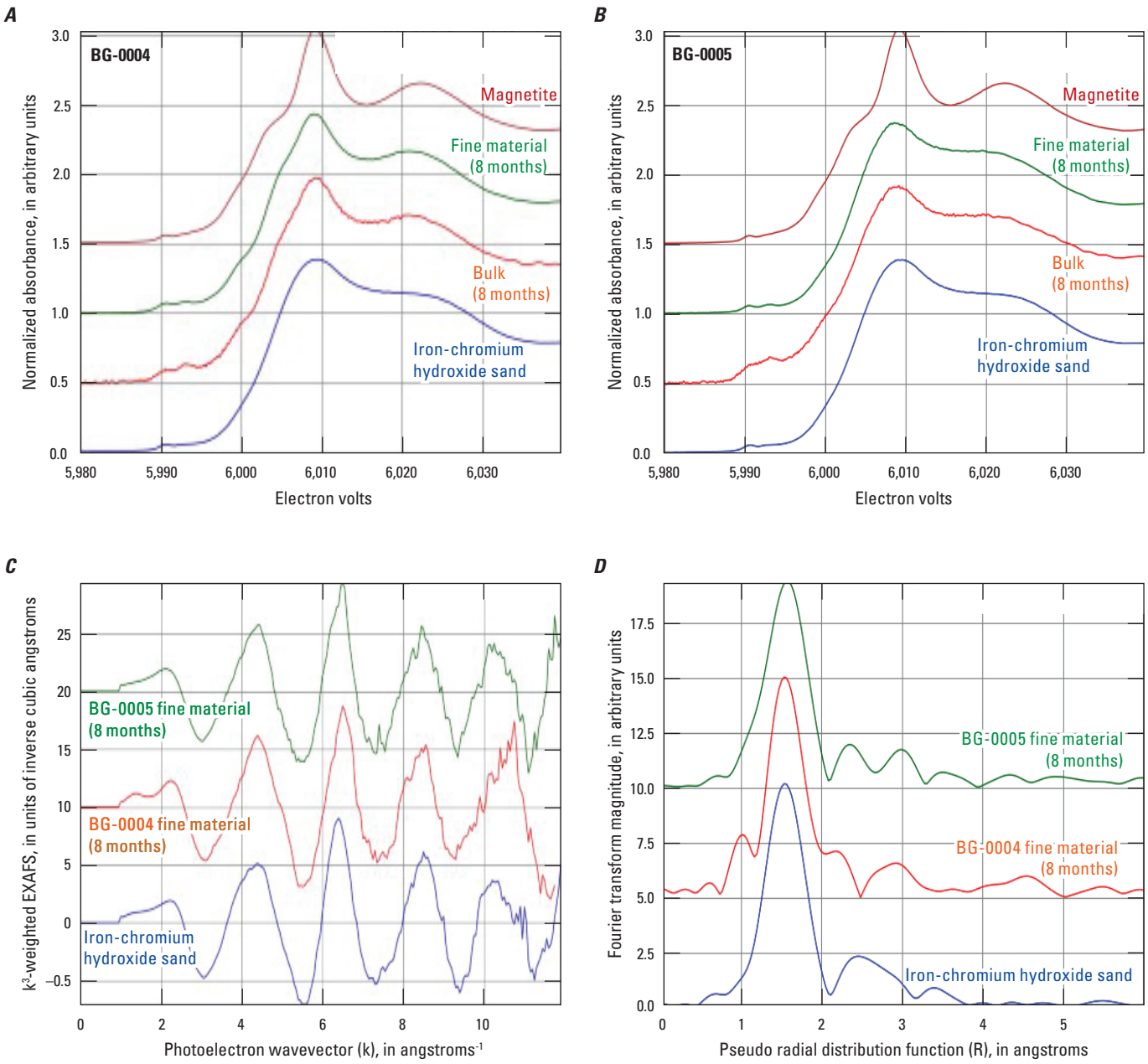

Figure I.19. Bulk chromium X-ray absorption near edge spectra (Cr XANES) comparing *A*, bulk and fine fraction of sites BG-0004 and *B*, BG-0005 8-month reduction samples from elevated chromium reduction experiment (table I.1) to magnetite and iron-chromium hydroxide sand model compounds. Comparison of *C*, chromium extended X-ray absorption fine structure (Cr EXAFS) spectra and *D*, pseudo radial distribution functions of the 8-month fine fractions of BG-0004 and BG-0005 from the same experiment to that of the iron-chromium hydroxide sand. Spectra data are available in Foster and others (2023).

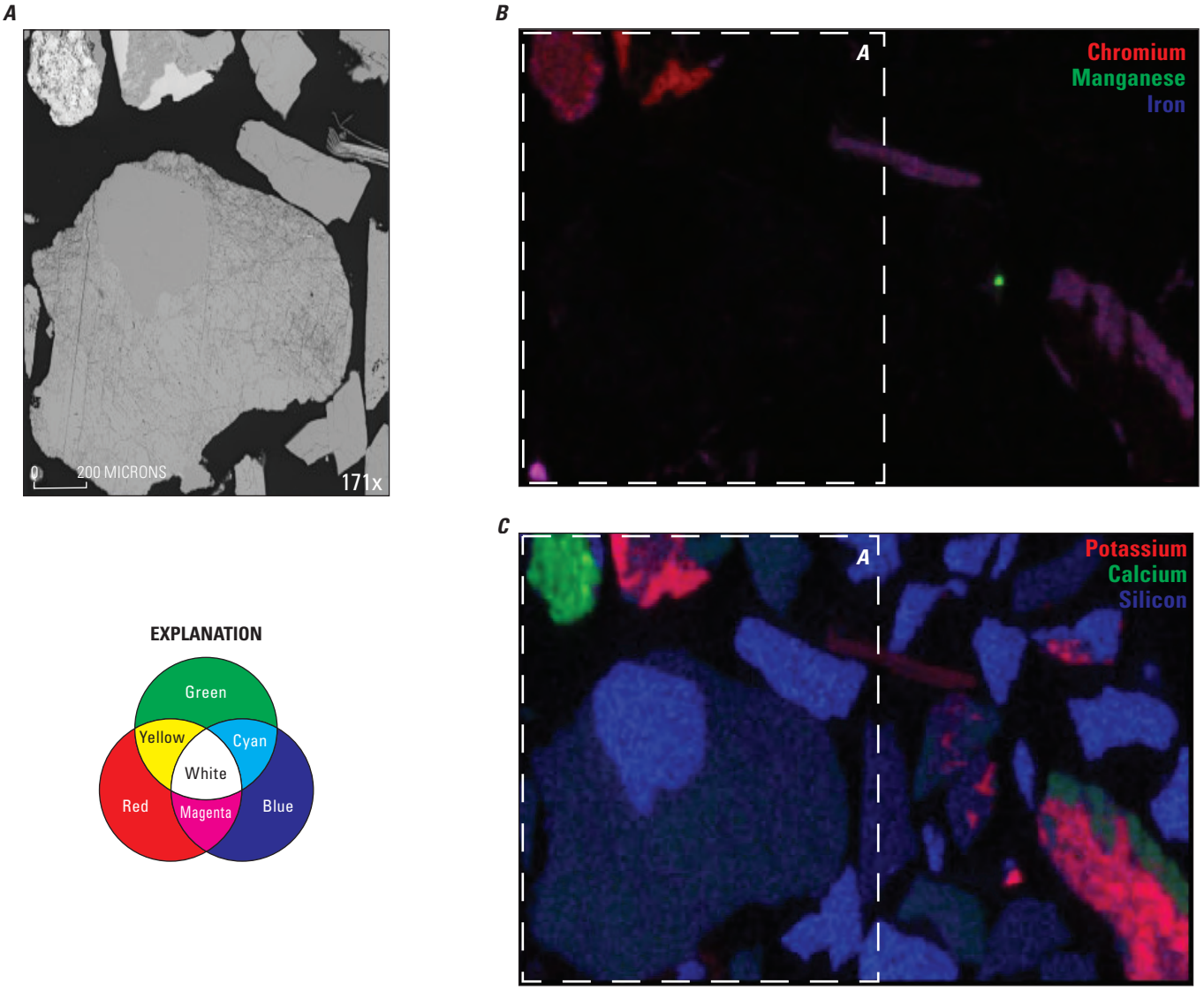

Figure I.20. *A*, shows backscatter electron-scanning electron microscopy (BSE-SEM) image of site BG-0005 material after 1.25 years of reduction (day 0 of the oxidation experiment) compared with synchrotron micro-X-ray fluorescence (μXRF) tricolor maps showing distribution of *B*, chromium (Cr), manganese (Mn), and iron (Fe); and *C*, potassium (K), calcium (Ca), and silicon (Si). Scales of *B* and *C* are the same as the scale of *A*; white-dashed boxes in *B* and *C* show the imaged area in *A*. Maps and images were collected from epoxy-mounted grains prepared as a standard 30-micrometer (μm) thick petrographic section. The 45-degree orientation of the sample with respect to the detector causes slight distortion of *B* and *C*. Data are available in Foster and others (2023).

Elevated concentrations of Cr, Mn, and Fe were observed after reduction of these concentrations at SA-SB-01. Backscattered bright spots (in areas circled on fig. I.21*A*) were associated with the edges of mineral grains and with on-edge clay particles. Where Cr was found, it was co-located with Fe (magenta; fig. I.21*B*). In contrast to analysis of SEM-EDS data from BG-0004 and BG-0005, manganese existed in isolation (green), perhaps as a silicate or carbonate (fig. I.21*B*). Plotting smoothed Cr and Fe counts (fig. I.21*C*) allowed for masking of the dominant Cr/Fe pattern, which was likely an artifact of the very high Fe counts relative to Cr. The secondary pattern (outlined by red box) was used to create the map on figure I.21*B*.

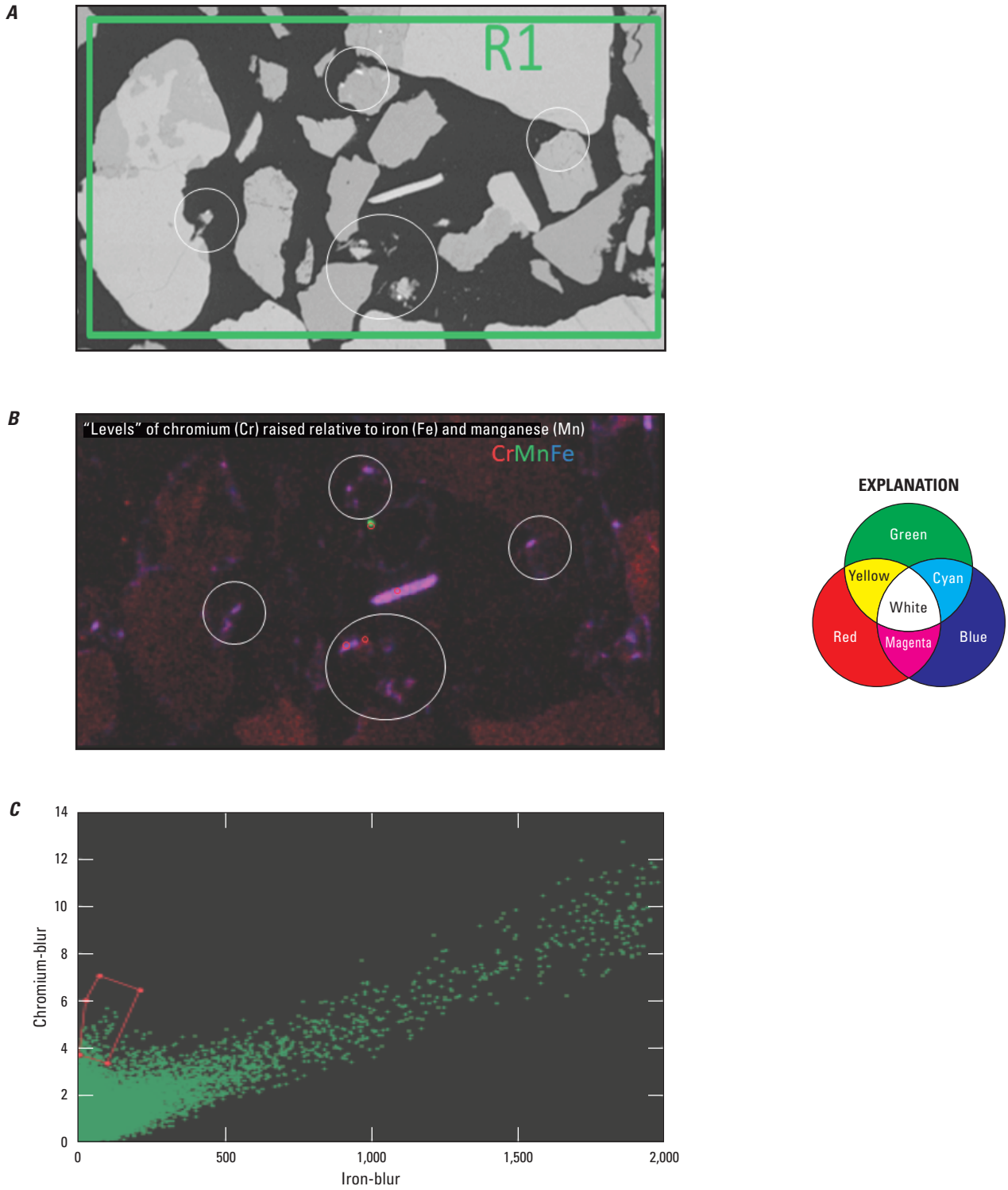

Figure I.21. *A*, Backscatter electron (BSE) image of site SA-SB-01 material after 1.25 years of reduction (day 0 of the oxidation experiment) compared with *B*, synchrotron micro-X-ray fluorescence (μXRF) tricolor maps of the same grains showing distribution of chromium, manganese, and iron (Cr-Mn-Fe). Maps and images were collected from epoxy-mounted grains prepared as a standard 30-micrometer (μm) thick petrographic section. The 45-degree orientation of the sample with respect to the detector causes slight distortions of the image in *B*. Small red circles on image *B* are not Cr hotspots—they indicate locations where micro-X-ray absorption near edge structure (μXANES) spectra were collected. *C*, Scatterplot of smoothed (blur) Cr and Fe μXRF counts from the map in *B* show a strong correlation between Cr and Fe and a near-constant ratio for most points; however, a minor but distinctly different Cr-Fe relation also is present as indicated by the red box. Data are available in Foster and others (2023).

Manganese XANES data also demonstrated a change in oxidation state of Mn with progress of reduction. Bulk spectra showed growth of the manganese(II), Mn(II), peak and a decrease in oxidized peaks from the precursor and the start of reduction (0 days) to 350 days of reduction in BG-0004 (fig. I.22*A*). First derivatives emphasize the change in slope of the XANES spectra (fig. I.22*B*). All three sites contained a mix of Mn oxidation states. Manganese(IV), Mn(IV), was less well defined in precursor BG-0005 and SA-SB-01 than in BG-0004. The spectrum of material from site PZ-07 (used in this study to represent highly oxidized material; see chapter C for additional detail) showed a predominance of oxidized Mn(IV).

A regular pattern of the effect of reduction was observed when comparing bulk Mn XANES spectra (figs. I.23*A–B*) from BG-0004 and BG-0005 collected at 41 days of reduction (T1) and 720 days of reduction (T5). Oxidized Mn(IV) peaks decreased with time in both sites but decreased with time more in BG-0004 than in BG-0005. Site BG-0005 may have lost some Mn(II) to the aqueous phase during reduction, but BG-0004 did not lose any Mn(II). Bulk Fe XANES spectra of both sites were nearly identical at 41 and 720 days of reduction (figs. I.23*C* and I.23*D*, respectively). However, Fe EXAFS spectra (insets on figs. I.23*C–D*) indicate that changes had occurred to local coordination of Fe.

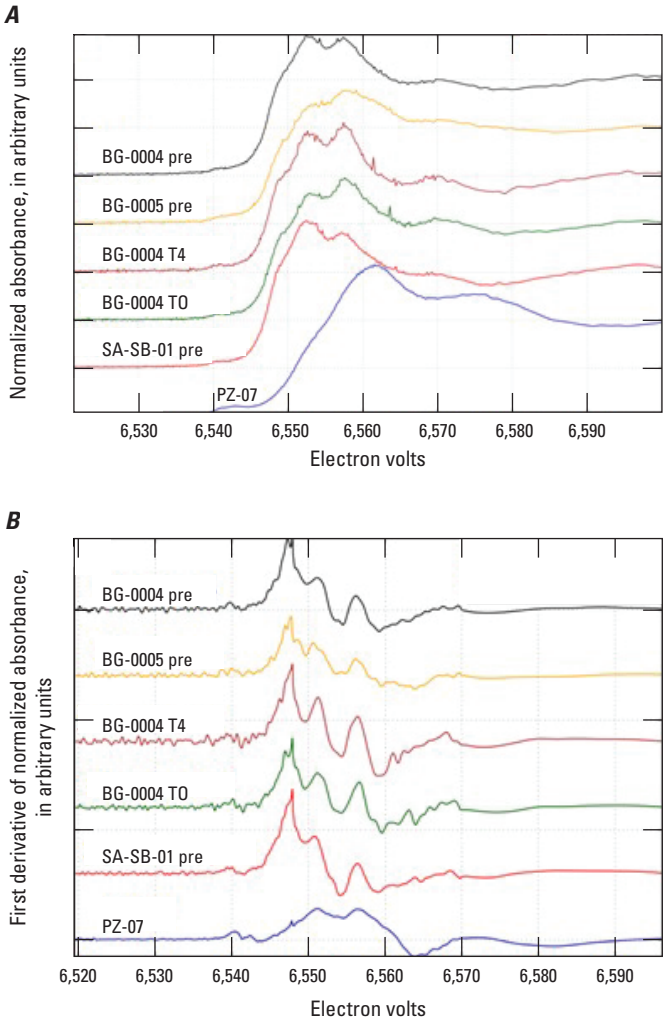

Figure I.22. Bulk manganese X-ray absorption near edge spectra (Mn XANES) *A*, of precursor materials (sites BG-0004, BG-0005, and SA-SB-01), PZ-07 material (see chapter C) as well as reduction samples collected at 0 days (T0) and 350 days (T4) for site BG-0004. Strong rightward shift of PZ-07 spectrum and distinct line shape indicates a predominance of Mn(IV), likely manganese oxide. First derivatives of spectra are shown in *B*, highlighting Mn(II), Mn(III), and Mn(IV) as distinct peaks from left to right. Spectra data are available in Foster and others (2023).

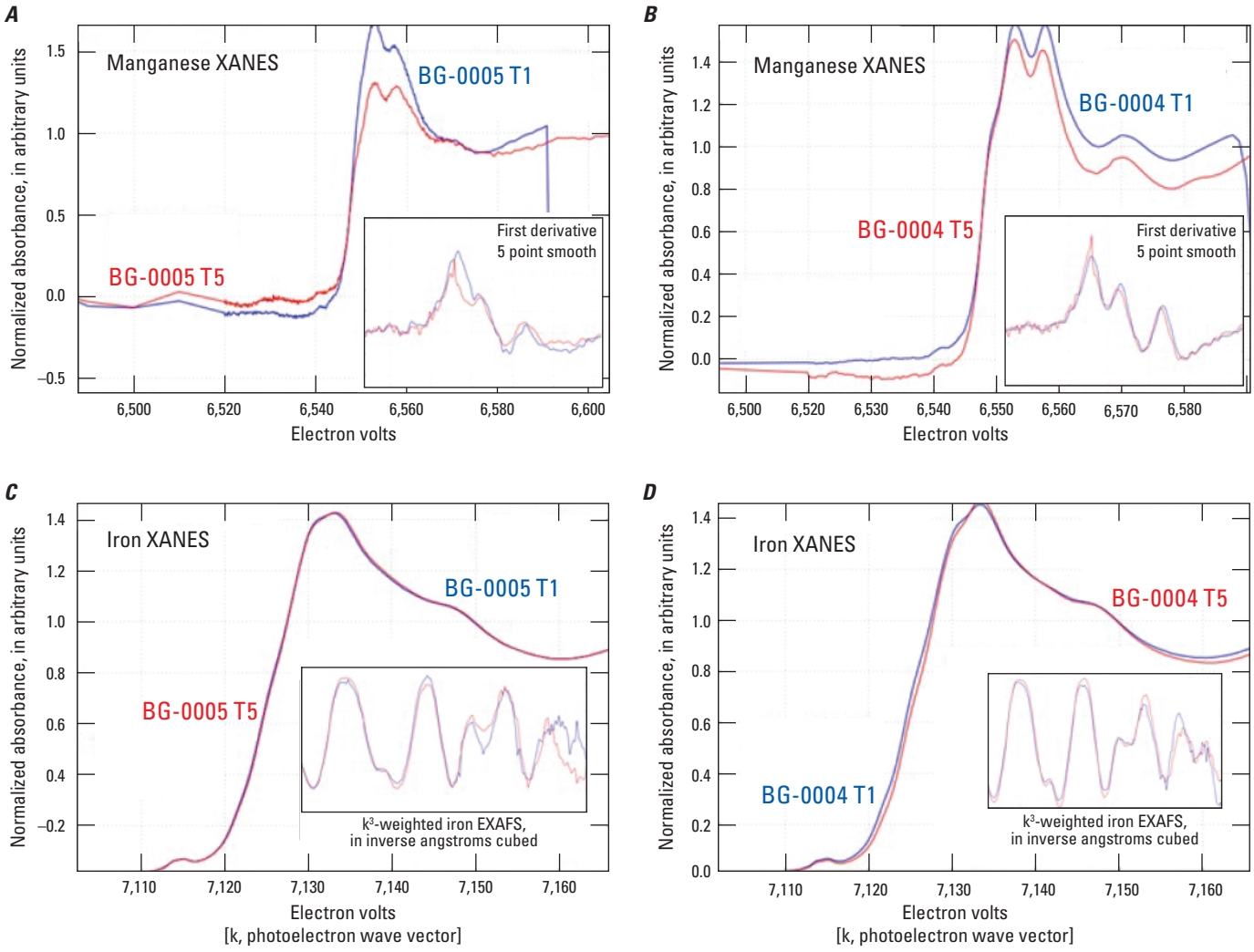

Figure I.23. Bulk manganese X-ray absorption near edge spectra (Mn XANES) and corresponding first derivatives (insets) of *A*, site BG-0005 reduction samples and *B*, site BG-0004 reduction samples. Bulk iron X-ray absorption near edge spectra (Fe XANES) and corresponding extended X-ray absorption fine structure (EXAFS, insets) are shown for 41 (T1) and 720 (T5) days of reduction for *C*, site BG-0005 and *D*, site BG-0004. Data are available in Foster and others (2023).

I.3.4. Oxidation Experiment

Groundwater sampled from wells MW-77S and BG-0004A (table I.2) is naturally oxic and alkaline (table I.2; chapter E, appendix E.1, table E.1.1). Chromium that was previously reduced by treatment within the IRZ or natural processes may oxidize from Cr(III) back to Cr(VI) and enter groundwater if hydrogeochemical conditions change and groundwater in the IRZ becomes oxic.

The potential for such release was evaluated by oxidizing previously reduced microcosms containing samples amended to 3,000 ng Cr/g of material (the same amount in the reduction experiment). The method distinguished Cr(VI) associated with aqueous (dissolved) and solid (sorbed) phases in the microcosms. Aqueous Cr(VI) is considered released, whereas Cr(VI) sorbed to mineral grains is considered available to be released. During the oxidation experiment, all materials released small amounts of Cr(VI) over time. However, after 365 and 679 days, the amount of soluble and surface-bound Cr(VI) decreased. The amount of Cr(VI) released and available for release and its distribution between aqueous and solid phases varied by sample type; hence site materials, pure Fe- and Mn-coated sand end members and mixtures of Fe- and Mn-coated sand are plotted and discussed separately.

I.3.4.1. Oxidation of Site Materials

Some Cr(VI) was produced and released during the nearly 2 years of oxidation imposed on previously reduced material from BG-0004 (fig. I.24*A*). Aqueous Cr(VI) values were frequently noted above the reporting level of 15 ng/g of material; however, mean aqueous values remained below 30 ng/g. Aqueous pH values ranged from 5.6 to 8.4. (As previously discussed it was not pH controlled within the microcosms using organic buffers, as these buffers altered the redox status of the microcosms.) By contrast, solid-phase Cr(VI) values rose in BG-0004 materials from an initial value of 56 ng/g (below the reporting level) to 285±87 ng/g (about twice the reporting level) at 285 days and then decreased to 111±31 ng/g by 679 days. These data indicate that some Cr(VI) is available for release during reoxidation of treated aquifer materials that are similar in texture and composition to the Recent Mojave River materials that are the most common materials present within the IRZ in Hinkley Valley (Miller and others, 2018).

Older Mojave River deposits (characterized by BG-0005) also comprise a significant portion of the IRZ materials (Miller and others, 2018), and there is greater potential for Cr(VI) release to occur upon reoxidation of these materials (fig. I.24*B*). Mean aqueous Cr(VI) values were generally low during 2 years of reoxidation of BG-0005 materials, with peak values of 60 ng/g initially (four times the reporting level) and 43±32 ng/g at 679 days. Aqueous pH values ranged from 5.6 to 8.6; however, solid-phase Cr(VI) values increased to more than 636 ng/g of material during the first 285 days of oxidation, indicating potential for Cr(VI) to be released from older Mojave River materials. Potential for release was noted at the 14-, 56-, 125-, and 285-day oxidation timepoints. Extractable (sorbed) Cr(VI) decreased by more than five times during the final two oxidation timepoints (365 and 679 days).

Site SA-SB-01 represents material previously treated with ethanol from within the IRZ. Materials from this location and depth were exposed to elevated levels of Cr(VI) for decades and were reduced in situ for several years before collection. Site SA-SB-01 materials remained anoxic during processing and were additionally subjected to the same 1-year reduction protocol applied to other samples, except incubations began under anoxic conditions. Monitoring of mineralization of the Cr(VI) that was added to SA-SB-01 microcosms was not done, as it was done with other site materials during the preliminary experiment; however, it is assumed that added Cr(VI) was similarly reduced as in BG-0004 and BG-0005, probably faster. Production of methane (CH_4) in nearly half the microcosms late in the reduction period indicated that reduction was extensive (data not shown). Consistent with other site materials, none of the added Cr(VI) remained in the aqueous phase of SA-SB-01 microcosms at the end of the 1.25±0.2 years reduction (T=0 of the oxidation experiment; fig. I.24*C*). Mean aqueous Cr(VI) values remained at or below the reporting level until 285 days oxidation at which time Cr(VI) increased to 60 ng/g of material (a four times increase). After 679 days of oxidation, mean aqueous Cr(VI) values were 78±14 ng/g of material. Aqueous pH values ranged from 7.3 to 9.2. Extractable Cr(VI) values were below the reporting level at T=0 and increased to the reporting level (150 ng/g of material) during the first 56 days of oxidation. Subsequently, mean extractable Cr(VI) increased to more than 300 ng/g of material during several timepoints before decreasing to below the reporting level at 365 and 679 days.

Similar to site materials from BG-0004 and BG-0005, Cr(VI) measured through time in the aqueous phase and in alkaline extractions indicates the potential for release of Cr(VI) from previously reduced IRZ materials that may be subjected to reoxidation resulting from changes in hydrologic regime. Additional Cr(III) present in SA-SB-01 as a result of prior bioremediation did not appear to result in greater reoxidation of Cr (III) to Cr(VI) from these materials.

I.3.4.2. Oxidation of Artificial Substrates

A similar pattern of Cr(VI) release during oxidation was observed for the pure end-member Fe- and Mn-coated sand as was observed in aquifer materials. Mean aqueous Cr(VI) values were consistently low (below 30 ng/g of material) during oxidation of microcosms containing reduced Fe sand (fig. I.25*A*). Aqueous pH values ranged from 6.4 to 8.3 and were similar to those measured in water from well BG-0004A. However, solid Cr(VI) values were initially elevated (above 200 ng/g of material) and increased further from 300 to 400 ng/g of material during the period from 125 to 285 days of oxidation. Manganese was present within the Fe-coated sand at low concentrations, only occasionally approaching 0.2 percent by weight, and oxidation of Cr(III) to Cr(VI) presumably occurred solely in the presence of dissolved oxygen. Subsequently, solid Fe sand Cr(VI) values decreased to below the reporting level (less than 150 ng/g) at 365 and 679 days.

Values for aqueous Cr(VI) of Mn sand were generally low (fig. I.25*B*) during oxidation; however, there was substantially more aqueous Cr(VI) present at 14 and 56 days (125 ng/g of material) than at later timesteps. Aqueous values declined with further oxidation to 20 ng/g of material (slightly above the reporting level) after 56 days and remained low throughout the study. Aqueous pH values of Mn sand (range 6.6–8.5 on fig. I.25*B*) were slightly higher than aqueous pH values of Fe sand (range 6.4–8.3 on fig. I.25*A*). As with Fe sand, mean solid Cr(VI) values in the Mn sand samples were elevated initially, notably increasing above 700 ng/g of material by 125 and 285 days. These were among the highest values obtained for potential Cr(VI) release during reoxidation. Samples at 365 and 679 days had substantially lower solid Cr(VI) values.

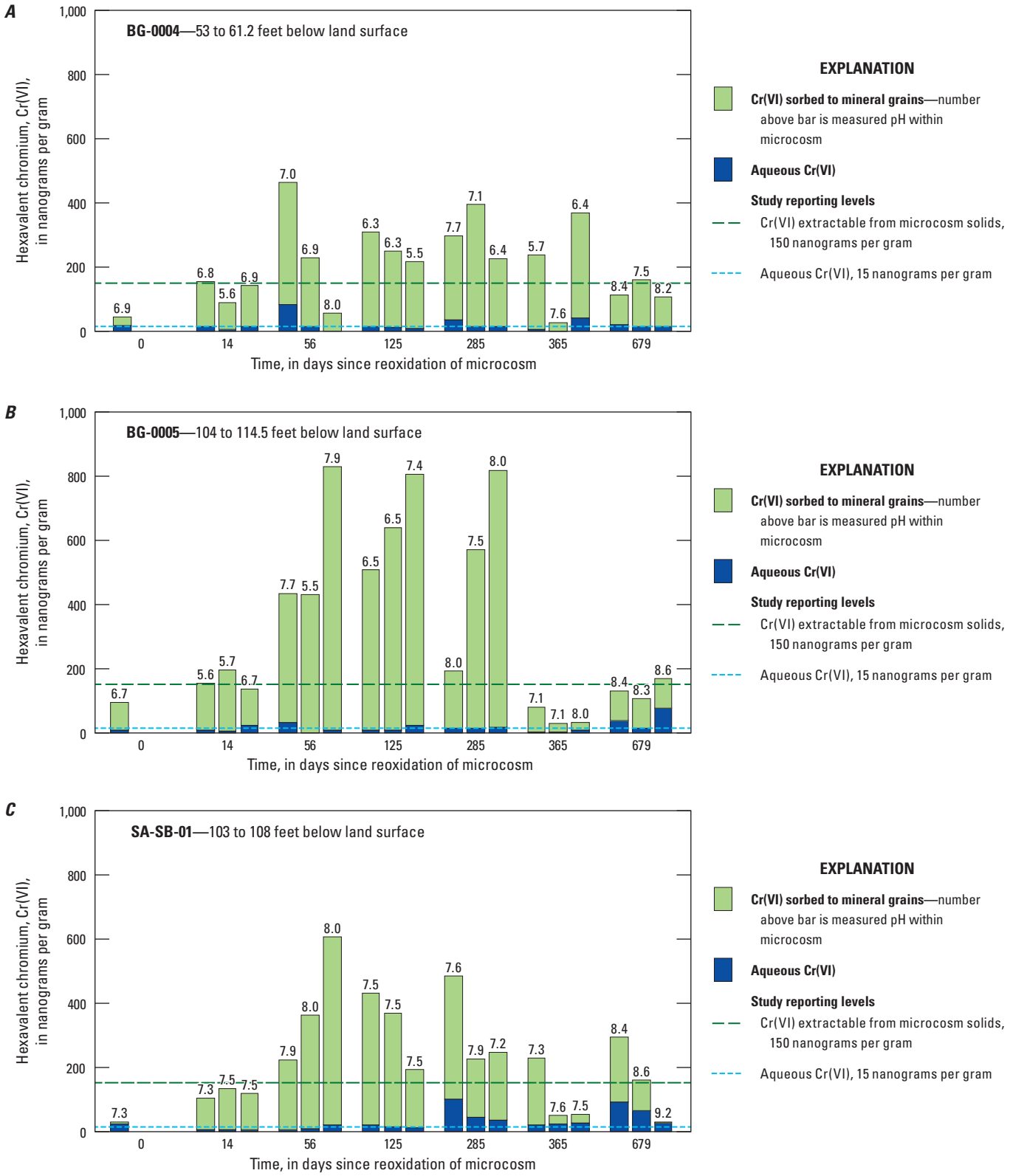

Figure I.24. Hexavalent chromium, Cr(VI), recovered at selected times during 2 years of reoxidation of site materials at *A*, BG-0004, *B*, BG-0005, and *C*, SA-SB-01, which were previously reduced for more than 1 year in the presence of 3,000 nanograms per gram (ng/g) added Cr(VI). Numbers above the bars indicate the pH of the aqueous phase at the time of sampling. Blue bars represent individual analyses of aqueous Cr(VI) at the time of separation from the solid phase. Blue-dashed lines represent the aqueous Cr(VI) reporting level. Green bars represent individual analyses of the amount of Cr(VI) released following alkaline digestion of the solid phase. Green-dashed lines represent the solid-phase Cr(VI) reporting level. Data are available in Miller and others (2020b).

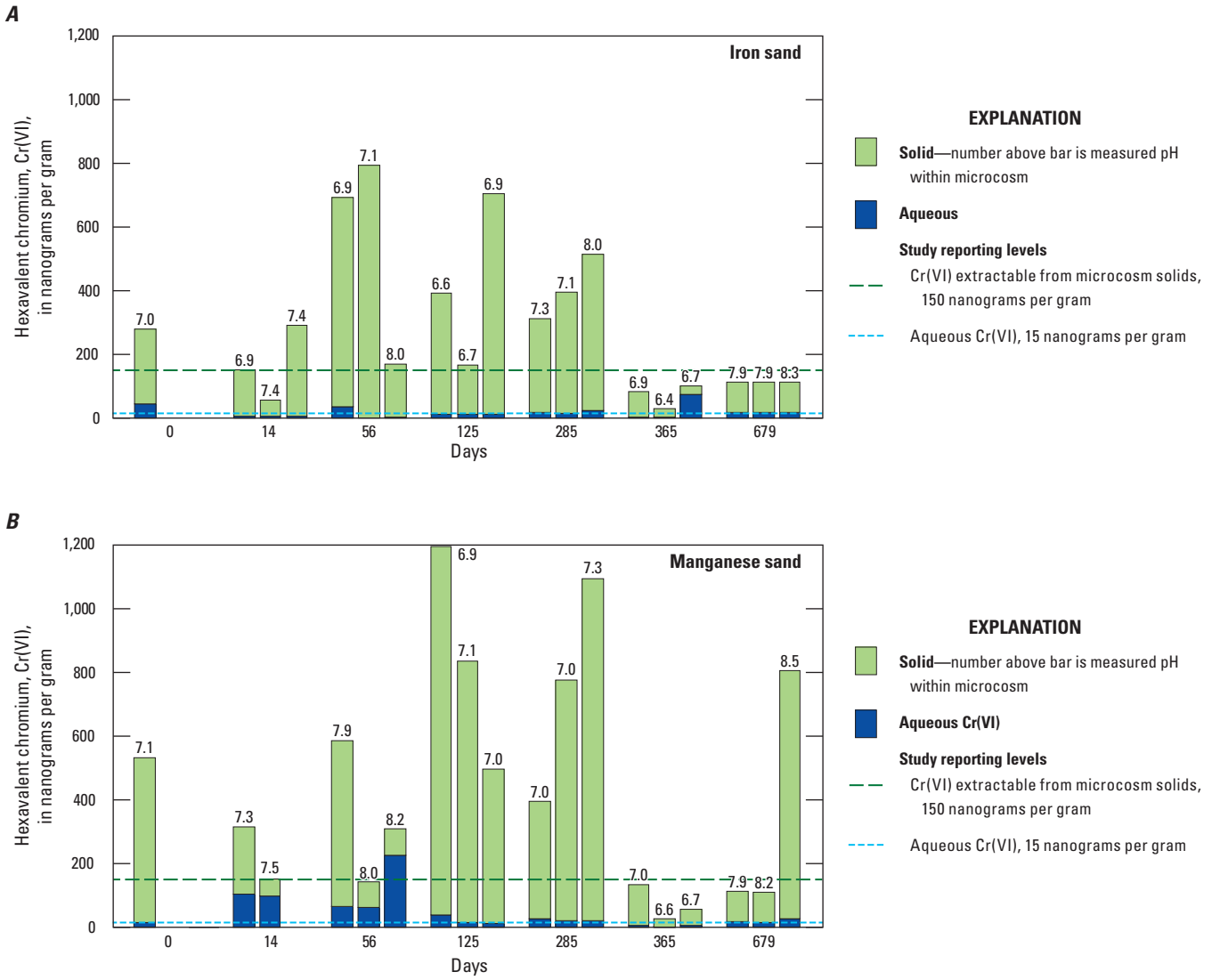

Figure I.25. Hexavalent chromium, Cr(VI), recovered at selected times during 2 years of reoxidation of *A*, iron (Fe) sand and *B*, manganese (Mn) sand, which were previously reduced for more than 1 year in the presence of 3,000 nanograms per gram (ng/g) added Cr(VI). Numbers above the bars indicate the pH of the aqueous phase at the time of sampling. Blue bars represent individual analyses of aqueous Cr(VI) at the time of separation from the solid phase. Blue-dashed lines represent the aqueous Cr(VI) reporting level. Green bars represent individual analyses of the amount of Cr(VI) released following alkaline digestion of the solid phase. Green-dashed lines represent the solid-phase Cr(VI) reporting level. Data are available in Miller and others (2020b).

Aqueous Cr(VI) was elevated in some early oxidation measurements of microcosms containing mixtures of Fe sand and Mn sand. Aqueous pH values ranged from 6.8 to 8.2 (fig. I.26*A*). The highest mean aqueous Cr(VI) values (over 500 ng/g of material) were observed after 14 days oxidation in microcosms containing Fe/Mn 100 (fig. I.26*A*). Aqueous Cr(VI) levels were lower after further oxidation. Other mixtures (Fe/Mn 50 and Fe/Mn 25; figs. I.26*B*–*C*) yielded variable, but generally low, levels of aqueous Cr(VI). Values above the solid-phase reporting level for Cr(VI) occurred in all Fe/Mn-coated sand mixtures, with the maximum values occurring in the middle of the oxidation period (125 and 285 days). A mean value of 800 ng/g Cr(VI) was recovered following 125 days of oxidation of microcosms containing Fe/Mn 25. These samples had the highest Mn content of the artificial substrate mixtures, and the effect of Mn on the amount of Cr(VI) available for release was comparable to pure Mn sand.

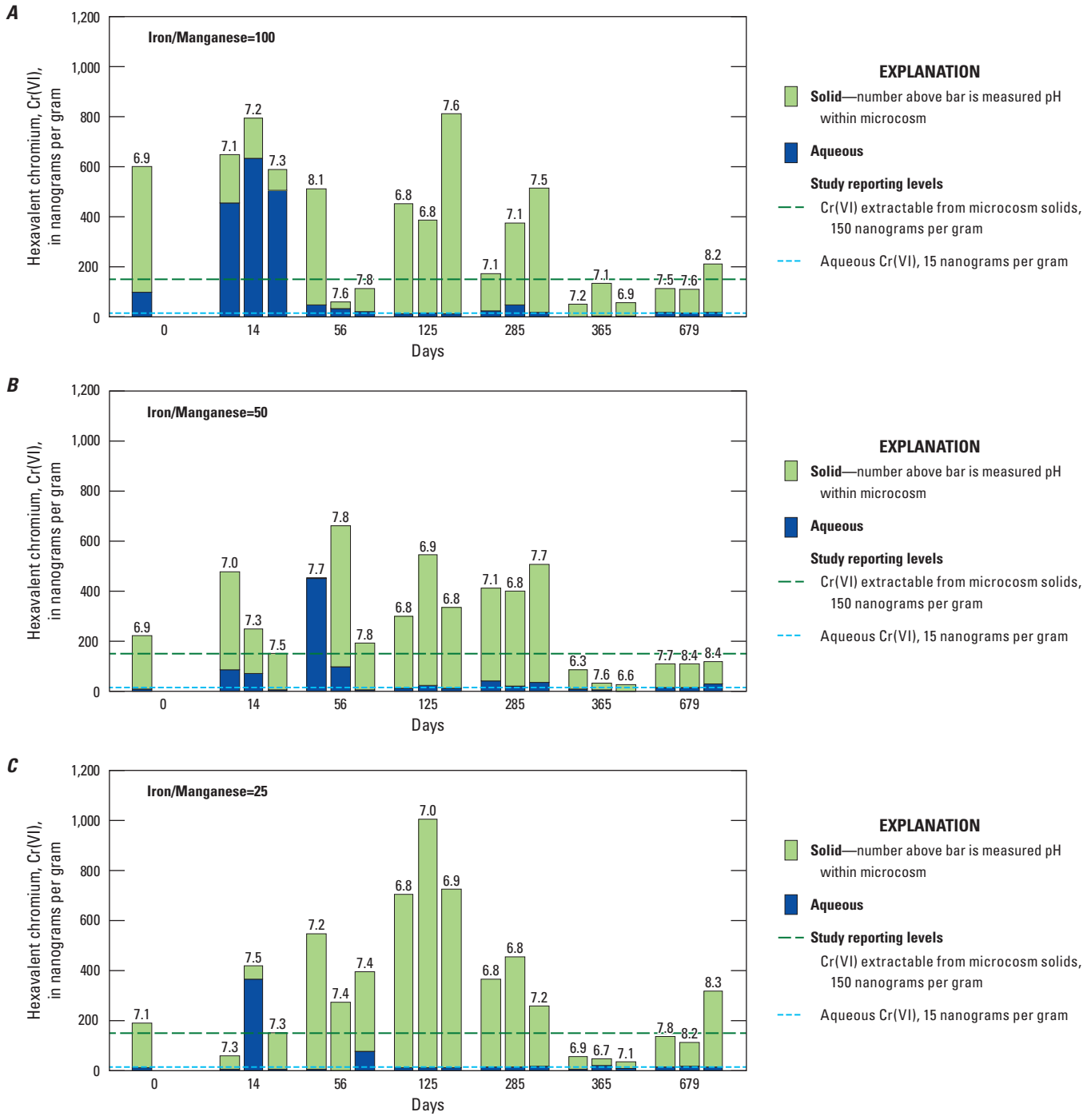

Figure I.26. Hexavalent chromium, Cr(VI), recovered at selected times during 2 years of reoxidation of mixtures of iron-coated (Fe) sand and manganese-coated (Mn) sand (*A*, Fe/Mn 100, *B*, Fe/Mn 50, and *C*, Fe/Mn 25), which were previously reduced for more than 1 year in the presence of 3,000 nanograms per gram (ng/g) added Cr(VI). Numbers above the bars indicate the pH of the aqueous phase at the time of sampling. Blue bars represent individual analyses of aqueous Cr(VI) at the time of separation from the solid phase. Blue-dashed lines represent the aqueous Cr(VI) reporting level. Green bars represent individual analyses of the amount of Cr(VI) released following alkaline digestion of the solid phase. Green-dashed lines represent the solid-phase Cr(VI) reporting level. Data are available in Miller and others (2020b).

I.3.4.3. Evolution of Solid Phases During Oxidation

Microcosms containing site materials or artificial substrates were fully reduced at the onset of the oxidation experiment. Redox state and biogeochemical conditions were stable after 1.25±0.2 years reduction (see results from section "I.2.2 Reduction Experiments"). Oxidation resulted in profound changes to solid-phase characteristics within weeks (14 days) to months (56 and 125 days). However, some characteristics were initially resistant to change. For example, after 14 days of exposure to air in SA-SB-01, sulfide grains in reduced clays (spectrum 109) remained armored to the oxidative changes occurring elsewhere in the solid matrix by thick coatings of reduced material (figs. I.27*A–B*).

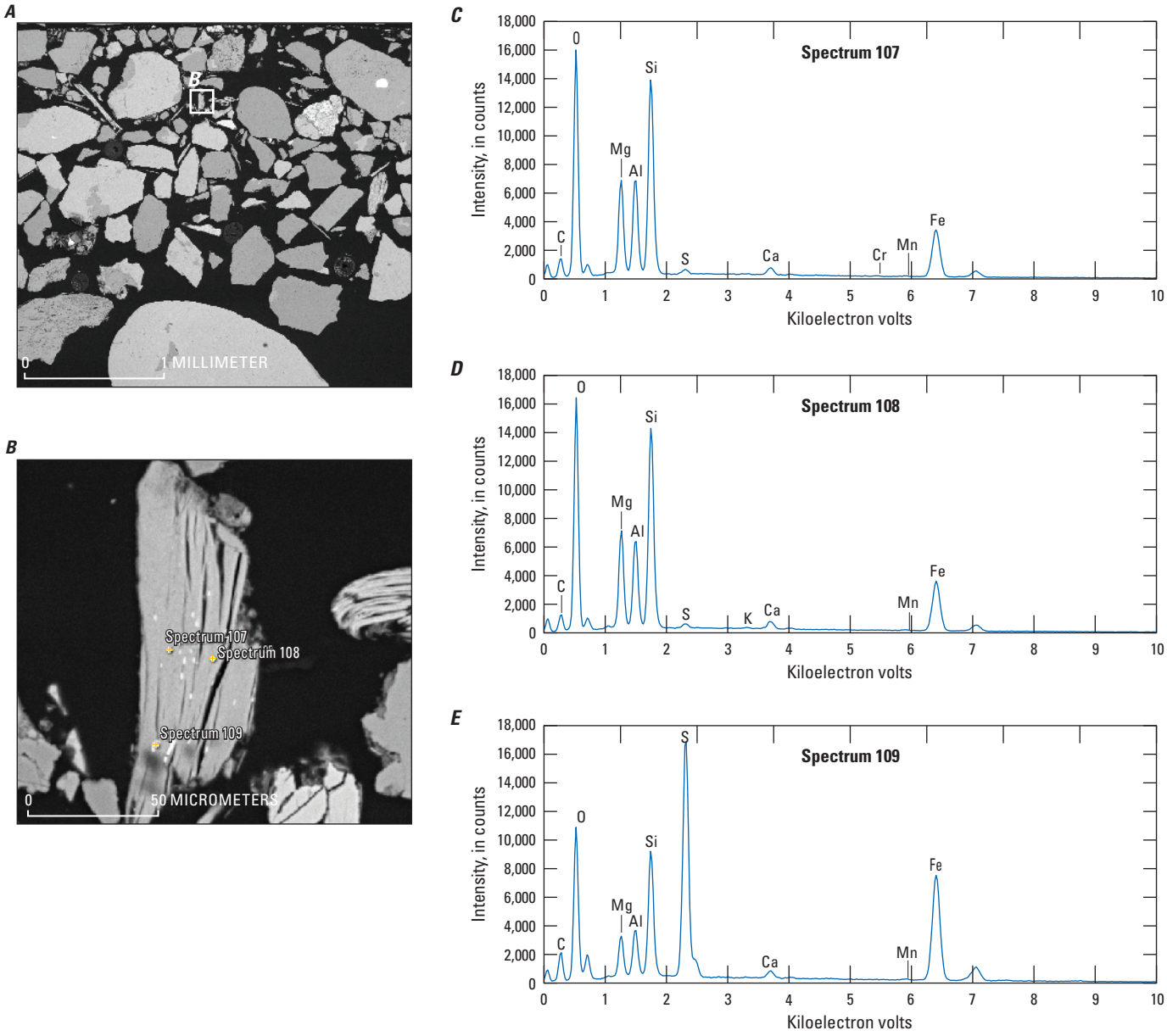

Figure I.27. Backscatter photomicrograph showing a thin section of SA-SB-01 in *A*, a large area; and *B*, in a location close up after 14 days of oxidation; spectra are shown in *C*, spectra 107; *D*, spectra 108; and *E*, spectra 109. Small grains of sulfide presumably formed during reduction are still visible in a grain with morphology and composition consistent with an iron-rich aluminosilicate clay (see table I.6 for compositions). Data are available in Foster and others (2023). [Al, aluminum; C, carbon; Ca, calcium; Cr, chromium; Fe, iron; K, potassium; Mg, magnesium; Mn, manganese; O, oxygen; S, sulfur; Si, silicon]

Optical microscopic analysis of polished petrographic thin sections revealed the presence of coatings on individual grains of artificial substrates at the onset of oxidation. Dark-brown and orange-brown particles were in a grayish-tan coating on grain edges but were rarely found inside quartz grains. As oxidation progressed, for example in Fe/Mn 50 (fig. I.28), the coating grew in thickness, from a median value of 12 µm (fig. I.28*A*) to as much as 34 µm after 125 days (fig. I.28*D*). Optical examination suggests that oxide coatings on native mineral grains can be as much as 20 µm thick, although generally they are less than 5 µm thick to indistinguishable on most grains (chapter C).Visually, the density of dark particles in the coating fluctuated as well. The grayish-tan coating thickness appeared to reach a maximum at 125 days of oxidation (fig. I.28*D*). The coating was observed to fill cracks with origin in grain exterior and completely infill surface topographic embayments. It is possible that, similar to sulfide grains discussed previously (fig. I.27*A*), after time these coatings armor chromium containing surface coatings produced during reduction, protecting them from oxidation during the later timesteps of the experiment.

Figure I.29 demonstrates the general pattern of increasing coating thickness during early oxidation for several end member samples. Iron sand (fig. I.29*A*) and Mn sand (fig. I.29*B*) had similar coating thickness when first manufactured (precursors) and after 1.25±0.2 years reduction (0 days of oxidation). Coating thickness increased in Fe sand and Mn-coated sand end members for 14 days and remained elevated for 9 months (285 days). Coating thickness also increased in Fe/Mn 50 by 14 days (fig. I.29*C*), decreased at 56 days, and returned to elevated levels thereafter. Samples from later in the oxidation period (365 and 679 days) had thin to non-existent coatings (data not shown). The particles in the coatings are the secondary Fe and Mn phases of primary interest to this study. In 2022, a relation between the density of secondary Fe and Mn hydroxides on particle edges in optical images and the thickness variation of the grayish-tan coatings, was not obtained.

Images of the same grains on thin sections made from samples of Fe sand at 14 days of oxidation and Mn sand at 56 days of oxidation were collected using optical microscopy and BSE microscopy (fig. I.30). More dark particles of Fe and Mn hydroxides are present in the optical image than in the corresponding BSE image, because the transparent nature of the quartz grains allows observation of particles down to indeterminate depths below the surface, whereas BSE images are extremely surface sensitive (only showing features within approximately 1–5 micrometers of the sample surface due to limited penetration/interaction depth of the electron beam). That most of the observable precipitate on figures I.30*A* and I.30*C* is not visible during BSE imaging indicates that most of the precipitate is below the surface and not available for SEM-EDS analysis. A notable exception is shown on figures I.30*C* and I.30*D* (see white arrows), where a particularly dense (or particularly dark) mass of precipitate has been preserved at the actual surface of the thin section.

The origin of the grayish-tan coatings in which precipitates appear associated was not made clear by comparing optical and BSE images of the same grains. The coatings appear invisible in the BSE image because the outer edge of the grains in the BSE images encompass the grayish-tan coating (if careful comparison to the corresponding optical image is made).

The BSE maps of hundreds of grains were examined in the thin sections of oxidation experiment samples to find locations where surface coatings were preserved and available for SEM-EDS analysis. For example, particles in attached and detached coatings from Fe/Mn 25 at 56 days of oxidation (fig. I.31) were clearly visible in thin sections under optical (fig I.31*A*) and backscattered (fig. I.31*B*) conditions. Close-up images (figs. I.31*C–F*) of two areas show that coatings consist of blocky Mn-rich (green) and Fe-rich (blue) grains of various shapes and sizes held together within a cementing fabric of another Fe-rich phase. Multi-element area maps and point spectra were used to create tricolor images (figs. I.31*G–H*) that show the Mn-rich phases surrounded by the Fe-rich phases but also indicate that segregation of Fe-rich and Mn-rich phases exists in this sample and was observed in all mixtures of Fe and Mn sands analyzed. Chromium was detected in tricolor images in a few instances but was not generally discernable in these images; chromium was more often quantified by spectral collections over areas encompassing a single grain.

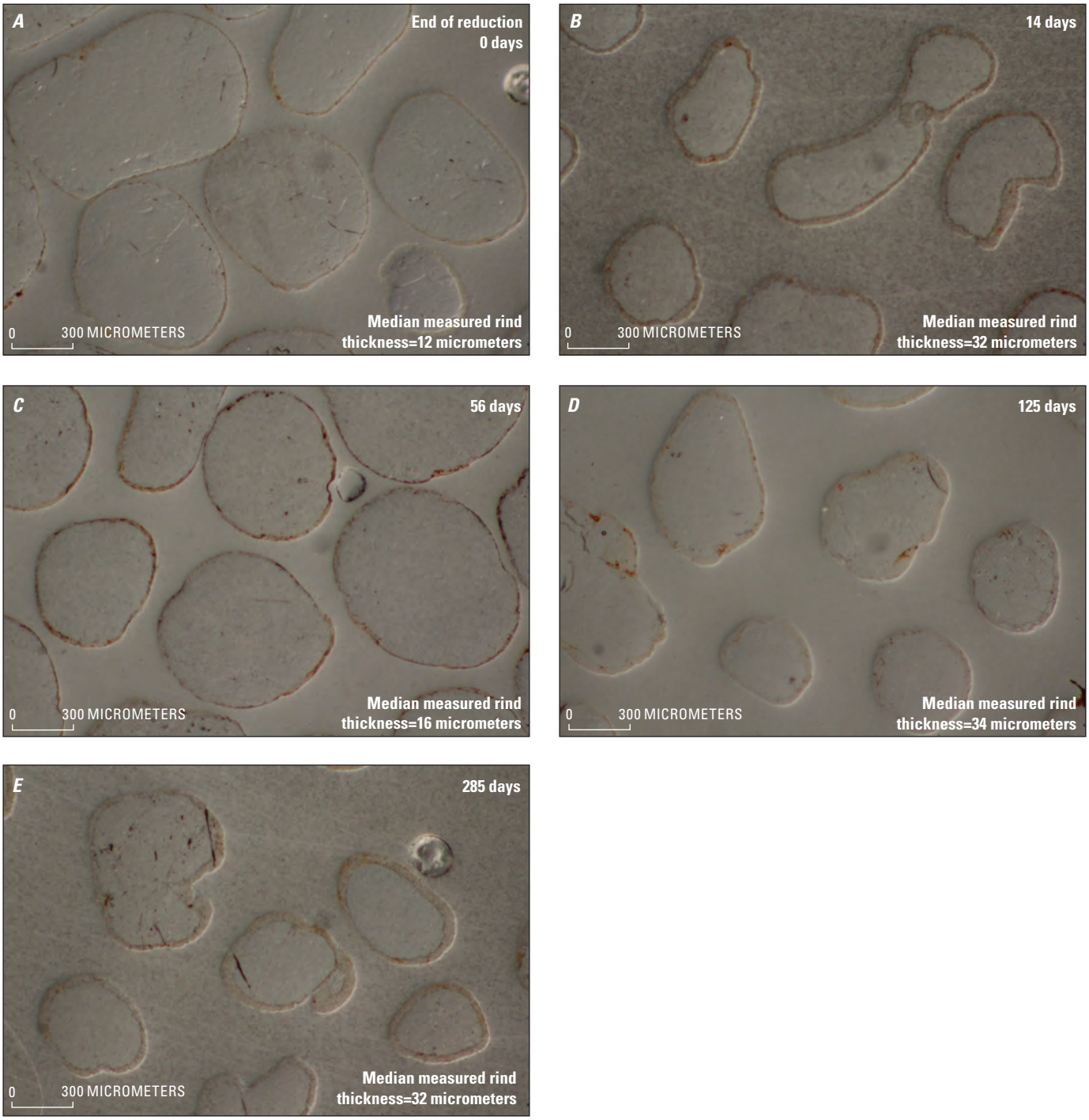

Figure I.28. Optical images of petrographic sections showing the progression of coatings on sand samples in which the ratio of iron (Fe) to manganese (Mn) in coated sand is equal to 50 (Fe/Mn 50); images show the progression of grayish-tan coatings on sand grains and their relation to Fe and Mn particles during the first 285 days of oxidation (*A*, 0 days; *B*, 14 days; *C*, 56 days; *D*, 125 days; and *E*, 285 days). Carbon coating of slides in *B* and *E* resulted in a speckled background. Data are available in Foster and others (2023).

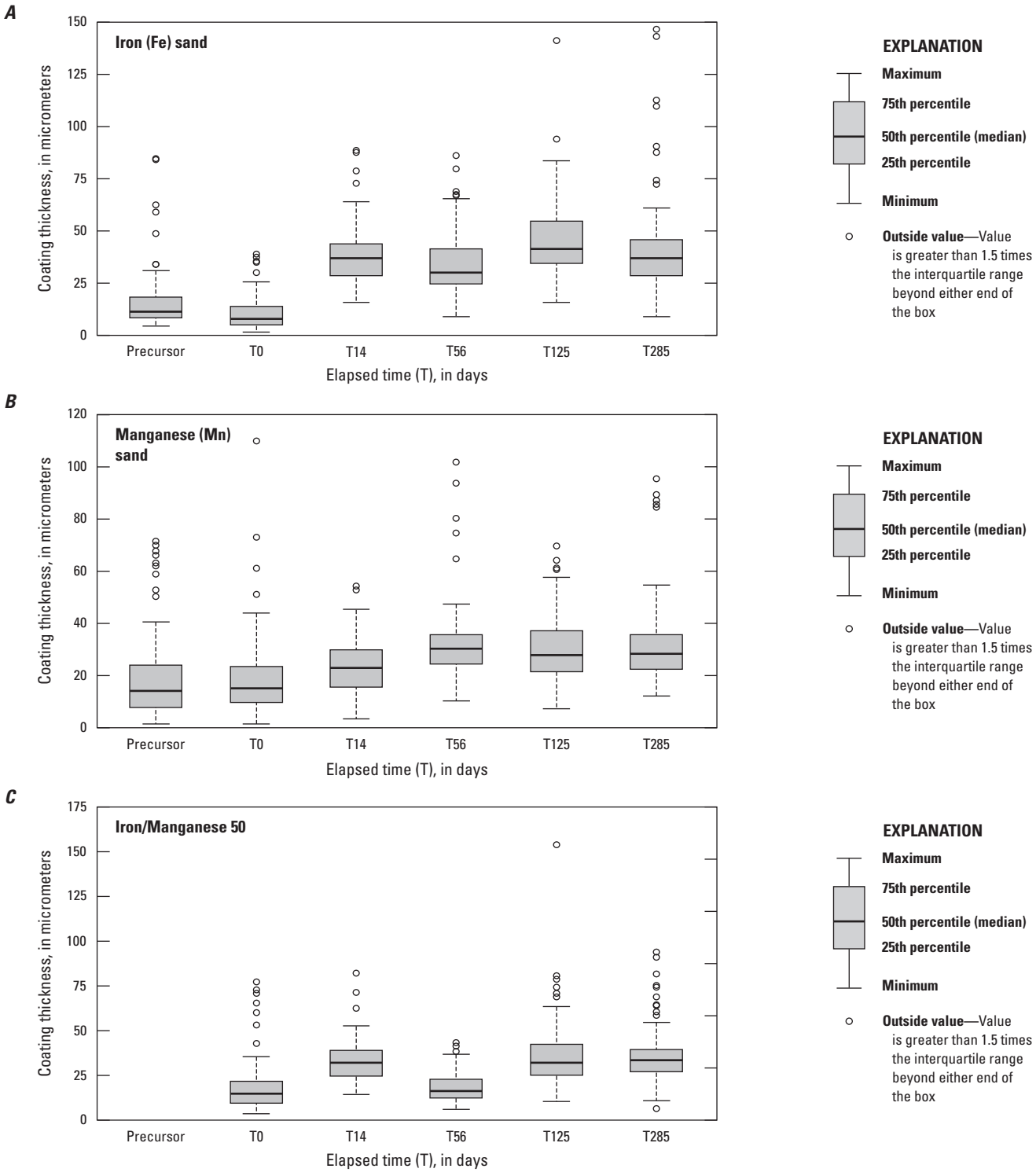

Figure I.29. Boxplots summarizing variation in thickness of grayish-tan coatings on *A*, iron-coated (Fe) sand, *B*, manganese-coated (Mn) sand, and *C*, Fe/Mn 50 during the oxidation experiment (table I.1) as measured from optical images of timepoint samples (precursor, 0 days, 14 days, 56 days, 125 days, and 285 days of oxidation). The thick, dark bar in each box represents the median measurements of more than 25 grains, the upper and lower edges of the box are the first and third quartile values (respectively). The lower and upper horizontal lines indicate the minimum and maximum values. Outliers (greater than or less than 1.5 times the interquartile range) are indicated separately as open circles. Note the different vertical scale for Mn sand and the absence of precursor values for Fe/Mn 50. Data are available in Foster and others (2023).

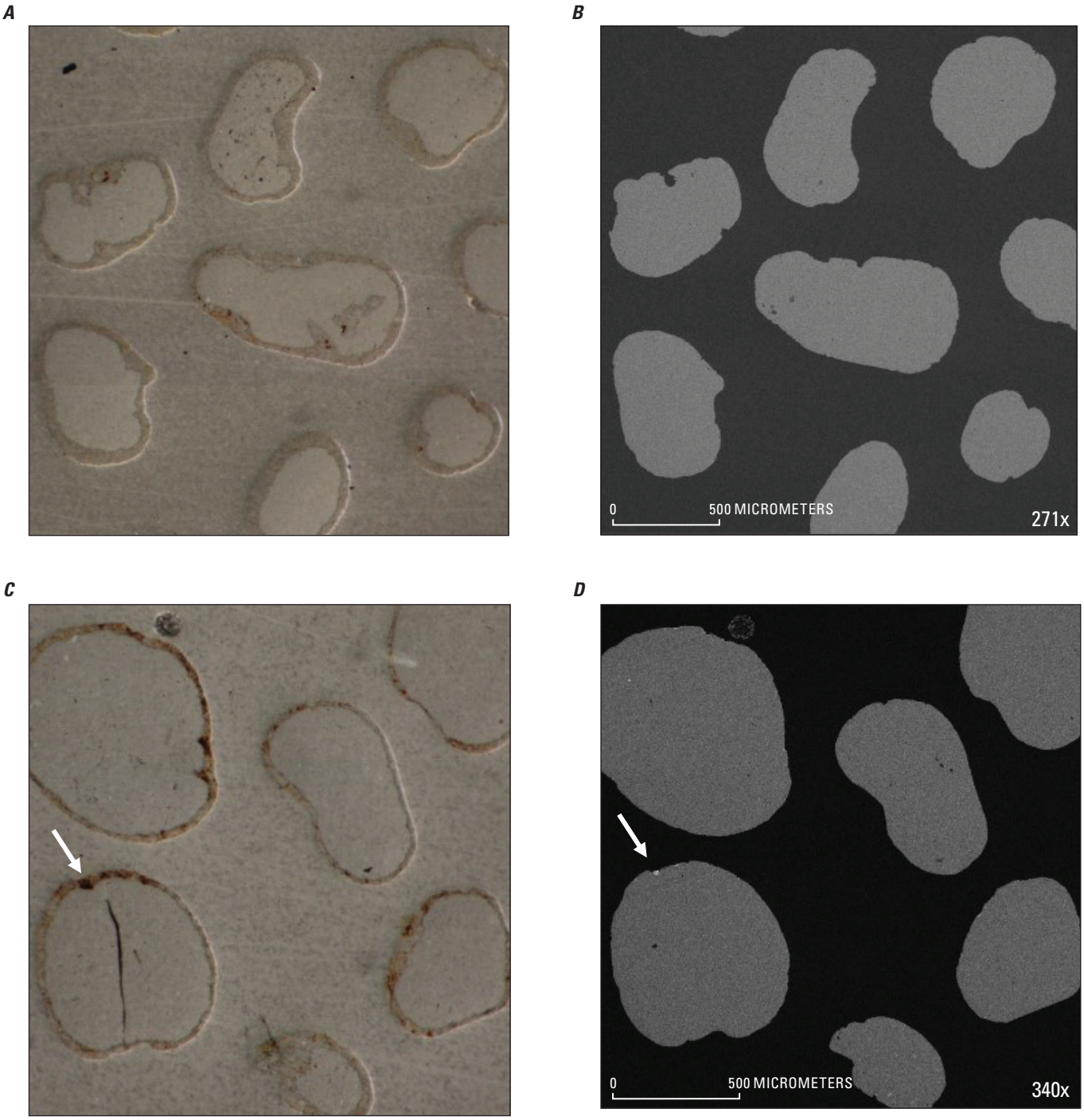

Figure I.30. Coupled optical and backscattered electron (BSE) images of the same areas of petrographic thin sections of iron (Fe) sand (*A* and *B*, 14 days of oxidation) and manganese (Mn) sand (*C* and *D*, 56 days of oxidation). Carbon coating on *A* and *C* makes the background of the optical images speckled. Data are available in Foster and others (2023).

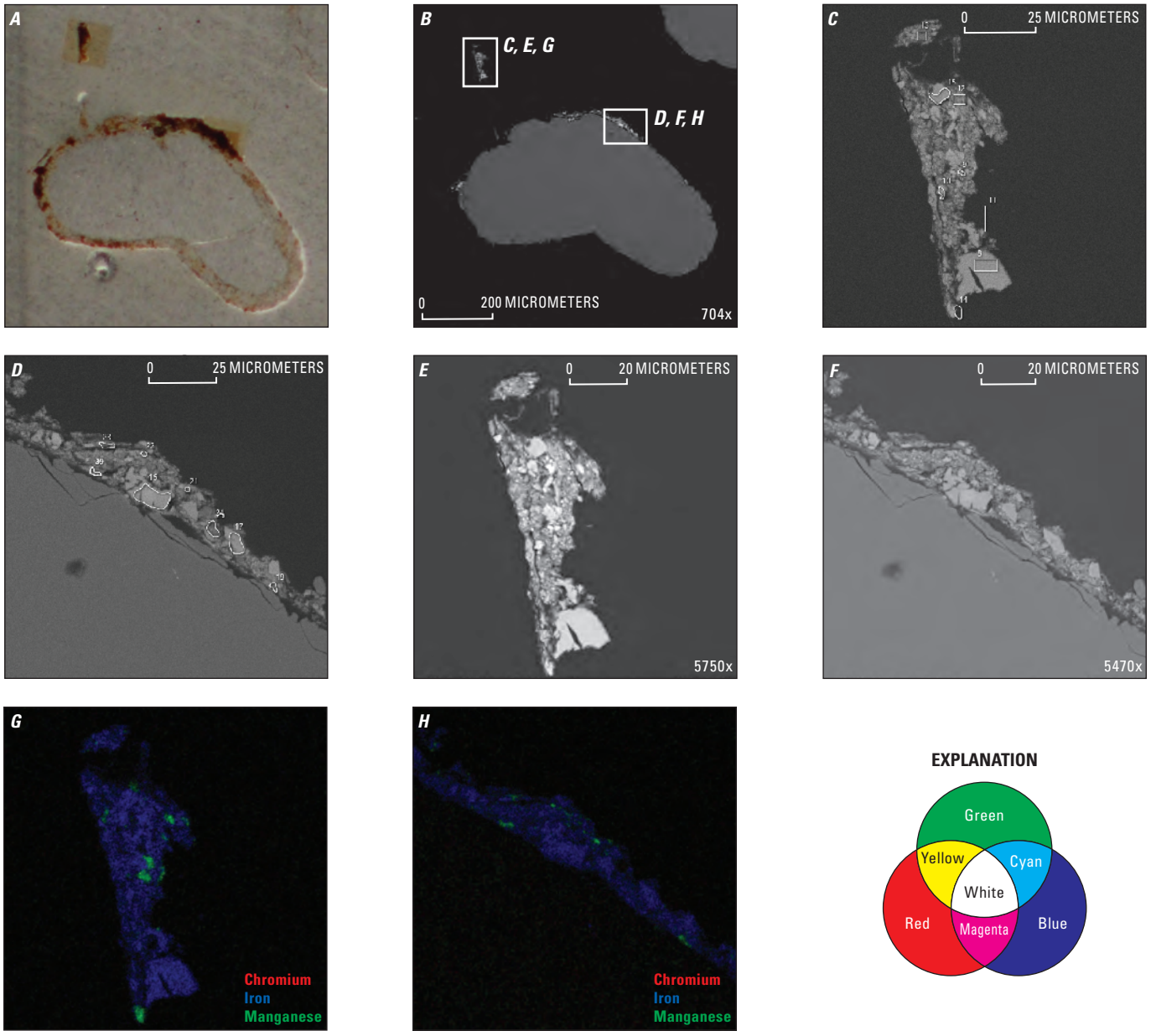

Figure I.31. Coupled *A*, optical and *B*, backscatter electron (BSE) images from iron/manganese 25 (Fe/Mn 25) at 56 days of oxidation. The white boxes in *B* correspond to close-up BSE image of precipitates presumably dislodged from the sand grain during preparation (*C* and *E)* and precipitates still associated with the sand grain (*D* and *F*). Points/areas of analyses are shown in *C* and *D*; *E* and *F* are higher resolution images of the same area. Tricolor element maps from scanning electron microscopy with energy dispersive spectrometry (SEM-EDS) in *G* and *H* show the co-location of Fe and Mn and the distinct morphologies present. Data are available in Foster and others (2023).

Concentrations of Cr, Fe, Mn, and Si on surfaces of artificial substrates were measured at selected times using multi-element EDS mapping described above. These data are presented as normalized percent by weight in box plots (figs. I.32–I.35). Silica derives from the washed sand starting material. Figures I.32*A* and I.33*A* show a lack of measured Cr in precursor materials Fe sand and Mn sand; therefore, it was assumed that precursor mixtures of Fe and Mn sand (figs. I.34–I.35) likewise did not contain Cr. After 1.25±0.2 years of reduction with added Cr, between 0.1 and 0.2 percent Cr by weight resided on surfaces in the solid phase of all substrates. Chromium remained at about that level during oxidation. The *B* panels on figures I.32–I.35 show the patterns in Fe concentrations through time. Approximately 10 percent of the solid-phase Fe was lost from the solid phase during reduction, leaving about 45 percent Fe by weight that was measured on the surface of Fe sand at the outset of oxidation, which remained unchanged during the first 14 days of oxidation. There was a trace amount of Fe in precursor Mn sand, which was undetectable after reduction and during oxidation. Iron remained constant on grain surfaces during oxidation of Fe/Mn 25 but decreased at 56 days in Fe/Mn 50. The *C* panels on figures I.32–I.35 show the patterns in Mn concentrations through time. The trace amount of Mn in precursor Fe sand was undetectable following reduction. About 45 percent Mn by weight resided on grain surfaces in precursor Mn sand, and this fraction increased to about 70 percent Mn by weight after reduction and remained elevated throughout 56 days of oxidation. About 10 percent Mn by weight was measured in Fe/Mn 25 early in the oxidation experiment and decreased thereafter. Manganese concentrations on surface grains of Fe/Mn 50 were initially below 10 percent by weight and increased markedly to 70 percent by weight at 56 days of oxidation.

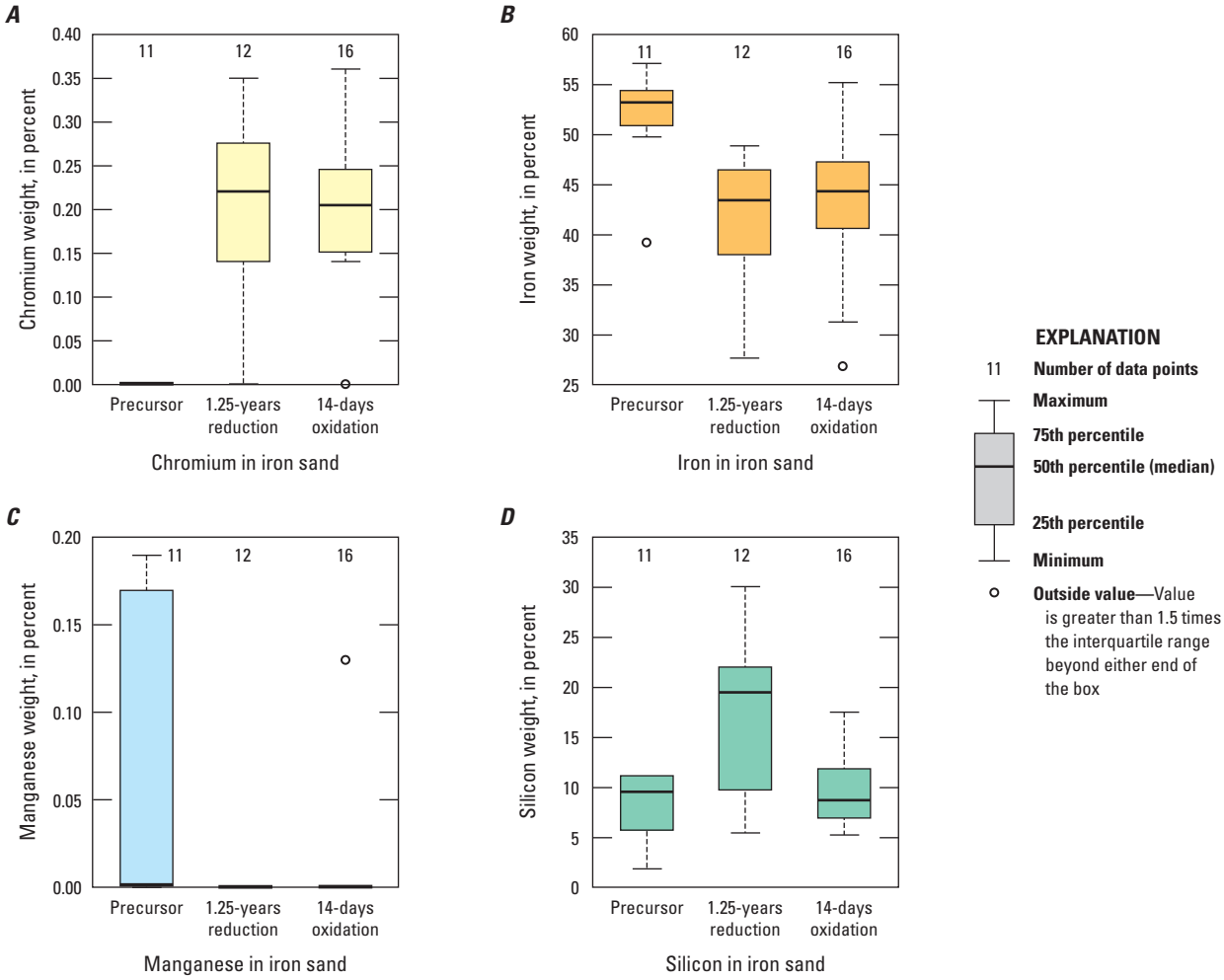

Figure I.32. Boxplots summarizing surface concentrations of solid-phase *A*, chromium (Cr); *B*, iron (Fe); *C*, manganese (Mn); and *D*, silicon (Si) in Fe sand as measured by scanning electron microscopy with energy dispersive spectroscopy (SEM-EDS) analysis of individual grains in precursor material (n=11) at 0 days of oxidation (1.25 years reduction; n=12) and after 14 days of oxidation (n=16). Data are available in Foster and others (2023).

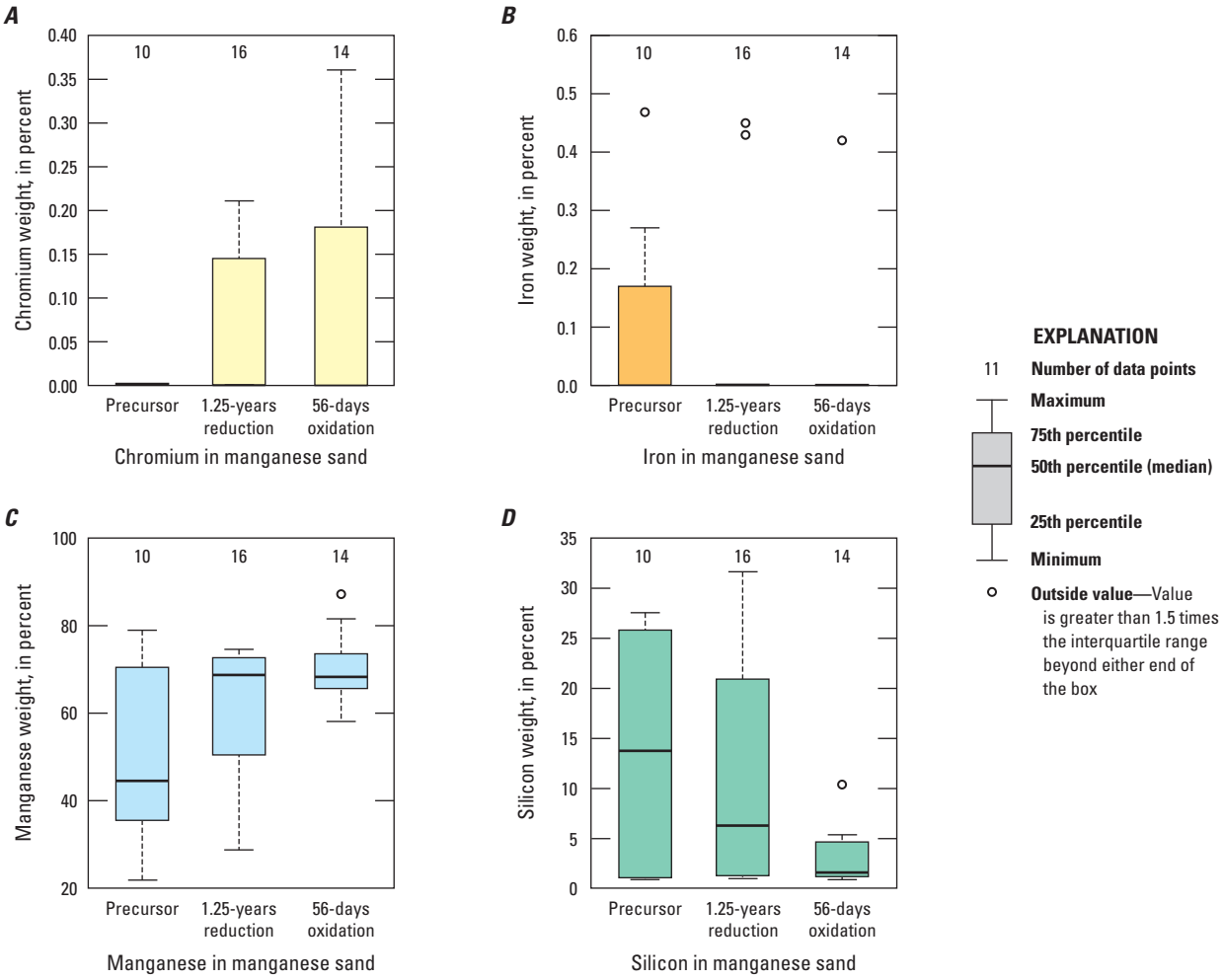

Figure I.33. Boxplots summarizing surface concentrations of solid-phase *A*, chromium (Cr); *B*, iron (Fe); *C*, manganese (Mn); and *D*, silicon (Si) in Mn sand as measured by scanning electron microscopy with energy dispersive spectroscopy (SEM-EDS) analysis of individual grains in precursor (n=10) material, at 0 days of oxidation (1.25 years reduction; n=16) and after 56 days of oxidation (n=14). Data are available in Foster and others (2023).

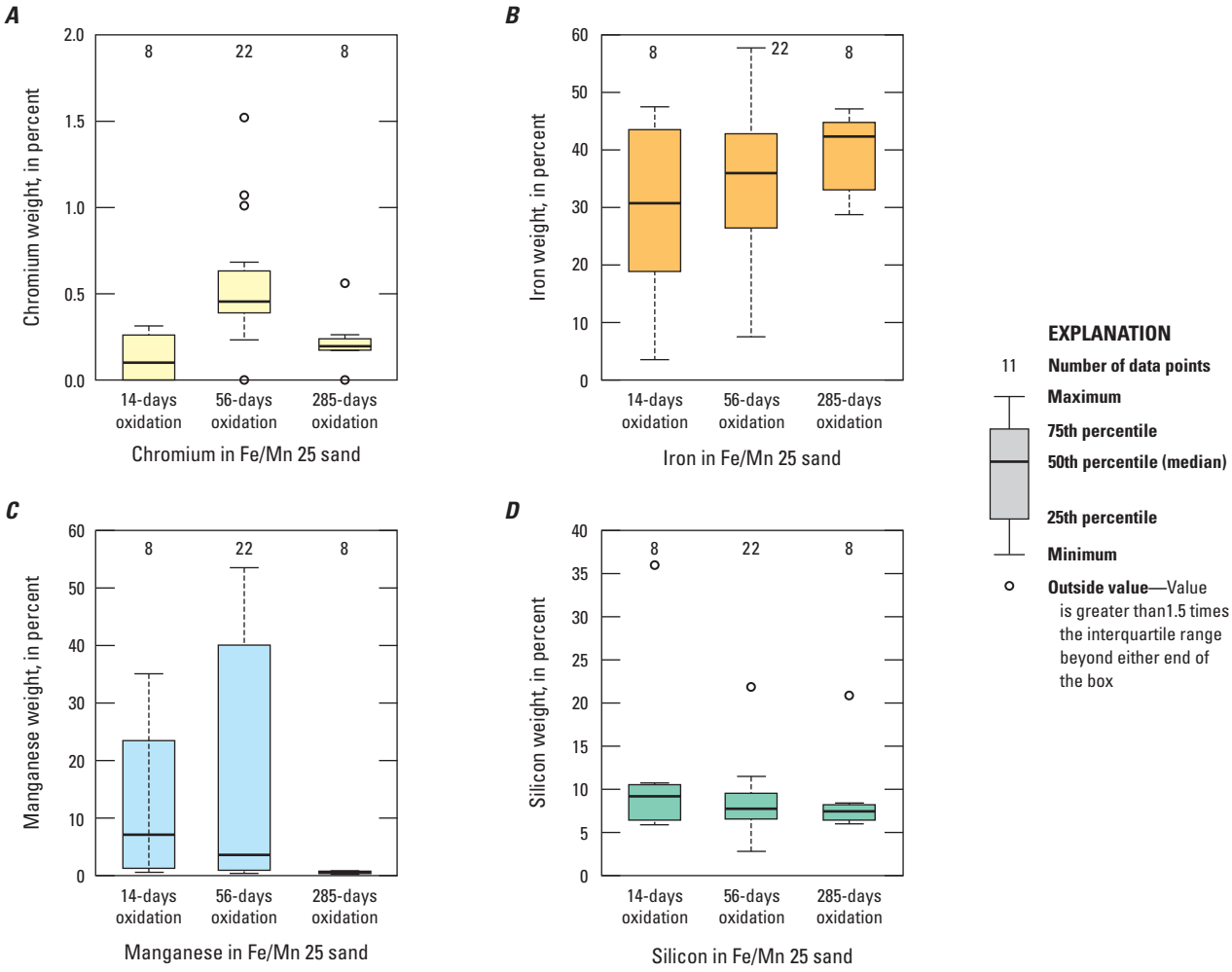

Figure I.34. Boxplots summarizing surface concentrations of solid-phase *A*, chromium (Cr); *B*, iron (Fe); *C*, manganese (Mn); and *D*, silicon (Si) in Fe/Mn 25 as measured by scanning electron microscopy with energy dispersive spectroscopy (SEM-EDS) analysis of individual grains after 14 days of oxidation (n=8), after 56 days of oxidation (n=22), and after 285 days of oxidation (n=8). Data are available in Foster and others (2023).

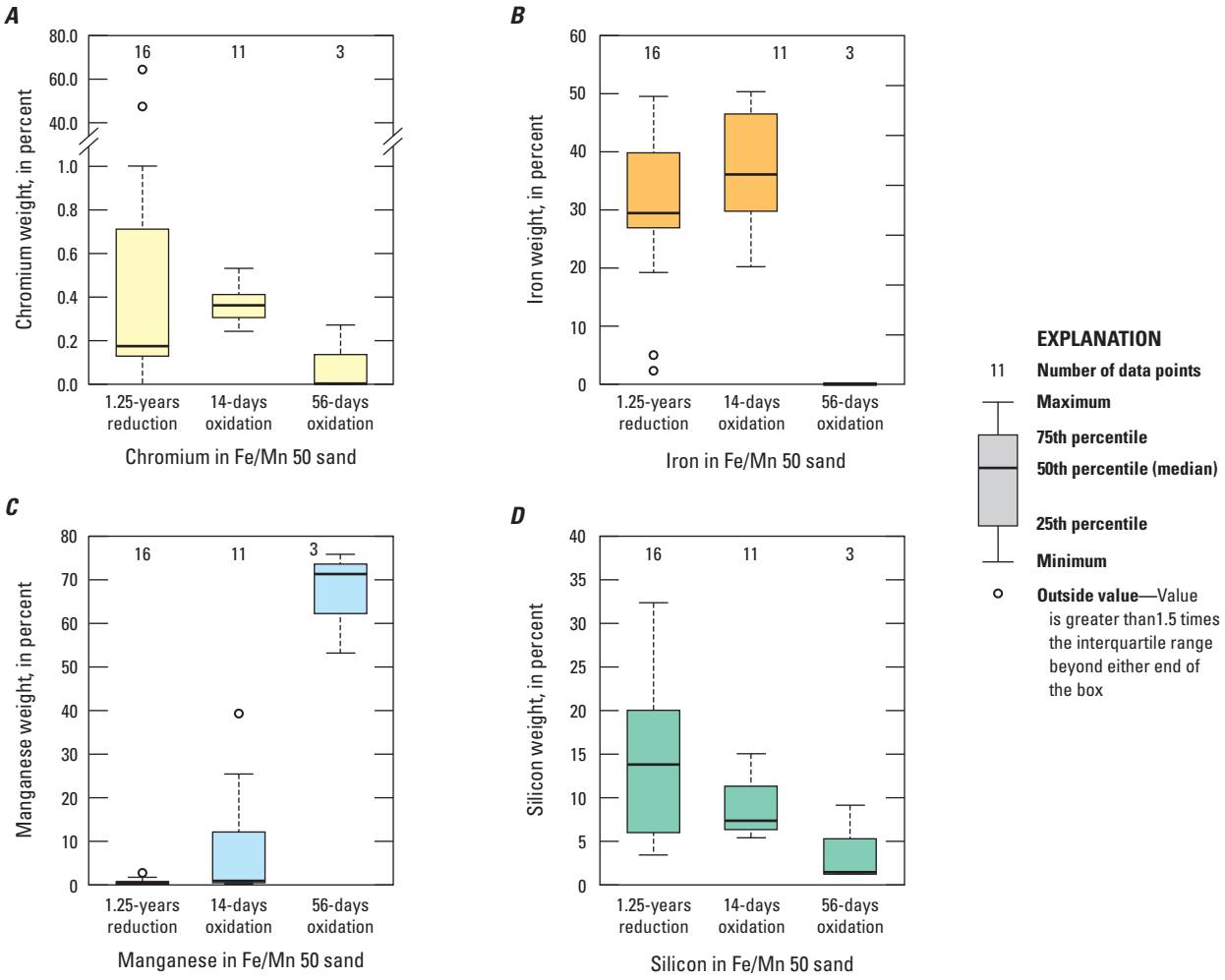

Figure I.35. Boxplots summarizing surface concentrations of solid-phase *A*, chromium (Cr); *B*, iron (Fe); *C*, manganese (Mn); and *D*, silicon (Si) in Fe/Mn 50 as measured by scanning electron microscopy with energy dispersive spectroscopy (SEM-EDS) analysis of individual grains at 0 days of oxidation (1.25 years reduction; n=16), after 14 days of oxidation (n=11), and after 56 days of oxidation (n=3). Data are available in Foster and others (2023).

All artificial substrate data presented on figures I.32–I.35 (excluding outliers) are represented in a ternary diagram with Fe, Mn, and Si end members (fig. I.36). Silica derives from the washed sand starting material. Samples of Fe sand plot on or near the Si-Fe axis, whereas samples of Mn sand plot on or near the Si-Mn axis; with one exception, none of the Fe-Mn mixed sands plotted along the axes; these data from Fe/Mn 50 or Fe/Mn 25 microcosms plot in the mid-field area.

Useable Cr bulk or micro-X-ray absorption near edge structure (μXANES) spectra on oxidation samples of site materials or artificial substrates were not obtained because of low Cr concentrations in samples. However, bulk Mn XANES spectra were collected for site materials at the start of oxidation and again 56 days later (fig. I.37). The last collection point for which beamtime was available was at 285 days of oxidation. Repeat spectra (1 of 2 and 2 of 2) collected on the same sample for the 14-day timepoint (T=14) showed that the X-ray beam did not affect the oxidation state of Mn in these samples. Manganese in all three sites (BG-0004, BG-0005, and SB-SA-01) was reduced at the start of oxidation and remained mostly reduced at 14 days in BG-0004 and BG-0005. However, by 56 days, samples more closely resembled precursor site material. Site SA-SB-01 evolved in a similar way from 0 to 56 days of oxidation. These findings indicate that higher oxidation states of Mn, especially Mn(IV), were formed early in the oxidation period and were available to participate in Cr(III) oxidation to Cr(VI).

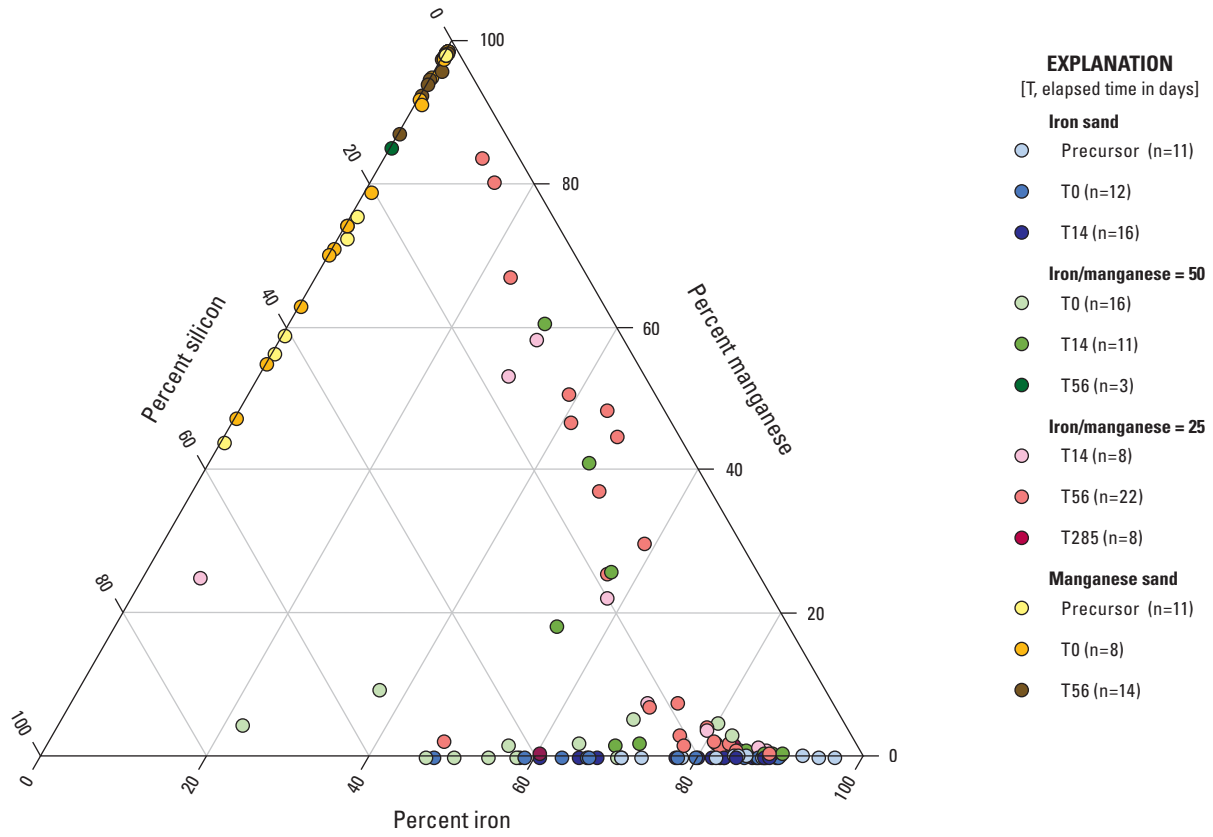

Figure I.36. Ternary plot summarizing the results of scanning electron microscopy (SEM) area (grain) and point analyses of artificial substrates iron (Fe) sand, manganese (Mn) sand, Fe/Mn 50, and Fe/Mn 25. (Note: element percent by weight compositions for silicon (Si)-Mn-Fe were re-normalized to 100 to produce this graph). Data are available in Foster and others (2023).

Manganese XANES of artificial substrates illustrated the redox status of Mn-containing solid products early in the oxidation process. In addition to Mn carbonate, minerals that are likely present after reduction for 1.25±0.2 years included magnetite which may display some degree of substitution of Cr and Mn for Fe. Figures I.38*A* and I.38*B* show µXANES spectra for Mn of Fe/Mn 50 and Mn-coated sand collected after 14 days of oxidation; these spectra are strikingly similar to the Fe XANES spectrum reported for jacobsite (fig. I.38*C*) in O'Day and others (2004). Jacobsite is a Fe-Mn mineral with a general formula of $(Mn^{2+}Fe^{2+})(Mn^{3+}Fe^{3+})_2O_4$ that is isostructural (has similar mineral structures) with chromite, magnetite, and hausmannite (Mn^{2+} $(Mn^{3+})_2O_4$). Similarities among spectra on figures I.38*A–C* strongly indicate that the jacobsite is the phase hosting the majority of Mn in Fe/Mn 50 and the Mn-coated sand 14 days after the onset of the oxidation experiment.

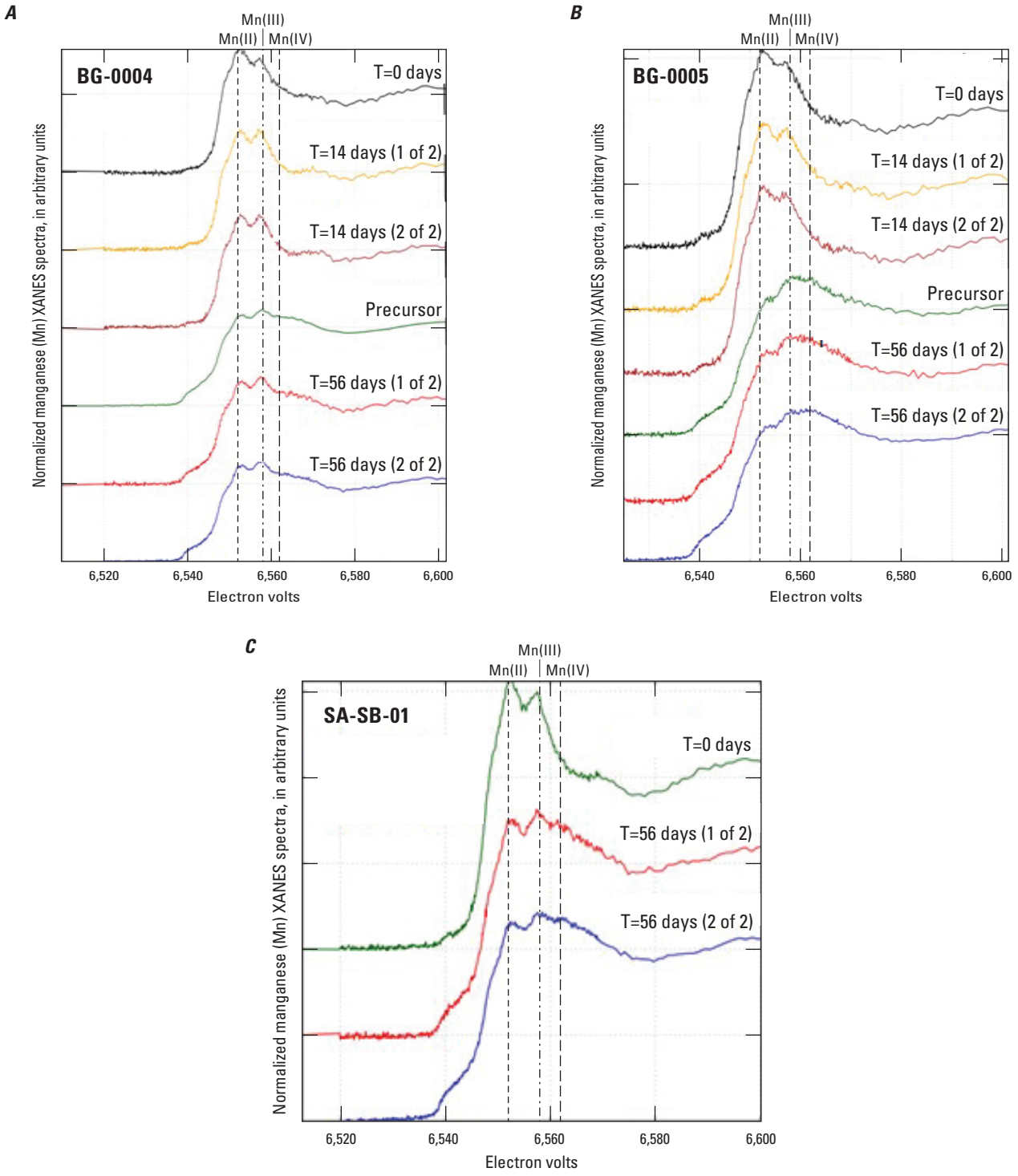

Figure I.37. Bulk manganese X-ray absorption near edge spectra (Mn XANES) of sites *A*, BG-0004; *B*, BG-0005; and *C*, SA-SB-01 comparing precursor, 0, 14, and 56 days of oxidation timepoints in *A* and *B* and 0 and 56 days of oxidation timepoints *C*. Replicate spectra (1 of 2 and 2 of 2) are shown to document that the sample of SA-SB-01 collected at 56 days of oxidation did not change speciation during repeated exposure to the synchrotron X-ray beam. Data are available in Foster and others (2023).

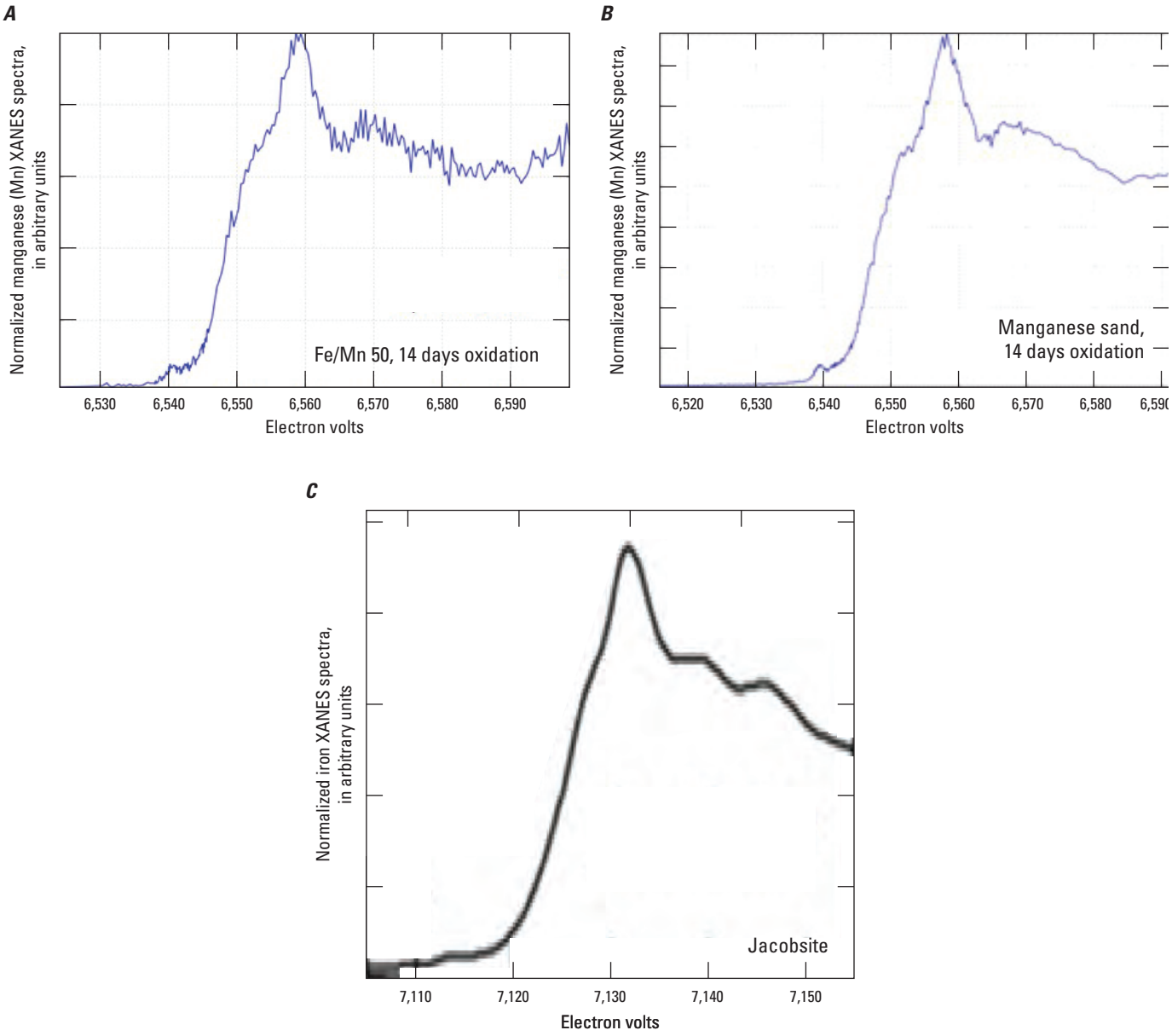

Figure I.38. Comparison of manganese (Mn) X-ray absorption near edge spectra (XANES) of *A*, iron/manganese 50 (Fe/Mn 50) and *B*, Mn-coated sand at 14 days of oxidation with *C*, the Fe XANES of jacobsite published by O'Day and others (2004). Data are available in Foster and others (2023).

I.4. Discussion

The preliminary experiment guided design of the reduction and oxidation experiments with respect to management of microcosms. The reduction experiment was completed to evaluate the fate of Cr and transformations that occur at particle surfaces during reduction. Chromium was concentrated to observe reduced products greater than the detection limit in an elevated Cr reduction experiment done to supplement data collected as part of the reduction experiment. The oxidation experiment was completed to determine if Cr(III) could be oxidized to Cr(VI) and released from surface sorption sites into groundwater within the IRZ if hydrologic and geochemical conditions were to change in the future. Artificial substrates were used in the reduction and oxidation experiments to help understand processes occurring at particle surfaces. Results of the microcosm experiments were used to determine if Cr(III) could reoxidize to Cr(VI) if conditions within the IRZ changed.

Microcosm results are not directly comparable to Cr behavior in aquifer settings within the IRZ, where dissolved constituents may move downgradient with groundwater. However, similarities in microcosm results and environmental site data were observed.

I.4.1. Lessons Learned from the Preliminary Experiment

The preliminary experiment was completed to assess the ethanol dosing regimen needed to maintain reduced conditions in microcosms within appropriate ranges, avoiding sulfate reducing or methanogenic conditions, while mimicking field conditions. Preliminary results were used to determine when to harvest bottles during the subsequent long-term reduction experiment. Results showed that Cr was rapidly reduced in the presence of ethanol (during oxic and anoxic conditions) and that fermentation of excess ethanol to acetate was likely responsible for the pH decreases observed in bottles with added 10 mM HEPES and EPPS buffers. Results also showed that weekly additions of 1 percent ethanol for the first 3 months and monthly additions thereafter would stimulate heterotrophic microbial activity while not resulting in build-up of excess ethanol that would create more reduced conditions within microcosms than observed within the field IRZ. Additionally, organic pH buffers were metabolized by the microbial community within the microcosms, resulting in sulfate reduction and enhanced SO_4^{-2} removal within the microcosms compared to conditions within the IRZ; consequently, pH could not be controlled within desired ranges using these organic buffers while maintaining the redox status of study microcosms.

In summary, preliminary results indicated that (1) Cr(VI) was rapidly and completely removed in buffered and un-buffered microcosms; (2) organic buffers contributed to decreased redox state within the microcosms, complicating efforts to maintain pH within ranges appropriate for either maximum oxidation of Cr(III) to Cr(VI) or maximum desorption of Cr(VI) from aquifer solids; and (3) sulfate reduction and variations in pH likely could be avoided with careful ethanol dosing while not artificially buffering the microcosms. Preliminary results were used to guide design of the longer-term reduction and oxidation experiments.

I.4.2. Reduction Experiment

Sequential extractions of aquifer site materials and artificial substrates revealed that Cr was progressively associated with more recalcitrant phases as reduction proceeded. Some Cr(VI) was initially sorbed to particle surfaces while the microcosms were still oxic. However, within 83 days, Cr(VI) that was reduced to Cr(III) had passed through weakly and specifically sorbed fractions and was ultimately mineralized and associated with an unaccounted for amorphous fraction or with the crystalline phase. The exact nature of Cr in the crystalline phase was not determined; however, evidence of Cr hydroxide precipitation was not found. Analysis by SEM-EDS, XANES, and μXANES provided evidence that secondary mixed-valence Fe and Mn minerals were present during later stages of reduction. Secondary mineral formation during reduction, specifically substitution of Cr in Fe- or Fe-Mn-crystalline phases, influenced the availability of Cr(III) and the potential for association of Cr(III) with freshly formed Mn oxides upon aquifer reoxidation. Co-location of Cr and Mn observed during the reduction experiment may contribute to reoxidation of Cr if oxic conditions are restored within IRZ treated aquifer material.

I.4.2.1. Reduction of Site Materials

The pattern of chromium-50 sequestration deduced from sequential extractions of microcosms harvested (incubation terminated) at specific timepoints was consistent among site materials. Most of the chromium-50 was associated with the crystalline phase within 83 days of reduction. Chromium-50 continued to accumulate in the crystalline phase of material from BG-0004 but not in material from BG-0005 containing older Mojave River material having more Mn (fig. I.3*E*). Plotting all five sequential extracts for each date together as stacked bar graphs revealed a mass imbalance for Cr (figs. I.4*A*, *D*). The simplest explanation for the observed deficit during the mid-late stages of reduction is that Cr was sequestered in a fraction that was not fully recovered by the method of sequential extractions.

Some of the missing Cr may have been associated with organic matter not subject to release by either ammonium oxalate (extraction 3 in table I.3) or 4N HNO_3 (4N nitric acid extraction, extraction 4 in table I.3). Soluble and insoluble organo-Cr(III) products are known to form during Cr(VI) reduction by *Escherichia coli* (Puzon and others, 2005). Although desert aquifers do not typically contain large quantities of natural organic matter, considerable microbiological growth occurred in the microcosms because of ethanol additions (table I.4). Biofilm growth, as well as the gasses the microbes produce and minerals that precipitate, have been observed to clog wells within the IRZ in Hinkley Valley over time. The Pacific Gas and Electric Company does maintenance to periodically clean the wells (Margret Gentile, ARCADIS, Inc., written commun., 2021). Chromium may have been complexed by this organic material. Consistent with this explanation, microbial mats have been shown to incorporate large amounts of Cr at surface-water contamination sites (Abed and others, 2020).

Oxidants (hydrogen peroxide, ascorbic acid, sodium persulfate, or perchlorate) are often added following ammonium oxalate in extraction protocols designed to mobilize organically bound metals and metals associated with amorphous Fe and Mn oxides during extraction 3 (table I.3; Zimmerman and Weindorf, 2010). Adding oxidants causes organic carbon to be more readily oxidized than with oxalate alone (Tessier and others, 1979). Oxidants were not included as part of the sequential extraction steps used in this study; therefore, organically bound chromium-50 may not have been fully accounted for in the samples. Likewise, reaction with 4N HNO_3 (4N nitric acid extraction; extraction 4 in table I.3) without additional oxidants such as perchlorate or hydrogen peroxide may not completely oxidize organic matter (Papp and others, 1991; Mikutta and others, 2005). Therefore, Cr bound to organic carbon may account for unrecovered reduced Cr product in the sequential extractions.

Sites SA-RW-34, BG-0004, BG-0005, and SA-SB-01 contained enough organic carbon initially (0.05–0.20 percent w/w) to account for the missing Cr (table I.4). In addition, organic matter increased to 6.6–6.8 percent w/w following reduction with ethanol for 2 years. Biofilms (composed of microbial cells and metabolic products) were observed forming after repeated additions of 1 percent ethanol during incubations of all materials except washed sand. Sequential extractions of Mojave River aquifer material were done separately (chapter C, appendix C.1) using oxalate followed by ascorbic acid. Comparison of the extraction results with those in chapter C within this professional paper indicate that additional Cr was associated with the organic fraction of BG-0004 and BG-0005, which was not measured. To rely solely on insufficiency of extraction 3 (table I.3) to explain the mass imbalance during incubations with site material requires that the amorphous fraction extractions underestimated the amount of recoverable chromium-50 by a factor of four (from 250 to more than 1,000 ng/g) by not including organics. This hypothesis leads to the indication that organically bound chromium-50 was further mineralized to the crystalline phase after 83 days of incubation in BG-0004 (fig. I.4*A*) but not in BG-0005 (fig. I.4*D*).

The total extractable Fe recovered during sequential extractions from study microcosms was comparable to the amount of extractable iron measured in site materials (chapter C, fig. C.14*B*; Groover and Izbicki, 2018). Iron was initially recovered only in crystalline and amorphous fractions during extractions of incubated site materials. Iron-bearing minerals observed by XRD in precursor materials include fully oxidized hematite, as well as trace amounts of magnetite (chapter C, table C.6). Iron was not detected in sorbed and aqueous fractions of sequential extractions until 350 days of reduction.

The total amount of extractable Mn recovered during sequential extractions of site materials was two to three times lower than the extractable Mn values reported in chapter C within this professional paper (chapter C, fig. C.14*C*; appendix C.1, table C.1.1), and both values were as low as one-tenth of the total amount measured in solids by pXRF (Groover and Izbicki, 2018). The reason for less than complete extraction of Mn is unclear, but it is possible that recalcitrant Mn (not extractable using 4N HNO_3) may be present in site materials. The SEM-EDS analyses of reduced site materials, show clays containing Mn (fig I.10*B*) and what appeared to be Mn silicates (fig. I.20). These minerals are resistant to extraction by 4N HNO_3. During the reduction experiment, Mn (like Fe) was initially detected only in crystalline and amorphous fractions of site materials. Precursor site materials analyzed by XANES contained Mn in three oxidation states: Mn(II), Mn(III), and Mn(IV) (fig. I.22). As reduction proceeded, Mn(IV) content decreased and Mn(III) content increased (figs. I.22–I.23), indicating an increase in soluble Mn.

A modest increase in total Mn extracted from site materials with time (figs. I.4*C*, *F*) can be ascribed to redistribution of organically bound Mn that was not captured by earlier extractions. The transition to majority Mn present in aqueous and sorbed fractions after 83 days of reduction indicates that by this time most Mn species in the systems were Mn(II) or Mn(III), which are more soluble than Mn(IV). This is consistent with the XANES results showing loss of Mn(IV). The observed broad distribution of Mn among all operationally defined fractions within the microcosms increases the likelihood that Mn (and Mn-oxidizing bacteria) would be co-located with sequestered Cr in a bioremediated environment at the onset of any future reoxidation event. This co-location was confirmed by SEM-EDS mapping of Cr-Mn-Fe in vortex-liberated fine samples of the elevated Cr experiment (fig. I.15) and in samples from BG-0005 (fig. I.20) and SA-SB-01 (fig. I.21) after 1.25 years of reduction.

I.4.2.2. Reduction of Artificial Substrates

Chromium was completely sequestered during incubations of washed sand and Fe sand (fig. I.3). As with site materials, some of the 1,600 ng/g of added chromium-50 was not recovered, possibly as a result of incorporation into organic material. Plotting all sequential extracts for each date together as stacked bar graphs (figs. I.5*A*, *D*) revealed a mass imbalance of chromium-50, particularly for Fe sand at later stages of reduction. For washed sand, the trend was less obvious and might have been influenced by the lack of an initial measurement.

Chromium was retained longer in the weakly sorbed and specifically sorbed fractions in artificial substrates than in site materials (figs. I.3*B*–*C*), particularly for the specifically sorbed fraction of washed sand microcosms. Sorption of Cr(VI) to particle surfaces is generally slow at circumneutral pH and decreases as pH increases (Rai and others, 1989). However, reduction of Cr(VI) to Cr(III) occurs on quartz and amorphous silica fractions in the presence of Fe(II) (Nelson and others, 2019). Chromium-50 in the amorphous fraction of Fe sand was elevated (50–100 ng/g) and more like site materials at later stages of reduction. By contrast, little chromium-50 was recovered in the amorphous fraction of washed sand throughout the incubations, which could result from less residual Fe available to create amorphous Fe-Cr complexes.

The amount of chromium-50 extracted from the crystalline phase of artificial substrates was less than half of the amount recovered from site materials at comparable times (fig. I.2). Less mineralization and slower rates of sequestration were likely due to the lack of crystalline Fe(III) minerals (other than HFO coatings) in artificial substrates. Iron(III)-bearing minerals (hematite, goethite, or other ferric-oxides) present in site materials and not in artificial substrates have been shown to enhance the rate of Cr sequestration by providing surfaces for sorption to occur and by reducing Fe to Fe(II), which may facilitate Cr reduction (Peterson and others, 1997a).

Sequential extractions of Fe sand yielded total Fe amounts that were comparable to site materials, whereas washed sand yielded a minor amount of extractable Fe (fig. I.5*B*). Surprisingly, chromium-50 was sequestered to a similar extent during incubations of washed sand and Fe sand. Therefore, Fe(III) coatings (HFO) may not have controlled sorption and reduction, the mechanisms responsible for Cr removal from the aqueous phase. Hydrous ferric oxide coatings were expected to promote removal of chromium-50 because reduction of HFO produces magnetite, a mixed valence Fe(III)/Fe(II) oxide, which is an ideal surface for Cr(VI) to sorb to and for reduction to occur (Peterson and others, 1997b). However, enhanced Cr removal by this process was not observed.

Added chromium-50 was primarily sequestered in the crystalline phase of artificial substrates after 168 days of incubation. This result was not surprising for Fe sand given the amount of Fe from HFO available to promote sorption and reduction. However, sequestration in the crystalline phase was unexpected for washed sand, which was intended to be a control that was free of added Fe. The trace amount of aqueous Fe present in the native groundwater (table I.2) used for these incubations (equivalent to less than 12 ng/g of material) could not account for this mineralization. More likely, low amounts of Fe remained after extensive efforts to remove Fe during acid washing of washed sand (fig. I.5*B*), which later contributed to Cr sequestration. Incubations of washed sand using autoclaved water from BG-0004 showed that sequestration could not be attributed to abiotic processes alone (fig. I.6). In that case, sequential extractions of sterile washed sand after 108- and 248-day incubations indicated no reduction of Cr with added ethanol. Chromium-50 added initially as Cr(VI) remained entirely associated with aqueous and weakly sorbed fractions; therefore, Cr was not sequestered into crystalline mineral phases in the absence of viable microbes.

I.4.2.3. Interpretation of Solid-Phase Analyses

Changes in the oxidation state of Fe- and Mn-containing minerals were observed during prolonged reductions of microcosms. The biggest changes were transformations of predominantly Fe(III) minerals (such as hematite and ferrihydrite; figs. I.7, I.9) in site materials to predominantly Fe(II)-containing minerals (figs. I.10–I.12). Formation of reduced Fe minerals during reduction was confirmed in samples reduced for 1.25±0.2 years (fig. I.13) and from the elevated Cr reduction experiment (fig. I.14) using SEM-EDS analysis and mapping of vortex-liberated samples. Figures I.10–I.14 show the locations (spots) where spectra were collected; these spectra can be referenced by figure number and image number in the accompanying solid-phase data release (Foster and others, 2023) and are summarized in table I.6.

Data plotted in the interior of the ternary diagram (fig. I.15*A*) represent spots where all three elements (Cr, Fe, and Mn) were co-located (within the 1.2-µm beam resolution), either in a mineral or in proximity. Co-location of these elements (on a scale of several µm) also was observed on coatings of grains and grain fragments of site materials after reduction at the start of the oxidation experiment (fig. I.20). The closeness of Cr(III)-bearing minerals to Mn oxides exerts a controlling effect on the oxidation of Cr(III) and release of Cr(VI) in flowing groundwaters (Hausladen and others, 2019). Proximity is expected to have greater importance in the closed microcosm incubations because diffusion was less of a barrier to the transport of aqueous Cr(III) or Mn oxides in agitated bottles than in groundwater.

Additional evidence that Cr, Fe, and Mn were redistributed and eventually co-located during reduction comes from observations of the solid phase of mixed artificial substrates. When pure end members Fe sand and Mn sand were physically homogenized to prepare mixtures, the coatings remained segregated, meaning that sand grains had either Fe coatings or Mn coatings but not both. By the end of reduction, coatings were found to contain Cr, Fe, and Mn in proximity to one another (fig. I.16).

Our Cr XANES results indicated a predominance of Fe-Cr hydroxide compared to Cr-substituted magnetite in site materials after 83 and 350 days of reduction (fig. I.18) and in the elevated Cr experiment after 8 months of reduction (fig. I.19). Iron-chromium hydroxide is typically produced at an ideal Fe/Cr ratio of 3 (table I.7). Hansel and others (2003a) reported that Fe-Cr hydroxide with Fe/Cr ratios lower than the ideal ratio of 3 could form during later stages of Cr(VI) reduction using Fe(II) from ferrihydrite as an electron donor. They concluded that Fe(II) in the product Fe-Cr hydroxide could be recycled and used to abiotically reduce Cr(VI), thereby depleting the Fe-Cr hydroxide product of Fe with time. Depletion of Fe could proceed as long as Cr(VI) reduction was ongoing. In the closed system incubations, this recycling of Fe(II), if it occurred, would have ceased after 41 days when Cr(VI) was depleted. Figure I.15*B* illustrates the observed relations between Cr and Fe that indicate Fe-Cr hydroxide was formed with a Fe/Cr ratio greater than the ideal ratio of 3 during reduction. A possible scenario for Fe-Cr hydroxide formation and preservation at a higher than "ideal" Fe/Cr ratio of 3 is that Cr(VI) reduction was not driven by reduced Fe but rather was a predominantly enzymatic process, operating concurrently with Fe reduction and possibly SO_4^{-2} reduction. Competition with sulfide for the produced Fe(II) would keep the Fe(II) content low in any Fe-Cr hydroxide product. Less Fe(II) in the product (higher Fe(III)/Fe(II) ratio) would reduce the effect of recycling and maintain a Fe/Cr ratio above 3. Figure I.15*C* shows a nearly 1:1 trend in the ratio of Cr/Mn that indicates substitution of Cr together with Mn in Fe-bearing minerals such as magnetite or jacobsite.

An increased abundance of clay minerals was observed at later stages of reduction of site materials using SEM-EDS (figs. I.12–I.13). The analytical approach lacked the sensitivity to confirm the presence of Cr in clays. Clay particles were associated with Fe, S, Al, and in some cases Mn; however, it could not be determined if Cr or Mn were structurally included in the clays or sorbed to the surface of clays using the techniques available for this study. In SA-SB-01, sulfide particles were clearly embedded in clay layers after additional reduction.

I.4.3. Oxidation Experiment

The oxidation experiment was designed to (1) determine if Cr(VI) was produced and available for release from sequestered fractions following oxidation of previously reduced aquifer materials and (2) evaluate the role of Fe and Mn in the processes of Cr oxidation and release. The items addressed were (1) using results from site materials and (2) using results from artificial substrates containing coated sand with different Fe/Mn ratios.

I.4.3.1. Oxidation of Site Materials

A small amount of Cr(III) was oxidized from site materials and released as aqueous Cr(VI) within the study microcosms during the 2-year reoxidation experiment (fig. I.24). Less Cr(VI) was released to the aqueous phase by BG-0004 (composed of recent Mojave River materials) than BG-0005 (composed of older Mojave River materials), and release occurred later in the period of oxidation (after 285 days). The amount of Cr(VI) released from SA-SB-01 to the aqueous phase was midway between the amounts released in BG-0004 and BG-0005. Somewhat more aqueous Cr(VI) was recovered from SA-SB-01 after oxidation for 285 and 679 days. The amount of Cr(VI) released to the aqueous phase was never more than 3 percent of the 3,000 ng/g Cr added initially and reduced. The added Cr was representative of aqueous Cr(VI) concentrations of 1,000 µg/L.

Aqueous Cr(VI) concentrations are potentially environmentally significant relative to background Cr(VI) concentrations calculated as part of this study, but making direct comparisons between microcosm and environmental data is challenging. Similar release of Cr(VI) to the aqueous phase was reported for a flowing groundwater system in Italy by Slejko and others (2019). They provided isotopic ($^{53}Cr/^{52}Cr$) evidence of oxidation of Cr(III) via Mn oxides hosted in the aquifer. The Cr(III) originated in the aquifer by natural attenuation (reduction) of an industrial contamination that occurred decades earlier.

Additional Cr(VI) was released from the solid phase of site materials following extraction with strong alkaline solution, indicating that Cr(III) had been oxidized to Cr(VI) within the microcosms but was bound to particle surfaces and not present in the aqueous phase. The pattern of oxidation was consistent among all materials, with more Cr(VI) extracted at middle periods of oxidation (56, 125, and 285 days) than earlier or later. Initial increases (0–56 days) may indicate the time required for Mn oxides to form in proximity to sequestered Cr(III). Wu and others (2005) showed that Cr(III) oxidation occurs on a time scale of weeks via a catalytic pathway in which microbes mediate Mn(II) oxidation to form Mn(III) or Mn(IV) oxides, and where Cr(III) was subsequently oxidized by these biogenic Mn-oxides. In the oxidation experiment, later decreases in aqueous Cr may indicate adsorption of aqueous Cr(VI) to freshly formed Fe and Mn oxides, with potential for armoring as new (Cr-poor) oxides cover up (occlude) sorbed Cr. Armoring may be a consequence of the closed system incubations, where soluble Fe remains available to react with reduced Cr(III). In a flowing groundwater regime, aqueous Fe(II) may be transported downgradient and would be less available to oxidize and participate in Cr armoring (Fandeur and others, 2009a).

Extractable solid Cr(VI) represented up to 10 percent of the amount of Cr added in BG-0004 and SA-SB-01 and the 20 percent added in BG-0005. This intra-site difference supports a previous finding of the reduction experiment (figs. I.3–I.4) that more Cr(VI) was bound in the crystalline phase of BG-0004 than BG-0005 and indicates that the three times greater amount of Mn available in BG-0005 was enhancing oxidation of Cr(III) to Cr(V) (Eary and Rai, 1987; Murray and Tebo, 2007). Tokunaga and others (2007) reported enhanced Cr(III) oxidation during reduction experiments with columns using Hanford soils with much greater Cr(VI) exposure, and they also provided evidence of a link to the Mn oxidation state.

The amount of solid (extractable) Cr(VI) available for release upon oxidation of SA-SB-01 was similar to the amount available from BG-0004 and only half the amount available from BG-0005. This result was surprising because the aquifer at SA-SB-01 contained anthropogenic Cr released from the Hinkley compressor station and had been treated and reduced for several years by ISR before sampling. In situ reduction may have produced different Cr(III)-bearing minerals than those produced in the microcosms. Manganese was not measured by sequential extractions of SA-SB-01; however, qualitative pXRF measurements indicated there was more Mn present than in BG-0004.

I.4.3.2. Oxidation of Artificial Substrates

Artificial substrate precursors consisted of quartz sand with coatings of ferrihydrite (Fe) or hausmannite (Mn) prepared as pure end members or mixtures designed to bracket the Fe/Mn ratio of Mojave River aquifer materials (Fe/Mn 50; chapter C). In contrast to site materials, clays and native Fe and Mn oxides and hydroxides were initially absent from artificial substrates. Therefore, the principal variables controlling sequestration and release of Cr in artificial substrates were the ratio of Fe/Mn in the surface coatings and the composition and structure of minerals produced during reduction. Consequently, the chemical and mineral composition at the outset of oxidation was less complex than in site materials. Experimental data showed Cr(III) was less likely to be bound in the crystalline phase and more likely to be co-located with Fe and Mn in other fractions at the end of the reduction period. This resulted in more Cr(VI) available for release following initial oxidation of artificial substrates (figs. I.25–I.26) than in site materials (fig. I.24).

In addition, Cr(VI) was more rapidly released to the aqueous phase during oxidation of artificial substrates than from oxidation of site materials. Aqueous Cr(VI) was observed immediately (0 days of oxidation) and after 14 and 56 days of oxidation of artificial substrates. More Cr(VI) was released by mixtures of Fe- and Mn-coated sand than pure end members. The greatest release (greater than 500 ng/g) was observed at 14 days of oxidation of Fe/Mn 100. These samples are the only instance where aqueous phase Cr(VI) exceeded extractable solid-phase Cr(VI). The coefficient of determination, R^2, for the relation between aqueous Cr(VI) and pH at the time of extraction was low, and not significantly different from 0 on the basis of the t-test (Neter and Wasserman; fig. I.39), indicating that these elevated Cr(VI) concentrations were not the result of desorption by hydroxide ions. This lack of relationship was not surprising because little Cr was associated with the specifically sorbed fraction during sequential extractions of the reduction experiment. The specifically sorbed fraction is the most pH dependent fraction (Chao and Sanzolone, 1989).

The pattern of Cr(VI) extracted by strong alkaline solutions from artificial substrates through time was similar to that of site materials, in that greater amounts of Cr(VI) were extracted at middle periods of oxidation (56, 125, and 285 days) than earlier or later. This pattern of Cr release was consistent among all materials tested. Artificial substrates with the highest Mn content released the most Cr(VI) following extraction. Up to 800 ng/g Cr(VI) was extracted from solids after 125 days of oxidation of pure Mn sand and Fe/Mn 25. This is consistent with previous work (Bartlett and James, 1979) showing higher rates of Cr(III) oxidation in soils with higher Mn content. Oxidation of the two higher Mn content artificial substrates (Fe/Mn 25- and Mn-coated sand) likely produced sufficient amounts of Mn(III and IV) oxides (Nico and Zasoski, 2000) and at the proper locations to react with Cr(III) to a greater extent than did other artificial substrates or site materials.

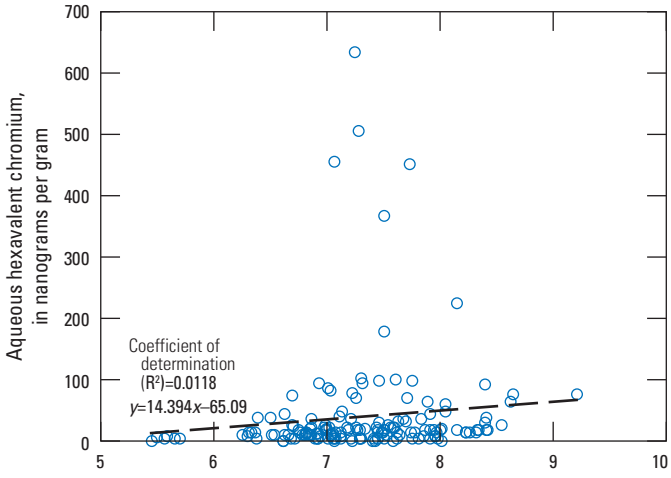

Figure I.39. Hexavalent chromium, Cr(VI), recovered in the aqueous phase of all oxidation samples plotted versus pH of the aqueous phase; the trendline represents a linear regression of all data, and the slope and intercept of the trendline and the coefficient of determination (R^2) are shown. Data are available in Miller and others (2020b).

I.4.3.3. Interpretation of Solid-Phase Analyses

The oxidation state of Mn changed rapidly after exposure to air containing oxygen. After 56 days, bulk Mn XANES were more like precursor material than material at the end of the reduction period. The allotted beam time expired before the end of the 2-year oxidation period; therefore, it is not known if Mn remained oxidized for the entire time. Assuming that Mn remained oxidized, the observed decreases in aqueous and sorbed Cr(VI) in Fe sand and mixed artificial substrates may be explained, like site materials, by Cr(VI) adsorption to freshly precipitated Fe or Fe-Mn oxides followed by occlusion by precipitates with lower Cr content. This scenario indicates that Fe oxidizes more slowly than Mn in the microcosms. Manganese sand, which contained only trace amounts of Fe, was the one substrate where the release of Cr(VI) was not attenuated after 1 year of oxidation. Iron oxides were rarely present within the Mn sand microcosms, and the lack of attenuation in the release of Cr(VI) in Mn sand with little Fe oxide supports the explanation that armoring by Fe oxides slowed release rates in the later months of the experiment.

The coatings on artificial substrates that were observed using optical microscopy might have influenced the availability of Cr(III), the access to Mn oxides, or both. Further, coatings could be acting to armor previously precipitated Cr(III) and dampen Cr(VI) release. Coating thickness increased shortly after the onset of oxidation in Fe sand, Mn sand, and Fe/Mn 50. Following the first 285 days of oxidation, coatings were thicker in Fe sand and thinner in Mn sand.

I.5. Conclusions

The U.S. Geological Survey was requested by the Lahontan Regional Water Quality Control Board (RWQCB) to complete an updated background study of hexavalent chromium, Cr(VI), concentrations in Hinkley and Water Valleys. Experiments described in this chapter were requested by the Lahontan RWQCB as part of the updated Cr(VI) background study. The purpose of these experiments was to evaluate the sequestration and potential for reoxidation of Cr(VI) from aquifer materials within the in situ reactive zone (IRZ) downgradient from the Hinkley compressor station.

Chromium (Cr) that was previously reduced and sequestered during in situ reduction may be reoxidized in the event of changing hydrologic conditions. The laboratory-based observations are consistent with findings of a field study where oxidation of Cr, previously reduced by natural attenuation, resulted in release of Cr(VI) into groundwater. Reoxidation, measured in the experiments as potential Cr(VI) available for release from solids after alkaline extraction, was observed after only 14 days of exposure to oxygen. As much as 10 percent of Cr added to microcosms prepared using recent Mojave River aquifer material was oxidized to Cr(VI), and as much as 20 percent of Cr added to microcosms prepared using older Mojave River aquifer material was oxidized to Cr(VI). Less Cr(VI) was released to the aqueous phase (less than 3 percent of Cr added before reduction), and this release followed longer oxygen exposure. However, even small amounts of Cr(VI) released to the aqueous phase may be an indication of future risk. Continued monitoring and maintenance of reduced conditions within the in situ reactive zone (IRZ) would ensure that Cr does not re-enter groundwater in the future after bioremediation with ethanol ceases.

The amount of reoxidation of trivalent chromium, Cr(III), increased with manganese (Mn) concentration during incubations with aquifer materials and artificial substrates. This relation is attributed to co-location of Cr and Mn in minerals and on particle surfaces during later stages of reduction. Chromite-like minerals containing Cr(III) and iron [Fe(II) and Fe(III)] and the presence of jacobsite-like minerals containing Cr(III), Fe(II), and Fe(III) with Mn(III) or Mn(IV) in reduced samples with elevated Cr were observed in study microcosms. It was further documented that Mn was present in the aqueous phase during later stages of reduction of site materials. Upon exposure to oxygen for as little as 14 days, this well-distributed Mn(II) was oxidized to Mn(III) and Mn(IV) that formed precipitates on particle surfaces. Thus, oxidized Mn was in close proximity to Cr(III) following even brief periods of reoxidation. In aquifer settings, it is possible that some of this Mn may move downgradient with groundwater potentially limiting reoxidation of reduced Cr(III) to Cr(VI). Mobilization of oxidized Cr(VI) on aquifer solids may be further limited in field settings by slightly acidic to alkaline groundwater pH that tends to promote sorption of Cr(VI) to aquifer solids.

Microcosm studies do not incorporate the effect of advective groundwater flow on the sequestration and reoxidation of Cr(VI) within the IRZ. However, results show that co-location of Cr and Mn within secondary minerals formed on particle surfaces may contribute to reoxidation of Cr(III) to Cr(VI) in study microcosms. Examination of core material collected within the regulatory Cr(VI) plume and within IRZ treated portions of the plume show (1) massive accumulations of Fe and Mn-containing hydroxides co-located on mineral grain surfaces and (2) fine-scale accumulations of Fe and Mn-containing hydroxides distributed on mineral grains in a spider-web manner at otherwise imperceptible lithologic contacts within the Cr(VI) regulatory plume (chapter C). These hydroxides contain a high fraction of weakly sorbed, potentially reactive Cr; similar hydroxide accumulations containing similar concentrations of weakly sorbed, reactive Cr were not observed at sites outside the mapped Cr(VI) regulatory plume (chapter C). Microcosm studies indicate that maintenance of anoxic (oxygen absent) conditions within the IRZ may ensure sequestration of Cr on aquifer solids as Cr(III) and prevent re-oxidation of Cr(III) to Cr(VI) and subsequent mobilization into groundwater in the future after ethanol bioremediation ends.

I.6. References Cited

Abed, R.M.M., Shanti, M., Muthukrishnan, T., Al-Riyami, Z., Pracejus, B., and Moraetis, D., 2020, The role of microbial mats in the removal of hexavalent chromium and associated shifts in their bacterial community composition: Frontiers in Microbiology, v. 11, no. 12, accessed January 6, 2020, at https://doi.org/10.3389/fmicb.2020.00012.

ARCADIS, 2016, Annual cleanup status and effectiveness report (January to December 2015), Pacific Gas and Electric Company, Hinkley Compressor Station, Hinkley, California: San Francisco, Calif., Pacific Gas and Electric Company, prepared by ARCADIS, Oakland, Calif., RC000699, [variously paged], accessed February 2016, at https://documents.geotracker.waterboards.ca.gov/esi/uploads/geo_report/5010230779/SL0607111288.PDF.

Bartlett, R., and James, B., 1979, Behavior of chromium in soils—Oxidation: Journal of Environmental Quality, v. 8, no. 1, p. 31–35. [Available at https://doi.org/10.2134/jeq1979.00472425000800010008x.]

Beller, H.R., Yang, L., Varadharajan, C., Han, R., Lim, H.C., Karaoz, U., Molins, S., Marcus, M.A., Brodie, E.L., Steefel, C.I., and Nico, P.S., 2014, Divergent aquifer biogeochemical systems converge on similar and unexpected Cr(VI) reduction products: Environmental Science & Technology, v. 48, no. 18, p. 10699–10706, accessed January 6, 2020, at https://doi.org/10.1021/es5016982.

Brewer, P.G., and Spencer, D.W., 1971, Colorimetric determination of manganese in anoxic waters: Limnology and Oceanography, v. 16, no. 1, p. 107–110. [Available at https://doi.org/10.4319/lo.1971.16.1.0107.]

Burle, E., and Kirby-Smith, W.W, 1979, Application of formaldoxime colorimetric method for the determination of manganese in the pore water of anoxic estuarine sediments: Estuaries, v. 2, p. 198–201, accessed January 6, 2020, at https://doi.org/10.2307/1351736.

Chao, T.T., and Sanzolone, R.F., 1989, Fractionation of soil selenium by sequential partial dissolution: Soil Science Society of America Journal, v. 53, no. 2, p. 385–392. [Available at https://doi.org/10.2136/sssaj1989.03615995005300020012x.]

Eary, L.E., and Rai, D., 1987, Kinetics of chromium(III) oxidation to chromium(VI) by reaction with manganese dioxide: Environmental Science & Technology, v. 21, no. 12, p. 1187–1193. [Available at https://doi.org/10.1021/es00165a005.]

Eary, L.E., and Rai, D., 1989, Kinetics of chromate reduction by ferrous ions derived from hematite and biotite at 25 degrees C: American Journal of Science, v. 289, no. 2, p. 180–213. [Available at https://doi.org/10.2475/ajs.289.2.180.]

Fandeur, D., Juillot, F., Morin, G., Olivi, L., Cognigni, A., Ambrosi, J.-P., Guyot, F., and Fritsch, E., 2009a, Synchrotron-based speciation of chromium in an oxisol from New Caledonia—Importance of secondary Fe-oxyhydroxides: The American Mineralogist, v. 94, no. 5–6, p. 710–719. [Available at https://doi.org/10.2138/am.2009.3073.]

Fandeur, D., Juillot, F., Morin, G., Olivi, L., Cognigni, A., Webb, S.M., Ambrosi, J.-P., Fritsch, W., Guyot, F., and Brown, G.E., Jr., 2009b, XANES evidence for oxidation of Cr(III) to Cr(VI) by Mn-oxides in a lateritic regolith developed on serpentinized ultramafic rocks of New Caledonia: Environmental Science & Technology, v. 43, no. 19, p. 7384–7390. [Available at https://doi.org/10.1021/es900498r.]

Faybishenko, B., Hazen, T.C., Long, P.E., Brodie, E.L., Conrad, M.E., Hubbard, S.S., Christensen, J.N., Joyner, D., Borglin, S.E., Chakraborty, R., Williams, K.H., Peterson, J.E., Chen, J., Brown, S.T., Tokunaga, T.K., Wan, J., Firestone, M., Newcomer, D.R., Resch, C.T., Cantrell, K.J., Willett, A., and Koenigsberg, S., 2008, In situ long-term reductive bioimmobilization of Cr(VI) in groundwater using hydrogen release compound: Environmental Science & Technology, v. 42, no. 22, p. 8478–8485. [Available at https://doi.org/10.1021/es801383r.]

Fendorf, S., Wielinga, B.W., and Hansel, C.M., 2000, Chromium transformations in natural environments—The role of biological and abiological processes in Cr(VI) reduction: International Geology Review, v. 42, no. 8, p. 691–701. [Available at https://doi.org/10.1080/00206810009465107.]

Foster, A.L., and Kim, C.S., 2014, Arsenic speciation in solids using X-ray absorption spectroscopy: Reviews in Mineralogy and Geochemistry, v. 79, no. 1, p. 257–369. [Available at https://doi.org/10.2138/rmg.2014.79.5.]

Foster, A.L., Wright, E.G., Bobb, C., Choy, D., and Miller, L.G., 2023, Optical petrography, bulk chemistry, micro-scale mineralogy/chemistry, and bulk/micron-scale solid-phase speciation of natural and synthetic solid phases used in chromium sequestration and re-oxidation experiments with sand and sediment from Hinkley, CA: U.S. Geological Survey data release, https://doi.org/10.5066/P9ENBLGY.

Fruchter, J., 2002, In-situ treatment of chromium-contaminated groundwater: Environmental Science & Technology, v. 36, no. 23, p. 464A–472A. [Available at https://doi.org/10.1021/es022466i.]

Groover, K.D., 2016, Elemental analyses using a handheld x-Ray fluorescence spectrometer: U.S. Geological Survey Fact Sheet 2016–3043, 2 p., accessed August 2, 2017, at https://doi.org/10.3133/fs20163043.

Groover, K.D., and Izbicki, J.A., 2018, Field portable X-ray fluorescence and associated quality control data for the western Mojave Desert, San Bernardino County, California: U.S. Geological Survey data release, accessed November 29, 2018, at https://doi.org/10.5066/P9CU0EH3.

Groover, K.D., and Izbicki, J.A., 2019, Selected trace-elements in alluvium and rocks, western Mojave Desert, southern California: Journal of Geochemical Exploration, v. 200, p. 234–248. [Available at https://doi.org/10.1016/j.gexplo.2018.09.005.]

Haley and Aldrich, Inc., 2010, Feasibility study, Pacific Gas and Electric Company Hinkley compressor station, Hinkley, California, Addendum 3: San Francisco, Calif., Pacific Gas and Electric Company, prepared by Haley and Aldrich, San Diego, Calif., [variously paged], accessed November 27, 2018, at https://www.waterboards.ca.gov/lahontan/water_issues/projects/pge/fsr083010.html.

Hansel, C.M., Wielinga, B.W., and Fendorf, S., 2003a, Structural and compositional evolution of Cr/Fe solids after indirect chromate reduction by dissimilatory iron-reducing bacteria: Geochimica et Cosmochimica Acta, v. 67, no. 3, p. 401–412. [Available at https://doi.org/10.1016/S0016-7037(02)01081-5.]

Hansel, C.M., Benner, S.G., Neiss, J., Dohnalkova, A., Kukkadapu, R.K., and Fendorf, S., 2003b, Secondary mineralization pathways induced by dissimilatory iron reduction of ferrihydrite under advective flow: Geochimica et Cosmochimica Acta, v. 67, no. 16, p. 2977–2992. [Available at https://doi.org/10.1016/S0016-7037(03)00276-X.]

Hausladen, D.M., and Fendorf, S., 2017, Hexavalent chromium generation within naturally structured soils and sediments: Environmental Science & Technology, v. 51, no. 4, p. 2058–2067. [Available at https://doi.org/10.1021/acs.est.6b04039.]

Hausladen, D.M., Alexander-Ozinskas, A., McClain, C., and Fendorf, S., 2018, Hexavalent chromium sources and distribution in California groundwater: Environmental Science & Technology, v. 52, no. 15, p. 8242–8251. [Available at https://doi.org/10.1021/acs.est.7b06627.]

Hausladen, D., Fakhreddine, S., and Fendorf, S., 2019, Governing constraints of Chromium(VI) formation from Chromium(III)-bearing minerals in soils and sediments: Soil Systems, v. 3, no. 4, accessed January 6, 2020, at https://doi.org/10.3390/soilsystems3040074.

Izbicki, J.A., and Groover, K.D., 2016, A plan for study of natural and man-made hexavalent chromium, Cr(VI), in groundwater near a mapped plume, Hinkley, California: U.S. Geological Survey Open-File Report 2016–1004, 12 p., accessed November 28, 2018, at https://doi.org/10.3133/ofr20161004.

Izbicki, J.A., and Groover, K.D., 2018, Natural and man-made hexavalent chromium, Cr(VI), in groundwater near a mapped plume, Hinkley, California—Study progress as of May 2017, and a summative-scale approach to estimate background Cr(VI) concentrations: U.S. Geological Survey Open-File Report 2018–1045, 28 p., accessed November 28, 2018, at https://doi.org/10.3133/ofr20181045.

Jacobs Engineering Group, Inc., 2019, Ground water flow modeling to support the Hinkley chromium background study, San Bernardino County, California, Project no. 706888CH, for Pacific Gas and Electric Company: Redding, Calif., Jacobs Engineering Group, Inc., [variously paged], with Appendixes A through H.

Jobby, R., Jha, P., Yadav, A.K., and Desai, N., 2018, Biosorption and biotransformation of hexavalent chromium [Cr(VI)]—A comprehensive review: Chemosphere, v. 207, p. 255–266. [Available at https://doi.org/10.1016/j.chemosphere.2018.05.050.]

Kent, D.B., Davis, J.A., Anderson, L.C.D., Rea, B., and Waite, T.D., 1994, Transport of chromium and selenium in the suboxic zone of a shallow aquifer—Influence of redox and adsorption reactions: Water Resources Research, v. 30, no. 4, p. 1099–1114. [Available at https://doi.org/10.1029/93WR03244.]

Klein, C., 1998, Manual of Mineralogy (21st ed.): Hoboken, N.J., John Wiley & Sons, Inc., 704 p.

Koningsberger, D.C., and Prins, R., eds., 1988, X-ray absorption—Principles, applications, techniques of EXAFS, SEXAFS, and XANES: Hoboken, N.J., John Wiley & Sons, 688 p. [Available at https://www.wiley.com/en-us/X+Ray+Absorption%3A+Principles%2C+Applications%2C+Techniques+of+EXAFS%2C+SEXAFS+and+XANES+-p-9780471875475.]

Lafuente, B., Downs, R.T., Yang, H., and Stone, N., 2015, The power of databases—The RRUFF project, *in* Armbruster, T., and Danisi, R.M., eds., Highlights in mineralogical crystallography: Berlin, Germany, De Gruyter, p. 1–30. [Available at https://doi.org/10.1515/9783110417104-003.]

Lahontan Regional Water Quality Control Board, 2011, Investigative order no. R6V-2011-0053, to submit revised manganese mitigation plan for the PG&E Hinkley compressor station, San Bernardino County—Cleanup and abatement order no. R6V-2008-0002: South Lake Tahoe, Calif., California Regional Water Quality Control Board, Lahontan Region, 4 p. [Available at https://documents.geotracker.waterboards.ca.gov/regulators/deliverable_documents/9066225945/r6v2011_53.pdf.]

Lahontan Regional Water Quality Control Board, 2013, Final environmental impact report—Comprehensive groundwater cleanup strategy for historical chromium discharges from PG&E's Hinkley Compressor Station, San Bernardino County: South Lake Tahoe, Calif., California Regional Water Quality Control Board, Lahontan Region, [variously paged], accessed November 20, 2018, at https://www.waterboards.ca.gov/rwqcb6/water_issues/projects/pge/docs/feir/vol1_intro.pdf.

Lahontan Regional Water Quality Control Board, 2015, Cleanup and abatement order no. R6V-2015-0068—Requiring Pacific Gas and Electric Company to clean up and abate waste discharges of total and hexavalent chromium to the groundwaters of the Mojave Hydrologic Unit: Lahontan Regional Water Quality Control Board, 80 p., accessed July 17, 2017, at https://www.waterboards.ca.gov/lahontan/water_issues/projects/pge/docs/pge_cao_revised_attachments.pdf.

Lovley, D.R., 1993, Dissimilatory metal reduction: Annual Review of Microbiology, v. 47, no. 1, p. 263–290. [Available at https://doi.org/10.1146/annurev.mi.47.100193.001403.]

Lovley, D.R., and Coates, J.D., 1997, Bioremediation of metal contamination: Current Opinion in Biotechnology, v. 8, no. 3, p. 285–289. [Available at https://doi.org/10.1016/S0958-1669(97)80005-5.]

Lovley, D.R., and Phillips, E.J.P., 1986, Availability of ferric iron for microbial reduction in bottom sediments of the freshwater tidal Potomac River: Applied and Environmental Microbiology, v. 52, no. 4, p. 751–757. [Available at https://doi.org/10.1128/aem.52.4.751-757.1986.]

Lovley, D.R., and Phillips, E.J.P., 1994, Reduction of chromate by *Desulfovibrio vulgaris* and its c_3 cytochrome: Applied and Environmental Microbiology, v. 60, no. 2, p. 726–728. [Available at https://doi.org/10.1128/aem.60.2.726-728.1994.]

Marsh, T.L., Leon, N.M., and McInerney, M.J., 2000, Physiochemical factors affecting chromate reduction by aquifer materials: Geomicrobiology Journal, v. 17, no. 4, p. 291–303. [Available at https://doi.org/10.1080/01490450050193351.]

McKenzie, R.M., 1971, The synthesis of birnessite, cryptomelane, and some other oxides and hydroxides of manganese: Mineralogical Magazine, v. 38, no. 296, p. 493–502. [Available at https://doi.org/10.1180/minmag.1971.038.296.12.]

Mikutta, R., Kleber, M., Kaiser, K., and Jahn, R., 2005, Review—Organic matter removal from soils using hydrogen peroxide, sodium hypochlorite, and disodium peroxodisulfate: Soil Science Society of America Journal, v. 69, no. 1, p. 120–135. [Available at https://doi.org/10.2136/sssaj2005.0120.]

Miller, D.M., Haddon, E.K., Langenheim, V.E., Cyr, A.J., Wan, E., Walkup, L.C., and Starratt, S.W., 2018, Middle Pleistocene infill of Hinkley Valley by Mojave River sediment and associated lake sediment—Depositional architecture and deformation by strike-slip faults, *in* Miller, D.M., ed., The Mojave River from sink to source: The 2018 Desert Symposium Field Guide and Proceedings, April 2018.

Miller, D.M., Langenheim, V.E., and Haddon, E.K., 2020a, Geologic map and borehole stratigraphy of Hinkley Valley and vicinity, San Bernardino County, California: U.S. Geological Survey Scientific Investigations Map 3458, 23 p., 2 sheets, scale 1:24,000. [Available at https://doi.org/10.3133/sim3458.]

Miller, L.G., Bobb, C., Bennett, S., and Baesman, S.M., 2020b, Aqueous and solid phase chemistry of sequestration and re-oxidation of chromium in experimental microcosms with sand and sediment from Hinkley, CA: U.S. Geological Survey data release, accessed January 6, 2020, at https://doi.org/10.5066/P9U8C82V.

Mills, C.T., Morrison, J.M., Goldhaber, M.B., and Ellefsen, K.J., 2011, Chromium(VI) generation in vadose zone soils and alluvial sediments of the southwestern Sacramento Valley, California—A potential source of geogenic Cr(VI) to groundwater: Applied Geochemistry, v. 26, no. 8, p. 1488–1501. [Available at https://doi.org/10.1016/j.apgeochem.2011.05.023.]

Mills, C.T., Bern, C.R., Wolf, R.E., Foster, A.L., Morrison, J.M., and Benzel, W.M., 2017, Modifications to EPA method 3060A to improve extraction of Cr(VI) from chromium ore processing residue-contaminated soils: Environmental Science & Technology, v. 51, no. 19, p. 11235–11243. [Available at https://doi.org/10.1021/acs.est.7b01719.]

Mojave Water Agency, 2014, Geospatial library: Mojave Water Agency web page, accessed May 22, 2014, at https://www.mojavewater.org/data-maps/geospatial-library/.

Morrison, J.M., Benzel, W.M., Holm-Denoma, C.S., and Bala, S., 2018, Grain size, mineralogic, and trace-element data from field samples near Hinkley, California: U.S. Geological Survey data release, https://doi.org/10.5066/P9HUPMG0.

Murray, K.J., and Tebo, B.M., 2007, Cr(III) is indirectly oxidized by the Mn(II)-oxidizing bacterium *Bacillus* sp. strain SG-1: Environmental Science & Technology, v. 41, no. 2, p. 528–533. [Available at https://doi.org/10.1021/es0615167.]

Namgung, S., Kwon, M.J., Qafoku, N.P., and Lee, G., 2014, $Cr(OH)_3(s)$ oxidation induced by surface catalyzed Mn(II) oxidation: Environmental Science & Technology, v. 48, no. 18, p. 10760–10768. [Available at https://doi.org/10.1021/es503018u.]

Nelson, J., Joe-Wong, C., and Maher, K., 2019, Cr(VI) reduction by Fe(II) sorbed to silica surfaces: Chemosphere, v. 234, p. 98–107. [Available at https://doi.org/10.1016/j.chemosphere.2019.06.039.]

Neter, J., and Wasserman, W., 1974, Applied linear statistical models: Homewood, Ill., Richard D. Irwin Inc., 152 p.

Nico, P.S., and Zasoski, R.J., 2000, Importance of Mn(III) availability on the rate of Cr(III) oxidation on δ-MnO_2: Environmental Science & Technology, v. 34, no. 16, p. 3363–3367. [Available at https://doi.org/10.1021/es991462j.]

O'Day, P.A., Rivera, N., Jr., Root, R., and Carroll, S.A., 2004, X-ray absorption spectroscopic study of Fe reference compounds for the analysis of natural sediments: The American Mineralogist, v. 89, no. 4, p. 572–585. [Available at https://doi.org/10.2138/am-2004-0412.]

Oremland, R.S., Hoeft, S.E., Santini, J.M., Bano, N., Hollibaugh, R.A., and Hollibaugh, J.T., 2002, Anaerobic oxidation of arsenite in Mono Lake water and by a facultative, arsenite-oxidizing chemoautotroph, strain MLHE-1: Applied and Environmental Microbiology, v. 68, no. 10, p. 4795–4802. [Available at https://doi.org/10.1128/AEM.68.10.4795-4802.2002.]

Oze, C., Bird, D.K., and Fendorf, S., 2007, Genesis of hexavalent chromium from natural sources in soil and groundwater: Proceedings of the National Academy of Sciences of the United States of America, v. 104, no. 16, p. 6544–6549. [Available at https://doi.org/10.1073/pnas.0701085104.]

Pacific Gas and Electric Company, 2011, Addendum #2 to the feasibility study: San Francisco, Calif., Pacific Gas and Electric Company, [variously paged], accessed May 7, 2020, at https://www.waterboards.ca.gov/lahontan/water_issues/projects/pge/docs/addndm2.pdf.

Papp, C.S.E., Filipek, L.H., and Smith, K.S., 1991, Selectivity and effectiveness of extractants used to release metals associated with organic matter: Applied Geochemistry, v. 6, no. 3, p. 349–353. [Available at https://doi.org/10.1016/0883-2927(91)90010-M.]

Peterson, M.L., Brown, G.E., Jr., Parks, G.A., and Stein, C.L., 1997a, Differential redox and sorption of Cr(III/VI) on natural silicate and oxide minerals—EXAFS and XANES results: Geochimica et Cosmochimica Acta, v. 61, no. 16, p. 3399–3412. [Available at https://doi.org/10.1016/S0016-7037(97)00165-8.]

Peterson, M.L., White, A.F., Brown, G.E., Jr., and Parks, G.A., 1997b, Surface passivation of magnetite by reaction with aqueous Cr(VI)—XAFS and TEM results: Environmental Science & Technology, v. 31, no. 5, p. 1573–1576. [Available at https://doi.org/10.1021/es960868i.]

Puzon, G.J., Roberts, A.G., Kramer, D.M., and Xun, L., 2005, Formation of soluble organo-chromium(III) complexes after chromate reduction in the presence of cellular organics: Environmental Science & Technology, v. 39, no. 8, p. 2811–2817. [Available at https://doi.org/10.1021/es048967g.]

Rai, D., Eary, L.E., and Zachara, J.M., 1989, Environmental chemistry of chromium: Science of the Total Environment, v. 86, no. 1–2, p. 15–23. [Available at https://doi.org/10.1016/0048-9697(89)90189-7.]

Saha, R., Nandi, R., and Saha, B., 2011, Sources and toxicity of hexavalent chromium: Journal of Coordination Chemistry, v. 64, no. 10, p. 1782–1806. [Available at https://doi.org/10.1080/00958972.2011.583646.]

Sass, B.M., and Rai, D., 1987, Solubility of amorphous chromium(III)-iron(III) hydroxide solid solutions: Inorganic Chemistry, v. 26, no. 14, p. 2228–2232. [Available at https://doi.org/10.1021/ic00261a013.]

Schroeder, D.C., and Lee, G.F., 1975, Potential transformations of chromium in natural waters: Water, Air, and Soil Pollution, v. 4, no. 3–4, p. 355–365. [Available at https://doi.org/10.1007/BF00280721.]

Schwertmann, U., and Cornell, R.M., 2000, Iron oxides in the laboratory—Preparation and characterization: New York, N.Y., Wiley-VCH, 188 p. [Available at https://doi.org/10.1002/9783527613229.]

Sedlazeck, P., Höllen, D., Müller, P., Mischitz, R., and Gieré, R., 2017, Mineralogical and geochemical characterization of a chromium contamination in an aquifer—A combined analytical and modeling approach: Applied Geochemistry, v. 87, p. 44–56. [Available at https://doi.org/10.1016/j.apgeochem.2017.10.011.]

Slejko, F.F., Petrini, R., Lutman, A., Forte, C., and Ghezzi, L., 2019, Chromium isotopes tracking the resurgence of hexavalent chromium contamination in a past-contaminated area in the Friuli Venezia Giulia Region, northern Italy: Isotopes in Environmental and Health Studies, v. 55, no. 1, p. 56–69. [Available at https://doi.org/10.1080/10256016.2018.1560278.]

Stamos, C.L., Martin, P., Nishikawa, T., and Cox, B.F., 2001, Simulation of ground-water flow in the Mojave River basin, California: U.S. Geological Survey Water-Resources Investigations Report 2001–4002, 129 p. [Available at https://doi.org/10.3133/wri014002.]

Stookey, L.L., 1970, Ferrozine—A new spectrophotometric reagent for iron: Analytical Chemistry, v. 42, no. 7, p. 779–781. [Available at https://doi.org/10.1021/ac60289a016.]

Tang, Y., Webb, S.M., Estes, E.R., and Hansel, C.M., 2014, Chromium(III) oxidation by biogenic manganese oxides with varying structural ripening: Environmental Science—Processes & Impacts, v. 16, no. 9, accessed January 6, 2020, at https://doi.org/10.1039/C4EM00077C.

Tessier, A., Campbell, P.G.C., and Bisson, M., 1979, Sequential extraction procedure for the speciation of particulate trace metals: Analytical Chemistry, v. 51, no. 7, p. 844–851. [Available at https://doi.org/10.1021/ac50043a017.]

Thatoi, H., Das, S., Mishra, J., Rath, B.P., and Das, N., 2014, Bacterial chromate reductase—A potential enzyme for bioremediation of hexavalent chromium—A review: Journal of Environmental Management, v. 146, p. 383–399. [Available at https://doi.org/10.1016/j.jenvman.2014.07.014.]

Thompson, A., and Vaughan, D., eds., 2001, X-ray data booklet: Berkeley, Calif., Lawrence Berkeley National Laboratory, 457 p. [Available at https://xdb.lbl.gov.]

Tokunaga, T.K., Wan, J., Firestone, M.K., Hazen, T.C., Olson, K.R., Herman, D.J., Sutton, S.R., and Lanzirotti, A., 2003, In situ reduction of chromium(VI) in heavily contaminated soils through organic carbon amendment: Journal of Environmental Quality, v. 32, no. 5, p. 1641–1649. [Available at https://doi.org/10.2134/jeq2003.1641.]

Tokunaga, T.K., Wan, J., Lanzirotti, A., Sutton, S.R., Newville, M., and Rao, W., 2007, Long-term stability of organic carbon-stimulated chromate reduction in contaminated soils and its relation to manganese redox status: Environmental Science & Technology, v. 41, no. 12, p. 4326–4331. [Available at https://doi.org/10.1021/es062874c.]

U.S. Environmental Protection Agency, 1992, Colorimetric determination of hexavalent chromium, method 7196—Test methods for evaluating solid waste: Washington, D.C., U.S. Government Printing Office, 6 p.

U.S. Environmental Protection Agency, 1996, Alkaline digestion for hexavalent chromium, method 3060A: Washington, D.C., U.S. Government Printing Office, 15 p.

U.S. Environmental Protection Agency, 2007, Field portable x-ray fluorescence spectrometry for the determination of elemental concentrations in soil and sediment, method 6200 (revision 0): Washington, D.C., U.S. Government Printing Office, 32 p.

U.S. Geological Survey, 2021, USGS water data for the Nation: U.S. Geological Survey National Water Information System database, accessed January 6, 2021, at https://doi.org/10.5066/F7P55KJN.

Viollier, E., Inglett, P.W., Hunter, K., Roychoudhury, A.N., and Van Cappellen, P., 2000, The ferrozine method revisited—Fe(II)/Fe(III) determination in natural waters: Applied Geochemistry, v. 15, no. 6, p. 785–790, accessed January 6, 2020, at https://doi.org/10.1016/S0883-2927(99)00097-9.

Waychunas, G.A., Fuller, C.C., Rea, B.A., and Davis, J.A., 1996, Wide angle X-ray scattering (WAXS) study of "two-line" ferrihydrite structure—Effect of arsenate sorption and counterion variation and comparison with EXAFS results: Geochimica et Cosmochimica Acta, v. 60, no. 10, p. 1765–1781. [Available at https://doi.org/10.1016/0016-7037(96)89830-9.]

Webb, S.M., 2005, SIXpack—A graphical user interface for XAS analysis using IFEFFIT: Physica Scripta, v. 2005, no. T115, p. 1011. [Available at https://doi.org/10.1238/Physica.Topical.115a01011.]

Wenzel, W.W., Kirchbaumer, N., Prohaska, T., Stingeder, G., Lombi, E., and Adriano, D.C., 2001, Arsenic fractionation in soils using an improved sequential extraction procedure: Analytica Chimica Acta, v. 436, no. 2, p. 309–323. [Available at https://doi.org/10.1016/S0003-2670(01)00924-2.]

Wu, Y., Deng, B., Xu, H., and Kornishi, H., 2005, Chromium(III) oxidation coupled with microbially mediated Mn(II) oxidation: Geomicrobiology Journal, v. 22, no. 3–4, p. 161–170, accessed January 6, 2020, at https://doi.org/10.1080/01490450590945997.

Zimmerman, A.J., and Weindorf, D.C., 2010, Heavy metal and trace metal analysis in soil by sequential extraction—A review of procedures: International Journal of Analytical Chemistry, v. 2010, 8 p., accessed January 6, 2020, at https://doi.org/10.1155/2010/387803.

Appendix I.1. Experimental Microcosms Used for Solid-Phase Analysis

This appendix contains one table (table I.1.1) that summarizes experimental microcosm source materials and treatment for reduction and oxidation experiments. The materials were used for incubations and solid-phase analysis discussed in this chapter. The numbers in the table refer to an inventory system developed to uniquely identify samples and correspond to identification numbers used by Miller and others (2020) and Foster and others (2023). Values "na(1)" and "na(2)" indicate materials not analyzed for reasons described in the footnotes.

References Cited

Foster, A.L., Wright, E.G., , Bobb, C., Choy, D., and Miller, L.G., 2023, Optical petrography, bulk chemistry, micro-scale mineralogy/chemistry, and bulk/micron-scale solid-phase speciation of natural and synthetic solid phases used in chromium sequestration and re-oxidation experiments with sand and sediment from Hinkley, CA: U.S. Geological Survey data release, https://doi.org/10.5066/P9ENBLGY.

Miller, L.G., Bobb, C., Bennett, S., and Baesman, S.M., 2020, Aqueous and solid phase chemistry of sequestration and re-oxidation of chromium in experimental microcosms with sand and sediment from Hinkley, CA: U.S. Geological Survey data release, https://doi.org/10.5066/P9U8C82V.

Table I.1.1. Summary of precursor and timepoint samples from reduction and oxidations microcosm experiments.

[The numbers in each cell refer to an inventory system developed to uniquely identify analyzed samples. **Abbreviations**: ft bls, foot below land surface; B, bottle; Fe sand, iron coated sand; Mn sand, manganese coated sand; Fe/Mn, ratio of Fe sand to Mn sand by weight; n/a (2), not applicable, created from physical mix of Fe-Sand and Mn-Sand; a, b, c, "clay", "silt", and "sand" subsamples; n/a (1), not applicable, material not used in this experiment; —, not analyzed]

Material	SA-SB-01 103–108 ft bls	BG-0004 53.0–61.2 ft bls	BG-0005 104.0–114.5 ft bls	Fe sand	Washed sand	Mn sand	Fe/Mn 25	Fe/Mn 50	Fe/Mn 100
Precursor material	14, 20, 186	9a, 9b, 59, 84	3, 60, 185	2, 68	175	1, 67	n/a (2)	n/a (2)	n/a (2)
Reduction experiment									
B1 a, b, c: Aerobic 83 days	n/a (1)	65, 54, 49	n/a (1)	n/a (1)	n/a (1)	n/a (1)	n/a (1)	n/a (1)	n/a (1)
B2 a, b, c: Reduced 0 days	n/a (1)	64, 55, 50	n/a (1)	n/a (1)	n/a (1)	n/a (1)	n/a (1)	n/a (1)	n/a (1)
B3 a, b, c: Reduced 83 days	n/a (1)	63, 56, 51	n/a (1)	n/a (1)	n/ (1)	n/a (1)	n/a (1)	n/a (1)	n/a (1)
B4 a, b, c: Reduced 168 days	n/a (1)	62, 57, 52	n/a (1)	n/a (1)	n/a (1)	n/a (1)	n/a (1)	n/a (1)	n/a (1)
B5 a, b, c: Reduced 350 days	n/a (1)	61, 58, 53	n/a (1)	n/a (1)	n/a (1)	n/a (1)	n/a (1)	n/a (1)	n/a (1)
41 days	—	107	108	—	—	n/a (1)	n/a (1)	n/a (1)	n/a (1)
83 days	—	—	—	—	137	n/a (1)	n/a (1)	n/a (1)	n/a (1)
720 days	—	109	110	—	—	n/a (1)	n/a (1)	n/a (1)	n/a (1)
Oxidation experiment									
Time 0 (1.25 yr reduction)	91, 122 (black)	92	93, 120 (black)	88, 121 (black)	n/a (1)	89	119 (black)	90	—
14 days	86	87	81	84	n/a (1)	85	83	80	82
56 days	104	105	106	101	n/a (1)	102	133	103	132
125 days	113	111	112	114	n/a (1)	115	118	116	117
285 days	126	124	125	127	n/a (1)	128	131	129	130
Elevated Cr reduction experiment									
5-month bulk	n/a (1)	144	146	n/a (1)	140	n/a (1)	n/a (1)	142	n/a (1)
5-month fine material	n/a (1)	153	149	n/a (1)	—	n/a (1)	n/a (1)	—	n/a (1)
8-month bulk	n/a (1)	145	147	n/a (1)	141	n/a (1)	n/a (1)	143	n/a (1)
8-month fine material	n/a (1)	151	152	n/a (1)	—	n/a (1)	n/a (1)	—	n/a (1)

For more information concerning the research in this report, contact the

Director, California Water Science Center
U.S. Geological Survey
6000 J Street, Placer Hall
Sacramento, California 95819
https://www.usgs.gov/centers/ca-water/

Publishing support provided by the U.S. Geological Survey
Science Publishing Network, Sacramento Publishing Service Center

Miller and others—**Chapter I: Sequestration and Reoxidation of Chromium in Experimental Microcosms**—PP 1885-I

ISSN 2330-7102 (online)
https://doi.org/10.3133/pp1885I